TALLINN UNIVERSITY OF TECHNOLOGY
DOCTORAL THESIS
21/2020

The Study of Magnetoelectric Effect in Multiferroics Using THz Spectroscopy

JOHAN VIIROK

TAL
TECH
PRESS

TALLINN UNIVERSITY OF TECHNOLOGY
School of Science
Department of Cybernetics

The dissertation was accepted for the defence of the degree of Doctor of Philosophy (Applied Physics) on 04 June 2020

Supervisor: PhD Toomas Rõõm,
National Institute of Chemical Physics and Biophysics,
Tallinn, Estonia

Co-supervisor: PhD Urmas Nagel,
National Institute of Chemical Physics and Biophysics,
Tallinn, Estonia

Opponents: Professor Andrei Pimenov,
Vienna University of Technology,
Vienna, Austria

Professor Marco Kirm,
University of Tartu,
Tartu, Estonia

Defence of the thesis: 16 July 2020, Tallinn

Declaration:
Hereby I declare that this doctoral thesis, my original investigation and achievement, submitted for the doctoral degree at Tallinn University of Technology, has not been submitted for any academic degree elsewhere.

Johan Viirok

signature

European Union
European Regional
Development Fund

Investing
in your future

Copyright: Johan Viirok, 2020
ISSN 2585-6898 (publication)
ISBN 978-9949-83-568-3 (publication)
ISSN 2585-6901 (PDF)
ISBN 978-9949-83-569-0 (PDF)
Printed by Auratrükk

TALLINNA TEHNIKAÜLIKOOL
DOKTORITÖÖ
21/2020

Magnetelektrilise nähtuse uurimine multiferroidides THz spektroskoopiaga

JOHAN VIIROK

Contents

List of Publications 7

Author's Contributions to the Publications 8

Introduction 10

1 Theoretical Principles 13
  1.1 Multiferroics 13
  1.2 Magnetoelectric Effect in Multiferroics 14
    1.2.1 Nonreciprocal Directional Dichroism 16
    1.2.2 Dynamic ME Effect and Nonreciprocal Directional Dichroism 16
    1.2.3 Microscopic Description of the Dynamic Magnetoelectric Effect 18
    1.2.4 Magnetoelectric Sum Rule 20
  1.3 Magnetoelectric Coupling Mechanisms for Type-II Multiferroics 20
    1.3.1 Exchange Striction Mechanism 21
    1.3.2 Dzyaloshinskii-Moriya Mechanism 22
    1.3.3 Spin-dependent Hybridization Mechanism 22

2 Experimental Details 25
  2.1 Interferometry with Michelson and Martin-Puplett Interferometers 25
  2.2 TeslaFIR Experimental Setup 27
  2.3 Voigt Probes 29
    2.3.1 Rotating Voigt Probe 29
    2.3.2 High-Temperature High-Voltage Voigt Probe 31
  2.4 Filter Wheel 33
  2.5 Thermometry 34
  2.6 Resistive Bitter Magnet Measurement System in Nijmegen 36

3 Data Analysis 37
  3.1 Fitting Software FitPeaks 39
  3.2 BdepTools - Python Library for Preparing Figures for Publishing 42

4 Results and Discussion 43
  4.1 $CaBaCo_4O_7$ 43
  4.2 $Sr_2CoSi_2O_7$ 46
  4.3 $LiCoPO_4$ 48

5 Achievements 53

6 Conclusions 55

List of Figures 56

References 57

Acknowledgements 65

Abstract 66

Kokkuvõte 68

Appendix 1 71

Appendix 2 81

Appendix 3 97

Curriculum Vitae 108

Elulookirjeldus 111

List of Publications

The present Ph.D. thesis is based on the following publications that are referred to in the text by Roman numbers.

I R. S. Fishman, S. Bordács, V. Kocsis, I. Kézsmárki, J. Viirok, U. Nagel, T. Rõõm, A. Puri, U. Zeitler, Y. Tokunaga, Y. Taguchi, and Y. Tokura. Competing exchange interactions in multiferroic and ferrimagnetic $CaBaCo_4O_7$. *Phys. Rev. B*, 95:024423, Jan 2017.

II J. Viirok, U. Nagel, T. Rõõm, D. G. Farkas, P. Balla, D. Szaller, V. Kocsis, Y. Tokunaga, Y. Taguchi, Y. Tokura, B. Bernáth, D. L. Kamenskyi, I. Kézsmárki, S. Bordács, and K. Penc. Directional dichroism in the paramagnetic state of multiferroics: A case study of infrared light absorption in $Sr_2CoSi_2O_7$ at high temperatures. *Phys. Rev. B*, 99:014410, Jan 2019.

III V. Kocsis, S. Bordács, Y. Tokunaga, J. Viirok, L. Peedu, T. Rõõm, U. Nagel, Y. Taguchi, Y. Tokura, and I. Kézsmárki. Magnetoelectric spectroscopy of spin excitations in $LiCoPO_4$. *Phys. Rev. B*, 100:155124, Oct 2019.

Author’s Contributions to the Publications

I In I, I designed and built the rotating Voigt probe that made this kind of experiment possible. With that probe I carried out optical experiments on the TeslaFIR setup in NICPB. After that I analyzed the results, prepared figures and took part in writing the manuscript.

II In II, I conducted the optical experiments in NICPB and HFML. I analyzed the experimental results, prepared the figures for publication, wrote the first draft of the manuscript and included the theory developed by Peter Balla and Karlo Penc.

III In III, I modified our experimental setup to allow high voltage experiments. I assembled the equipment for the optical experiments, conducted these measurements in NICPB and analyzed the results.

Approbation

I presented the results of the thesis at the following conferences:

1. **J. Viirok**, T. Rõõm, U. Nagel, D. G. Farkas, V. Kocsis, D. Szaller, I. Kézsmárki, P. Balla, K. Penc, Y. Tokunaga, Y. Taguchi, Y. Tokura. ’Directional Dichroism of THz Radiation in Multiferroic $Sr_2CoSi_2O_7$’, 2nd Grandmaster PhD Workshop in Physics: 6–11 September 2015, Budapest, Hungary.

2. **J. Viirok**, T. Rõõm, U. Nagel, D. G. Farkas, V. Kocsis, D. Szaller, I. Kézsmárki, P. Balla, K. Penc, Y. Tokunaga, Y. Taguchi, Y. Tokura. ’Directional Dichroism of THz Radiation in Multiferroic $Sr_2CoSi_2O_7$’, V International Symposium on Strong Nonlinear Vibronic and Electronic Interactions in Solids, 30 April–03 May 2015, Tartu, Estonia.

3. **J. Viirok**, U. Nagel, T. Rõõm, D. G. Farkas, P. Balla, D. Szaller, V. Kocsis, Y. Tokunaga, Y. Taguchi, Y. Tokura, B. Bernáth, D. L. Kamenskyi, I. Kézsmárki, S. Bordács and K. Penc. ‘Non-Reciprocal Directional Dichroism of THz Radiation in Multiferroic $Sr_2CoSi_2O_7$’, APS March Meeting: 4–8 March 2019, Boston, MA, USA.

Introduction

Multiferroic materials have gained enormous interest in recent years due to their versatile possibilities for applications in sensing, data storage, and computing [1–3]. These functionalities rely on the magnetoelectric effect which is augmented in multiferroics by the coexistence of ferroelectric and magnetic order. Magnetoelectric effect changes not only the static but also the dynamic properties of matter. One of the most fascinating optical effects in a magnetoelectric medium is the directional optical anisotropy also called the optical diode effect. If both symmetries, the spatial inversion and time-reversal, are broken, light beams passing through the medium in positive and negative direction can have different indices of refraction which may give rise to the so called one-way transparency [4].

Although the one-way transparency was observed a long time ago for the exciton transitions of the polar semiconductor CdS [5], it was recognized as a general magneto-optical phenomenon of noncentrosymmetric materials only by the original works of Rikken and his co-workers [6,7]. This optical directional anisotropy enables new applications for multiferroics in photonics, e.g. efficient one-way light guides. Furthermore, the transparent direction can be switched with applied magnetic [8] and possibly with electric field [9,10], paving the way for directional light switches for THz radiation [11]. However, the spontaneous electric and magnetic order in most multiferroic crystals known up to now exists only at cryogenic temperatures where the multiferroic phase develops, rendering their use in device applications impractical. Clarifying the fundamentals of the non-reciprocal optical phenomena and its enhancement in multiferroic crystals will help in designing and discovering novel materials that work at room temperature and beyond, opening the road to new applications.

THz absorption spectroscopy offers an excellent tool to investigate spin excitation spectra over a broad magnetic field range. As compared to the inelastic neutron scattering (INS), only spin excitations with zero linear momentum are probed, but with a better energy resolution. In addition to resonance frequencies of spin excitations, THz spectroscopy can determine whether the spin excitations couple to electric, magnetic, or to both electric and magnetic field components of radiation [12]. This information is essential for developing spin models that would describe the ground and the low-lying excited states of the material [13,14]. Very high sensitivity accompanied with THz radiation polarization control and strong magnetic fields make the results obtained with terahertz optical spectroscopy setup at the National Institute of Chemical Physics and Biophysics in Tallinn unique.

The main research focus of the author is the investigation of materials showing fascinating magneto-optical effects in order to help the tailoring of novel compounds with unique properties for information technology and optics. The study of such compounds over an extended range of magnetic field and temperature often provides essential information about the complex magnetic states and gives a clue for the well-controlled synthesis of new systems.

The *goal* of this PhD work is to investigate magnetoelectric effects in three multiferroic materials – $CaBaCo_4O_7$, $Sr_2CoSi_2O_7$ and $LiCoPO_4$ – and to understand the issues on the way of making their magnetoelectric applications feasible. $CaBaCo_4O_7$ has the highest spin-induced electric polarization, $Sr_2CoSi_2O_7$ features single-spin ME coupling mechanism and $LiCoPO_4$ has two ME domains. All these samples show nonreciprocal directional dichroism. The study helps to clarify the fundamentals of nonreciprocal phenomena and paves the way to discovering of novel materials where the nonreciprocal effect persists in zero field or above the magnetic ordering temperature, needed to make their applications accessible.

The thesis is organized as follows. Section 1 gives some theoretical background about the ME effect in multiferroics. After description of the experimental setup in Section 2, the data analysis is described in Section 3. Finally, the main experimental results obtained by the author are summarized in Section 4, followed by main achievements in Section 5 and conclusions in 6.

1 Theoretical Principles

1.1 Multiferroics

Multiferroics are materials that exhibit two or more primary ferroic orders - ferromagnetism, ferroelectricity, ferroelasticity or ferrotoroidicity - in the same phase [15] (see Fig. 1). In a broader meaning, non-primary orderings like antiferromagnetism are also included. Most commonly studied multiferroics combine ferroelectricity with (anti)ferromagnetism and these are the subject for this thesis. One of the most interesting effects in multiferroics is the magnetoelectric (ME) coupling where electric field ($\mathbf{E}$) can control the magnetization ($\mathbf{M}$) and the magnetic field ($\mathbf{H}$) can control the polarization ($\mathbf{P}$) [3, 16, 17]. Materials with ME coupling are particularly attractive for future technologies because the interplay between electricity and magnetism can be exploited in electronically controlled spintronic devices [18–22].

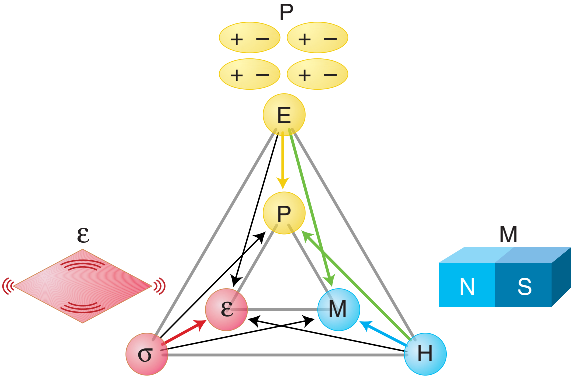

Figure 1: Electric field E, magnetic field H and stress σ control the electric polarization P, magnetization M and strain ε, respectively. In a ferroic material, M, P or ε are spontaneously formed to produce ferromagnetism, ferroelectricity (or ferroelasticity), respectively. Additional interactions may appear in multiferroics with several ferroic orders. Cross correlation between electric and magnetic properties is known as ME effect and shown with green arrows. Figure reproduced from [23].

The multiferroic property is closely linked to symmetry. The primary ferroic properties can be characterized by their behavior under space and time inversion. Space inversion will reverse the direction of polarization $\mathbf{P}$ while leaving the magnetization $\mathbf{M}$ invariant. Time reversal, in turn, will change the sign of $\mathbf{M}$, while the sign of $\mathbf{P}$ remains invariant. If material has spontaneous $\mathbf{M}$ or spontaneous $\mathbf{P}$ the time reversal or space inversion symmetry must be broken. Only ME multiferroics break both symmetries as can be seen in Fig. 2.

Multiferroics come in single-phase and composite varieties [25]. Single-phase multiferroics combine ferroelectric and magnetic properties intrinsically whereas composite multiferroics consist of regions of ferroelectric and magnetic phases in close proximity. The ME effect could be mediated at the boundary between the two phases by strain or exchange bias in composite multiferroics. The composite compounds show a more promising future for applications [22]. However, studying single-phase multiferroics is important to understand the origin of coupling between ferroic orders in more detail so that better composite multiferroics could be engineered. This thesis will only focus on single-phase multiferroics.

Multiferroics are classified into two groups – type-I and type-II multiferroics [26]. The first group includes multiferroics in which magnetism and ferroelectricity have different

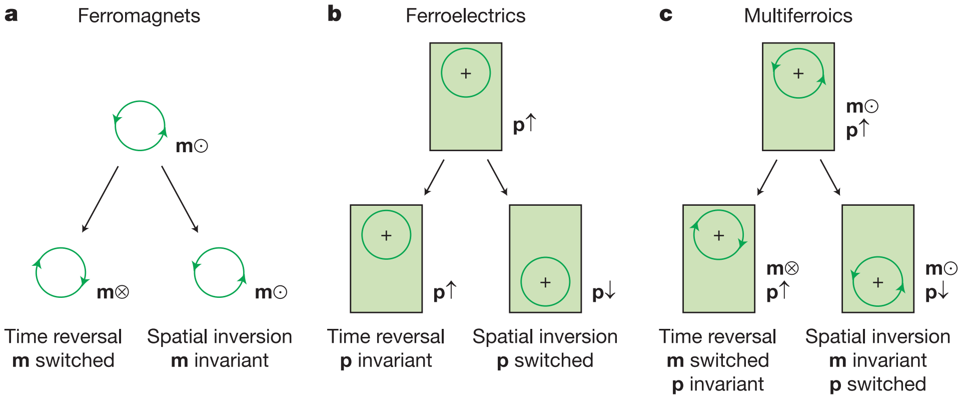

*Figure 2: (a) The local magnetic moment **m** may be represented classically by a charge that dynamically traces an orbit, as indicated by the arrowheads. A spatial inversion produces no change, but time reversal switches the orbit and thus **m**. Consequently ferromagnetic materials do not possess time reversal symmetry. (b) The local dipole moment **p** may be represented by a positive point charge that lies asymmetrically within a crystallographic unit cell that has no net charge. There is no net time dependence, but spatial inversion reverses **p**. Correspondingly ferroelectrics break the spatial inversion symmetry. (c) Multiferroics that are both ferromagnetic and ferroelectric possess neither symmetry. Figure reproduced from [24].*

origins and occur independently of each other, although they have some coupling between them. Usually ferroelectricity appears at higher temperatures than magnetism and the spontaneous polarization $\mathbf{P}$ is quite large ($\mathbf{P}$ $\sim$10–100 μC/cm^2). BiFeO$_3$ is one of the most widely known type-I multiferroics. It is both antiferromagnetic and ferroelectric and it's Curie and Néel temperatures are well above room temperature, T_C=1103 K [27] and T_N=643 K, respectively [28]. In type-II multiferroics, also called magnetism-driven multiferroics, ferroelectricity is caused by magnetism, therefore having a strong coupling between them. However, these materials tend to have smaller polarization and the transition temperatures are substantially below the room temperature. Notable type-II multiferroics are TbMnO$_3$ [29] and DyMnO$_3$ [30].

Coexistence of ferroelectricity and ferromagnetism is hard to come by. Usually, magnetic ordering requires a partially filled *d* or *f* shell which is often the case for transition metals and rare earth metals. Alternatively, electrical polarization requires empty *d* shells. Furthermore, ferroelectrics tend to be insulators. Therefore the coexistence of ferroelectricity and ferromagnetism is rare and usually occurs when the origin of electrical polarization has some alternate microscopic mechanism [31]. Some examples of this alternative mechanism are discussed in section 1.3.

1.2 Magnetoelectric Effect in Multiferroics

ME effect enables the control of polarization ($\mathbf{P}$) by a magnetic field ($\mathbf{H}$) and the control of magnetization ($\mathbf{M}$) by an electric field ($\mathbf{E}$). In linear ME effect, the induced electric polarization or magnetization is proportional to the applied magnetic or electric field, respectively. This can be expressed as

$$\begin{aligned} \mathbf{P} &= \hat{\alpha}^{em}\mathbf{H} \\ \mu_0\mathbf{M} &= \hat{\alpha}^{me}\mathbf{E}, \end{aligned} \tag{1}$$

where tensors $\hat{\alpha}^{em}$ and $\hat{\alpha}^{me}$ denote linear electromagnetic and magnetoelectric susceptibilities, respectively, and μ_0 is the magnetic permeability of vacuum. Most research on the ME effect is focused on the linear ME effect and it is generally accepted that the prefix "linear" be omitted. In the static case, the two susceptibility tensors are connected by the Kubo formula according to the relation

$$\hat{\alpha}^{em} = (\hat{\alpha}^{me})^T, \tag{2}$$

where T is the matrix transpose operator. It is also clear from Eq. 1 that the susceptibility tensors $\hat{\alpha}^{me}$ and $\hat{\alpha}^{em}$ can be finite only in materials without the time reversal and spatial inversion symmetry, as the vector quantities connected by these tensors transform differently upon these two symmetry operations. Thermodynamic stability constraints the ME tensor elements even further:

$$|\hat{\alpha}^{me}_{ij}| \leq \sqrt{\hat{\chi}^{ee}_{ii}\hat{\chi}^{mm}_{jj}}, \tag{3}$$

which means the ME coefficient magnitudes are limited to the geometric means of the dielectric and magnetic susceptibility components [32,33]. Therefore, only materials with simultaneous electric and magnetic order can have large ME susceptibilities.

The linear ME effect was described theoretically [34] and confirmed experimentally [35] in 1960 for Cr_2O_3. The first successful observation of the magnetoelectric effect led to a big excitement because of the possible applications of the cross-correlation between the electric and magnetic properties of matter. However, there was little progress on this topic for several decades because of the weakness of the ME effect. There has been renewed interest in ME effect since the beginning of the 21st century with an impressive amount of publications. The sudden increase of interest has partly to do with the realization how useful a ME material would be for applications [36–38].

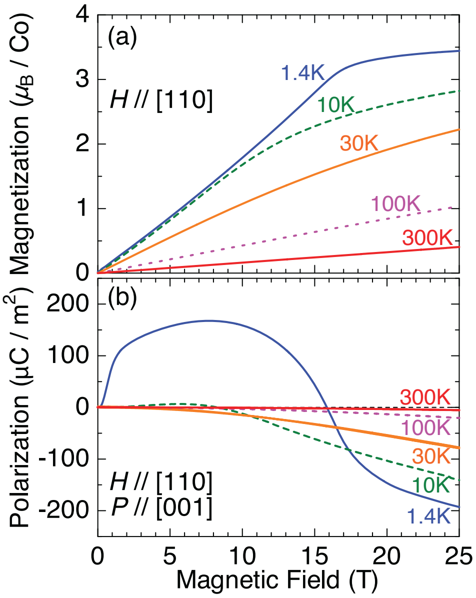

Figure 3: (a) Magnetization along the [110] and (b) electric polarization along [001] direction in $Sr_2CoSi_2O_7$ as a function of applied magnetic field along the [110] direction at different temperatures. Figure reproduced from [39].

Fig. 3 shows an example of static ME effect in a multiferroic crystal. $Sr_2CoSi_2O_7$ has a canted antiferromagnetic order below the the Néel temperature, T_N=7 K. In this ordered phase, the spins are canted by the magnetic field and induce a net electric polarization. As the field increases, the spins become more and more parallel and P changes sign. Above T_N=7 K the spins are randomly oriented and $P \approx 0$. As the magnetic field increases it aligns spins leading to finite P. Therefore, the ME effect is recovered in high fields above the Néel temperature. See more discussion about $Sr_2CoSi_2O_7$ in section 4.2.

1.2.1 Nonreciprocal Directional Dichroism

Nonreciprocal directional dichroism (NDD) is a property of a material to have different absorption coefficients for counterpropagating light beams, Ref. [40] and Eq 16. This effect was first observed for the exciton transitions of the polar semiconductor CdS with wurtzite structure in 1960 [5] but only in 1997 it was recognized as a general magnetooptical phenomenon of non-centrosymmetric materials [6,7]. Recent studies on multiferroics have found strong directional dichroism [8] and, what is more, one way transparency [41]. The largest directional dichroism in multiferroics is at terahertz (THz) frequencies that can boost terahertz photonics in the future [8].

There are two different cases of NDD – magnetochiral dichroism (MChD) [6] and toroidal dichroism. In the first case, the absorption coefficient is different for light propagation along and opposite the magnetization of chiral magnet, $\mathbf{k} \parallel \mathbf{M}$ [7]. In the latter case, NDD occurs in the direction $\mathbf{k} \parallel \mathbf{P} \times \mathbf{M}$, where $\mathbf{P}$ is the ferroelectric polarization and $\mathbf{M}$ is the magnetization of the material. NDD can be finite only when both the time-reversal, operator $\hat{\mathbf{t}}$, and spatial inversion, operator $\hat{\bar{\mathbf{1}}}$, symmetries are broken as these symmetry operations interconnect the light beams traveling in opposite directions, $\hat{\mathbf{t}}\mathbf{k} = -\mathbf{k}$ and $\hat{\bar{\mathbf{1}}}\mathbf{k} = -\mathbf{k}$. This follows from the Maxwell Eqs. (11) and (12) which do not change upon application of $\hat{\mathbf{t}}$ or $\hat{\bar{\mathbf{1}}}$ as $\hat{\mathbf{t}}\mathbf{B}_\omega = -\mathbf{B}_\omega$ (same for $\mathbf{H}_\omega$) and $\hat{\mathbf{t}}\mathbf{E}_\omega = \mathbf{E}_\omega$ (same for $\mathbf{D}_\omega$) or $\hat{\bar{\mathbf{1}}}\mathbf{B}_\omega = \mathbf{B}_\omega$ (same for $\mathbf{H}_\omega$) and $\hat{\bar{\mathbf{1}}}\mathbf{E}_\omega = -\mathbf{E}_\omega$ (same for $\mathbf{D}_\omega$). The operator ∇ is time-reversal invariant and $\hat{\bar{\mathbf{1}}}\nabla = -\nabla$. Symmetry conditions for nonreciprocal light propagation in magnetic crystals are given in [42].

When light beams travel in a ME material, for a beam propagating in one direction the oscillating magnetization generated by the electric field of the light can enhance the conventional magnetization component induced by the magnetic field of light, whereas these two terms interfere destructively for the counterpropagating beam since the relative phase of the electric and magnetic fields of light changes by π when reversing the propagation direction $\mathbf{k}$ to $-\mathbf{k}$, as can be seen from Maxwell Eqs. 12. As follows, we explain the non-reciprocal directional dichroism in more detail.

1.2.2 Dynamic Magnetoelectric Effect and Nonreciprocal Directional Dichroism

To understand the dynamic ME effect it is the best to start from constitutive relations [43]. These are necessary to describe the relation between macroscopic averaged fields, electric displacement $\mathbf{D}$ and magnetic field $\mathbf{H}$, and electric field $\mathbf{E}$ and magnetic induction $\mathbf{B}$:

$$\begin{aligned} \mathbf{D} &= \varepsilon_0\mathbf{E} + (\mathbf{P} + \ldots), \\ \mathbf{H} &= \frac{1}{\mu_0}\mathbf{B} - (\mathbf{M} + \ldots). \end{aligned} \tag{4}$$

The quantities in the brackets are spatial averages of microscopic bound charges and currents. Here, only the microscopically averaged electric dipoles, electric polarization $\mathbf{P}$, and magnetic dipoles, magnetization $\mathbf{M}$, are taken into account and the higher order terms $(\dots)$, like electric quadrupoles, are omitted.

The electric polarization and magnetization depend on fields in general, $\mathbf{P}(\mathbf{E},\mathbf{B})$ and $\mathbf{M}(\mathbf{E},\mathbf{B})$. We expand $\mathbf{P}$ and $\mathbf{M}$ up to the first order in powers of oscillating fields $\mathbf{E}_\omega$ and $\mathbf{B}_\omega$,

$$\begin{aligned} \mathbf{P}_\omega &= \tilde{\chi}^{ee}(\omega)\mathbf{E}_\omega + \tilde{\chi}^{em}(\omega)\mathbf{B}_\omega, \\ \mathbf{M}_\omega &= \tilde{\chi}^{mm}(\omega)\mathbf{B}_\omega + \tilde{\chi}^{me}(\omega)\mathbf{E}_\omega, \end{aligned} \tag{5}$$

where the *frequency-dependent* susceptibilities are

$$\begin{aligned} \tilde{\chi}^{ee}(\omega) &= \left.\frac{\partial \mathbf{P}_\omega}{\partial \mathbf{E}_\omega}\right|_{\mathbf{E}_\omega=0}, & \tilde{\chi}^{mm}(\omega) &= \left.\frac{\partial \mathbf{M}_\omega}{\partial \mathbf{B}_\omega}\right|_{\mathbf{B}_\omega=0}, \\ \tilde{\chi}^{em}(\omega) &= \left.\frac{\partial \mathbf{P}_\omega}{\partial \mathbf{B}_\omega}\right|_{\mathbf{B}_\omega=0}, & \tilde{\chi}^{me}(\omega) &= \left.\frac{\partial \mathbf{M}_\omega}{\partial \mathbf{E}_\omega}\right|_{\mathbf{B}_\omega=0}. \end{aligned} \tag{6}$$

For the rest of the thesis we drop the frequency dependence in the notation of susceptibilities.

Inserting (5) into constitutive relations (4) we get constitutive relations for the alternating electromagnetic fields:

$$\begin{aligned} \mathbf{D}_\omega &= \varepsilon_0\Big(1+\frac{\tilde{\chi}^{ee}}{\varepsilon_0}\Big)\mathbf{E}_\omega + \mu_0\tilde{\chi}^{em}\mathbf{H}_\omega, \\ \mathbf{B}_\omega &= \mu_0(1+\mu_0\tilde{\chi}^{mm})\mathbf{H}_\omega + \mu_0\tilde{\chi}^{me}\mathbf{E}_\omega, \end{aligned} \tag{7}$$

where we assumed $\mu_0\tilde{\chi}^{mm} \ll 1$ for the frequency-dependent $\tilde{\chi}^{mm}$.

The last two equations can be cast into a more familiar form with dimensionless susceptibilities $\hat{\chi}^{mm}$, $\hat{\chi}^{ee}$, $\hat{\chi}^{em}$, and $\hat{\chi}^{me}$,

$$\begin{aligned} \mathbf{D}_\omega &= \varepsilon_0(1+\hat{\chi}^{ee})\mathbf{E}_\omega + \sqrt{\varepsilon_0\mu_0}\,\hat{\chi}^{em}\mathbf{H}_\omega, \\ \mathbf{B}_\omega &= \mu_0(1+\hat{\chi}^{mm})\mathbf{H}_\omega + \sqrt{\varepsilon_0\mu_0}\,\hat{\chi}^{me}\mathbf{E}_\omega. \end{aligned} \tag{8}$$

The relation between dimensionless susceptibilities and susceptibilities defined as derivatives of $\mathbf{P}$ and $\mathbf{M}$ in (6) is

$$\begin{aligned} \hat{\chi}^{ee} &= \frac{1}{\varepsilon_0}\tilde{\chi}^{ee}, & \hat{\chi}^{mm} &= \mu_0\tilde{\chi}^{mm}, \\ \hat{\chi}^{em} &= \sqrt{\frac{\mu_0}{\varepsilon_0}}\,\tilde{\chi}^{em}, & \hat{\chi}^{me} &= \sqrt{\frac{\mu_0}{\varepsilon_0}}\,\tilde{\chi}^{me}. \end{aligned} \tag{9}$$

Equally, dielectric permittivity and magnetic permeability tensors are used:

$$\begin{aligned} \hat{\varepsilon} &= 1+\hat{\chi}^{ee}, \\ \hat{\mu} &= 1+\hat{\chi}^{mm}. \end{aligned} \tag{10}$$

The Maxwell equations in the non-conducting medium are [43]

$$\begin{aligned} \nabla\cdot\mathbf{B} &= 0, & \nabla\times\mathbf{E}+\frac{\partial\mathbf{B}}{\partial t} &= 0 \\ \nabla\cdot\mathbf{D} &= 0, & \nabla\times\mathbf{H}-\frac{\partial\mathbf{D}}{\partial t} &= 0. \end{aligned} \tag{11}$$

Lets consider a plane wave $\mathbf{A}(\mathbf{r},t)=\mathbf{A}_\omega\exp[i(\mathbf{k}\cdot\mathbf{r}-\omega t)]$ where $\mathbf{k}$ is a wavevector of the plane wave with an amplitude $\mathbf{A}_\omega$ and frequency ω. Then, from the Maxwell equations 11 for an insulating material we get the relations between the amplitudes of the plane-wave electromagnetic radiation and ω and $\mathbf{k}$:

$$\begin{aligned} \mathbf{k}\cdot\mathbf{B}_\omega &= 0, & \mathbf{k}\times\mathbf{H}_\omega &= -\omega\mathbf{D}_\omega, \\ \mathbf{k}\cdot\mathbf{D}_\omega &= 0, & \mathbf{k}\times\mathbf{E}_\omega &= \omega\mathbf{B}_\omega. \end{aligned} \tag{12}$$

Using constitutive relations (8) for $\mathbf{D}_\omega$ and $\mathbf{B}_\omega$, the right-hand equations of (12) can be reduced to six unknown components of $\mathbf{E}_\omega$ and $\mathbf{H}_\omega$. The eigenvalues of this set of equations for a given propagation direction $\mathbf{k}$ are N^{-1}, inverse of complex index of refraction

$$N\equiv\frac{c}{\omega}|\mathbf{k}|, \tag{13}$$

where c is the speed of light in the vacuum [44]. There will be two sets of solutions, one for $+k$ and the other for $-k$. If the sample is sufficiently thin polarization of linearly polarized light propagating through the sample is nearly preserved and the index of refraction can be written as [41]:

$$N^{\pm}_{\delta,\gamma}(\omega)=\sqrt{\varepsilon_{\delta\delta}(\omega)\mu_{\gamma\gamma}(\omega)}\pm\frac{1}{2}\left[\chi^{me}_{\gamma\delta}(\omega)+\chi^{em}_{\delta\gamma}(\omega)\right], \tag{14}$$

where the δ and γ coordinate axes are parallel to the direction of $\mathbf{E}_\omega$ and $\mathbf{B}_\omega$. $\varepsilon_{\delta\delta}(\omega)$ and $\mu_{\gamma\gamma}(\omega)$ are diagonal components of the dielectric permittivity and the magnetic permeability tensors. This formula shows that the refractive index $N^{\pm}$ is different for waves propagating in opposite directions if ME susceptibility is non-zero. Therefore, the absorption coefficient proportional to the imaginary part of the complex index of refraction,

$$\alpha^{\pm}_{\delta,\gamma}(\omega)=\frac{2\omega}{c}\Im N^{\pm}_{\delta,\gamma}(\omega), \tag{15}$$

is different for $+k$ and $-k$ propagation directions. The difference in the imaginary part of the N^{+} and N^{-} refractive indices gives rise to the difference in the absorption coefficients of counter-propagating waves [45], termed as directional dichroism:

$$\Delta\alpha(\omega)=\alpha^{+}(\omega)-\alpha^{-}(\omega)=\frac{2\omega}{c}\Im\left[\chi^{me}_{\gamma\delta}(\omega)-\left\{\chi^{me}_{\gamma\delta}(\omega)\right\}'\right]. \tag{16}$$

Here the time-reversal operation $\{\ldots\}'$ relates ME and EM susceptibility tensors: $\chi^{em}_{\delta\gamma}=-\{\chi^{me}_{\gamma\delta}\}'$, Eq. 20. It is obvious that time-reversal odd components of ME tensor contribute to directional dichroism. These are, see Eq. 21 and following discussion, real components of matrix element products, $\Re(\langle m|M|n\rangle\langle n|P|m\rangle)$.

1.2.3 Microscopic Description of the Dynamic Magnetoelectric Effect

Kubo formula defines the microscopic description of the linear response of a quantum system to external stimuli [46]. For the frequency dependence of the electric, magnetic and ME susceptibility tensor, the finite-temperature Kubo formula reads as, see e.g. [45]:

$$\begin{aligned} \chi^{ee}_{\gamma\delta}(z) &= -\frac{V_c}{\varepsilon_0\hbar}\sum_{m,n}\frac{e^{-\beta\hbar\omega_n}-e^{-\beta\hbar\omega_m}}{Z}\frac{\langle n|P_\gamma|m\rangle\langle m|P_\delta|n\rangle}{z-\omega_m+\omega_n}, \\ \chi^{mm}_{\gamma\delta}(z) &= -\frac{\mu_0 V_c}{\hbar}\sum_{m,n}\frac{e^{-\beta\hbar\omega_n}-e^{-\beta\hbar\omega_m}}{Z}\frac{\langle n|M_\gamma|m\rangle\langle m|M_\delta|n\rangle}{z-\omega_m+\omega_n}, \\ \chi^{me}_{\gamma\delta}(z) &= -\frac{V_c}{\hbar}\sqrt{\frac{\mu_0}{\varepsilon_0}}\sum_{m,n}\frac{e^{-\beta\hbar\omega_n}-e^{-\beta\hbar\omega_m}}{Z}\frac{\langle n|M_\gamma|m\rangle\langle m|P_\delta|n\rangle}{z-\omega_m+\omega_n}, \end{aligned} \tag{17}$$

respectively, where $z = \omega + i\varepsilon$ is the imaginary frequency and $\varepsilon \to 0+$, M_γ and P_δ are the magnetic and electric dipole density operators, $|m\rangle$ and $|n\rangle$ are eigenstates of the unperturbed system with energies of $\hbar\omega_m$ and $\hbar\omega_n$, respectively, $\beta = (k_B T)^{-1}$ is the inverse temperature, V_c is the volume of the unit cell and $Z = \sum_k e^{-\beta\hbar\omega_k}$ is statistical sum.

In the zero-temperature limit the Boltzmann factors $e^{-\beta\hbar\omega_n} Z^{-1}$ vanish except for the zero energy ground state $n = 0$. The real and imaginary parts of the ME susceptibility $\chi^{me}_{\gamma\delta}(\omega)$ can be separated from each other using the $\lim\limits_{\varepsilon\to 0} \frac{1}{x+i\varepsilon} \equiv \mathscr{P}\frac{1}{x} - i\pi\delta(x)$ identity, see e.g. [45]:

$$\begin{aligned}
\Re\chi^{me}_{\gamma\delta}(\omega) = -\frac{V_c}{\hbar}\sqrt{\frac{\mu_0}{\varepsilon_0}}\sum_m \Bigg[&\mathscr{P}\frac{2\omega_m \Re\left(\langle 0|M_\gamma|m\rangle \langle m|P_\delta|0\rangle\right)}{\omega^2 - \omega_m^2} + \\
&+\pi\Im\left(\langle 0|M_\gamma|m\rangle \langle m|P_\delta|0\rangle\right)\left(\delta(\omega-\omega_m) - \delta(\omega+\omega_m)\right)\Bigg], \\
\Im\chi^{me}_{\gamma\delta}(\omega) = -\frac{V_c}{\hbar}\sqrt{\frac{\mu_0}{\varepsilon_0}}\sum_m \Bigg[&\mathscr{P}\frac{2\omega \Im\left(\langle 0|M_\gamma|m\rangle \langle m|P_\delta|0\rangle\right)}{\omega^2 - \omega_m^2} - \\
&-\pi\Re(\langle 0|M_\gamma|m\rangle \langle m|P_\delta|0\rangle)(\delta(\omega-\omega_m) - \delta(\omega+\omega_m))\Bigg].
\end{aligned} \tag{18}$$

Here, in addition to separation of $\hat{\chi}^{em}$ into real and imaginary parts, the real and imaginary parts of matrix element products, $\langle 0|M_\gamma|m\rangle \langle m|P_\delta|0\rangle$, are introduced. These products bear important properties with respect to the time-reversal operation.

For a time-reversal even (odd) operator $A(+)$ ($A(-)$) it holds [40, p. 219]

$$\{\langle m|A(\pm)|n\rangle\}' = \pm\langle n|A(\pm)|m\rangle, \tag{19}$$

independent of A being Hermitian ($\langle m|A|n\rangle^* = \langle n|A|m\rangle$), anti-Hermitian ($\langle m|A|n\rangle^* = -\langle n|A|m\rangle$), or non-Hermitian.

Using (19) and M time-reversal odd and P time-reversal even, it follows from (18) that ME and electromagnetic susceptibility tensors are related by time-reversal operation,

$$\chi^{em}_{\delta\gamma} = -\{\chi^{me}_{\gamma\delta}\}'. \tag{20}$$

Furthermore, for Hermitian operators as P and M, taking the complex conjugate of the time-reversed state matrix elements we have

$$\begin{aligned}
\left[\{\langle m|M|n\rangle \langle n|P|m\rangle\}'\right]^* &= -\left[\langle m|P|n\rangle \langle n|M|m\rangle\right]^* \\
&= -\langle m|M|n\rangle \langle n|P|m\rangle.
\end{aligned} \tag{21}$$

Considering that upon complex conjugation only the imaginary part of a variable changes sign, we get that $\Re(\langle m|M|n\rangle \langle n|P|m\rangle)$ is time-reversal odd and $\Im(\langle m|M|n\rangle \langle n|P|m\rangle)$ is time-reversal even. Therefore, only $\Re(\langle m|M|n\rangle \langle n|P|m\rangle)$ contributes to the directional dichroism, Eq. 16.

Another useful relation between the components of tensors $\hat{\chi}^{mm}$ and $\hat{\chi}^{ee}$ can be derived using the hermiticity of an operator A, [40, p.92],

$$\langle m|A_\delta|n\rangle \langle n|A_\gamma|m\rangle = \langle m|A_\gamma|n\rangle^* \langle n|A_\delta|m\rangle^*. \tag{22}$$

The relation is

$$\begin{aligned}
\Re\left(\langle m|A_\delta|n\rangle \langle n|A_\gamma|m\rangle\right) &= \Re\left(\langle m|A_\gamma|n\rangle \langle n|A_\delta|m\rangle\right), \\
\Im\left(\langle m|A_\delta|n\rangle \langle n|A_\gamma|m\rangle\right) &= -\Im\left(\langle m|A_\gamma|n\rangle \langle n|A_\delta|m\rangle\right),
\end{aligned} \tag{23}$$

where $A_\gamma = M_\gamma$ or $A_\gamma = P_\gamma$.

In the limit of $\omega \to 0$, Eq. 18 describes the static ME susceptibility. Firstly, the term in the imaginary part of $\chi^{me}_{\gamma\delta}$ proportional to ω becomes zero and secondly, the delta-functions cancel. Thus, the dc ME susceptibility is real and is proportional to the real part of the matrix elements product:

$$\chi^{me}_{\gamma\delta}(0) = \frac{2V_c}{\hbar}\sqrt{\frac{\mu_0}{\varepsilon_0}}\sum_m \frac{\Re(\langle 0|M_\gamma|m\rangle \langle m|P_\delta|0\rangle)}{\omega_m}. \tag{24}$$

1.2.4 Magnetoelectric Sum Rule

From the spectrum of the dynamic ME effect one can also determine the static ME coupling using the ME susceptibility sum rule [45].

The Kramers-Kronig relations connect the real ($\Re$) and imaginary ($\Im$) parts of a causal frequency-dependent linear response function, see e. g. [47, Appendix L.1]:

$$\begin{aligned}\Re\chi(\omega) &= \frac{1}{\pi}\mathscr{P}\int_{-\infty}^{\infty}\frac{\Im\chi(\omega')}{\omega'-\omega}\mathrm{d}\omega',\\ \Im\chi(\omega) &= -\frac{1}{\pi}\mathscr{P}\int_{-\infty}^{\infty}\frac{\Re\chi(\omega')}{\omega'-\omega}\mathrm{d}\omega'.\end{aligned} \tag{25}$$

Often, only either the real or imaginary part of the susceptibility $\chi(\omega)$ or the amplitude and not the phase can be measured experimentally and the Kramers-Kronig transformation is used to obtain the entire complex response function [48].

In the limit $\omega \to 0$ Eq. 25 can be simplified to the following form:

$$\begin{aligned}\Re\chi(\omega=0) \equiv \chi(0) &= \frac{2}{\pi}\mathscr{P}\int_{0}^{\infty}\frac{\Im\chi(\omega)}{\omega}\mathrm{d}\omega,\\ \Im\chi(\omega=0) \equiv 0 &= -\frac{1}{\pi}\mathscr{P}\int_{-\infty}^{\infty}\frac{\Re\chi(\omega)}{\omega}\mathrm{d}\omega.\end{aligned} \tag{26}$$

One can see from Eq. 26 that the static response is determined by the corresponding dynamical susceptibility and the frequency denominator indicates the role of low-energy excitations in the static susceptibility. The main issue with the application of these sum rules is that usually χ^{me} cannot be determined from the optical quantities of the material because contributions to the refractive index from the ME susceptibility, magnetic permeability and dielectric permittivity can't be separated. However, this problem can be circumvented with the introduction of NDD spectrum, Eq. 16, as follows [45].

The general sum rule in Eq. 26 can be reformulated in a more specific way, which directly connects the static ME effect to the NDD spectrum:

$$\chi^{me}_{\gamma\delta}(0) = \frac{c}{2\pi}\mathscr{P}\int_{0}^{\infty}\frac{\Delta\alpha(\omega)}{\omega^2}\mathrm{d}\omega. \tag{27}$$

Here the static ME effect is mostly governed by the NDD of low-energy excitations, since the absorption difference, $\Delta\alpha$, is suppressed by the ω^2 denominator at higher frequencies. Eq. 27 shows that the low frequency electric *and* magnetic dipole active spin excitations dominate in the static ME susceptibility.

1.3 Magnetoelectric Coupling Mechanisms for Type-II Multiferroics

In type II multiferroics the magnetic ordering breaks the inversion symmetry and directly causes the ferroelectricity. These multiferroics are divided into three categories dependent on the specific mechanism responsible for the ferroelectric polarization [49–52]:

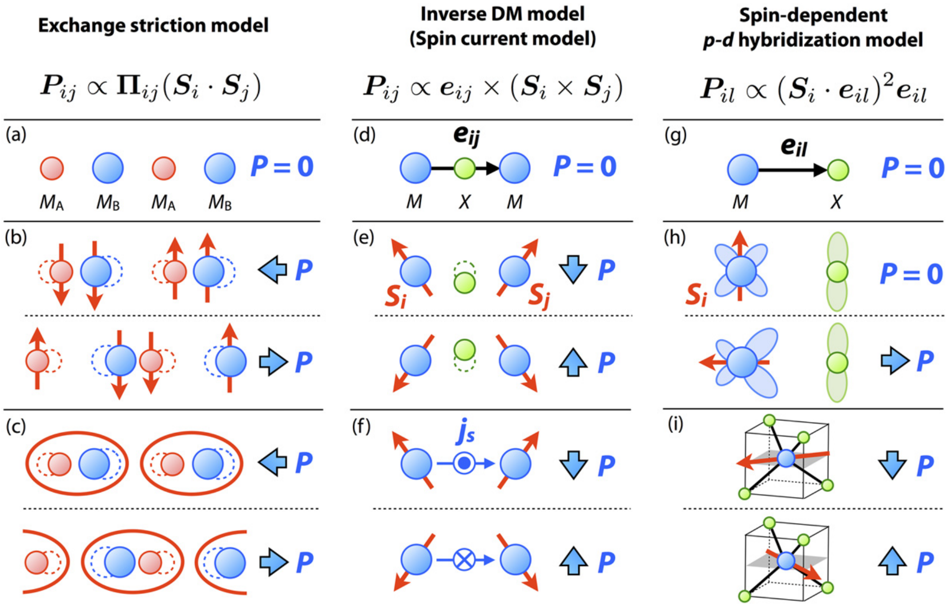
Exchange striction model
$P_{ij} \propto \Pi_{ij}(S_i \cdot S_j)$
Inverse DM model
(Spin current model)
$P_{ij} \propto e_{ij} \times (S_i \times S_j)$
Spin-dependent
p-d hybridization model
$P_{il} \propto (S_i \cdot e_{il})^2 e_{il}$
(a)
M_A
M_B
M_A
M_B
P = 0
(b)
P
P
(c)
P
P
(d)
e_{ij}
M
X
M
P = 0
(e)
S_i
S_j
P
P
(f)
j_s
P
P
(g)
e_{il}
M
X
P = 0
(h)
S_i
P = 0
P
(i)
P
P

Figure 4: Three major mechanisms of ME coupling. (a)-(c) Exchange striction mechanism; (d)-(f) Inverse DM model, also known as spin current mechanism and (g)-(i) spin-dependent p – d *hybridization mechanism. M and X denote magnetic and ligand ions, respectively.* $\mathbf{S}_i$ *and* $\mathbf{S}_j$ *are spin orientations at each magnetic site,* $\mathbf{e}_{ij}$ *and* $\mathbf{e}_{il}$ *are the unit vectors connecting two sites.* $\mathbf{P}$ *indicates the expected direction of magnetically induced electric polarization. Figure reproduced from [52]*

the symmetric exchange striction [53, 54], the inverse Dzyaloshinskii-Moriya interaction or spin current mechanism [55–57], and the spin-dependent *p* – *d* hybridization mechanism [50, 51, 58] (see Fig. 4).

1.3.1 Exchange Striction Mechanism

The symmetric exchange striction of a spin pair $\mathbf{S}_i$ and $\mathbf{S}_j$ can induce polarization along a specific crystallographic direction $\mathbf{e}_{ij}$:

$$\mathbf{P}_{i,j} = P^{\mathrm{es}} \mathbf{e}_{ij} (\mathbf{S}_i \cdot \mathbf{S}_j). \tag{28}$$

In a frustrated magnetic structure the exchange striction shifts ions in a way to optimize their exchange energy. For example, in a chain with nearest-neighbor ferromagnetic and next-nearest neighbor antiferromagnetic interactions the moments with parallel spin will move closer together which may break inversion symmetry and generate electric polarization [18, 26, 59]. Macroscopic polarization is produced when spin modulation is commensurate with the crystal lattice and there is no cancellation over the sum of the bonds over the whole crystal lattice. The magnitude of the induced polarization can be larger compared to the Dzyaloshinskii-Moriya and spin-dependent *p* – *d* hybridization because this mechanism does not involve the relativistic spin-orbit coupling [60]. Exchange striction is argued to be the predominant mechanism for ferroelectricity in YMn_2O_5 [59,61] and $CaBaCo_4O_7$ [62].

1.3.2 Dzyaloshinskii-Moriya Mechanism

Inverse Dzyaloshinskii-Moriya interaction was proposed to couple spin and charge [57]. This interaction, also known as spin current interaction, induces the polarization of the electronic orbitals, without the involvement of the lattice degrees of freedom. Another model was proposed by Sergienko and Dagotto where the Dzyaloshinskii-Moriya interaction changes the *M*-*L*-*M* bond angle resulting in a ferroelectric lattice displacement [55]. Both can be described with the same empirical formula

$$\mathbf{P} = P^{\mathrm{sc}}\mathbf{e}_{ij} \times (\mathbf{S}_i \times \mathbf{S}_j), \tag{29}$$

where unit vector $\mathbf{e}_{ij}$ connects the two spin sites. Prerequisite for induced polarization is that the crystal has to have a non-collinear magnetic structure, i.e. $\mathbf{S}_i \times \mathbf{S}_j$ is finite, like in a spin cycloid in $BiFeO_3$.

Dzyaloshinskii-Moriya mechanism has seen a lot of interest in multiferroics studies because transverse screw spin configurations can always produce spontaneous $\mathbf{P}$ [2]. Strong ME coupling in perovskite type manganites RMnO$_3$ (R=Tb, Dy, $Eu_{1-x}Y_x$) with cycloidal order is caused by Dzyaloshinskii-Moriya interaction [29, 63–65]. $BiFeO_3$ with a spin cycloid has the spin-current mechanism [11, 66]

1.3.3 Spin-dependent Hybridization Mechanism

In åkermanites the electric polarization is not induced by correlations between neighboring spins, thus neither by exchange striction nor Dzyaloshinskii-Moriya mechanism. What is more, the induced electric polarization is present even in the paramagnetic phase if magnetic field is applied [67, 68], as can be seen in Fig. 3. Spin-dependent metal-ligand hybridization mechanism is the microscopic mechanism behind this single-site electric polarization within CoO_4 tetrahedron. Polarization of a magnetic ion surrounded by inversion-breaking oxygen tetrahedron can be expressed as

$$\mathbf{P}_i \sim \sum_{l=1}^{4} (\mathbf{S} \cdot \mathbf{e}_{il})^2 \mathbf{e}_{il}, \tag{30}$$

where $\mathbf{e}_{il}$ is the unit vector from the metal ion i to the l-th oxygen ligand [68]. Cobalt ion in an oxygen tetrahedron is shown in Fig. 5. Electric polarization depends on the orientation of the cobalt spin relative to the Co-O bonds. If the spin is parallel to the bond connecting oxygens O_1 and O_2, the polarization is pointing up. 90 degree rotation of spin inverts the polarization.

One can see in Fig. 3 that the positive polarization at 1.4 K almost disappears at 10 K whereas the magnetization is comparable at 1.4 K and 10 K up to 10 T. However, the polarization above 20 T is similar at these temperatures. This is a clear sign that a large part of the electric polarization is produced by the uniform magnetic moment regardless of the antiferromagnetic spin order. The multiferroic properties of the whole åkermanite family (e.g. $Ba_2CoGe_2O_7$, $Sr_2CoSi_2O_7$) are explained by $p-d$ hybridization [39, 70–72]. The results of $Sr_2CoSi_2O_7$ are discussed in more detail in Section 4.2.

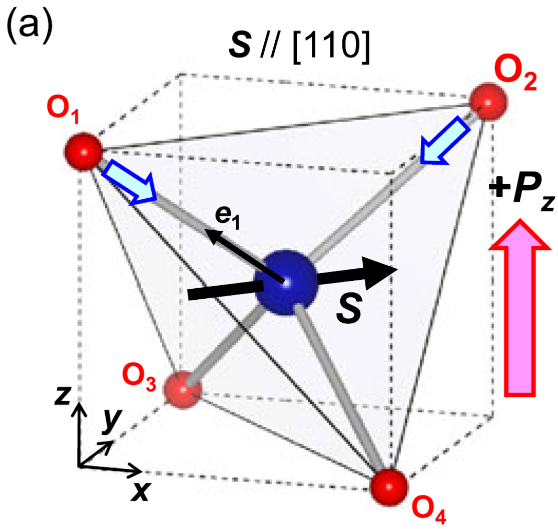

Figure 5: The spin-driven electric polarization in $Sr_2CoSi_2O_7$ due to $\mathrm{p-d}$ hybridization in an oxygen tetrahedron. The spin $\mathbf{S}$ points in a [110] direction and unit vector $\mathbf{e}_i$ points from the magnetic ion to the ith ligand ion. When the spin $\mathbf{S}$ is parallel to the upper oxygen bond O_1–O_2, the polarization points up along [001]. The polarization is reversed when $\mathbf{S}$ is parallel the lower oxygen bond O_3–O_4. Figure reproduced from [69].

2 Experimental Details

This chapter gives an overview of two magneto-optical spectroscopic setups used for this work, TeslaFIR in Tallinn and far-infrared setup in High Magnetic Field Laboratory in Nijmegen. Additionally, some parts of the setup designed and built by the author of this thesis are described in more detail.

2.1 Interferometric Detection with Michelson and Martin-Puplett Interferometers

Fourier transform spectroscopy is a method where spectra are obtained by computational analysis on the interferograms produced by two-beam interferometers. This method is well established and widely used in spectroscopic studies in all research fields. Several textbooks describe the subject in-depth, e.g. [73]. The procedure used in TeslaFIR to obtain spectrum from the measured interferogram follows closely the steps described by Porter and Tanner [74].

A schematic of a two-beam Michelson interferometer is shown in Fig. 6. Modulated intensity $I(x)$ is produced by moving the mirror M$_2$ by a path difference of x. The output intensity for this kind of interferometer for monochromatic light with a wavenumber $k=\frac{1}{\lambda}$ is

$$I(x)=\frac{I_0}{2}\left[1+\cos\left(2\pi kx\right)\right]=\frac{I_0}{2}\left[1+\cos(\Delta)\right]. \tag{31}$$

One can see from Eq. 31 that half of the incident intensity I_0 irradiated by the source gets modulated and is therefore spectrometrically useful. Unfortunately, the dielectric or 50% reflective metallic film beamsplitter in Michelson interferometer relies on interference within the film thickness to enhance the reflectance, and there are difficulties in getting high efficiency over a wide spectral range. The efficiency of a beamsplitter varies periodically with spectral frequency where the period is determined by the film thickness. It is not possible to maintain a good efficiency over more than around an octave of spectral frequency [75], which is a real issue in terahertz spectroscopy.

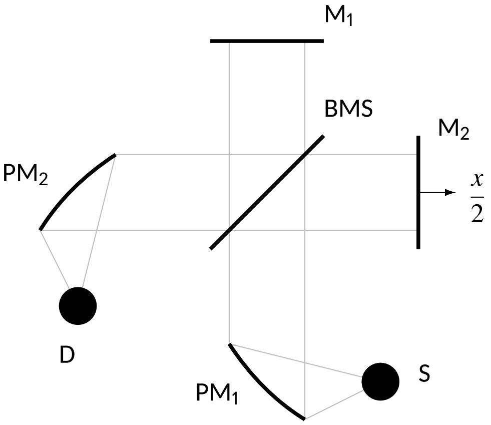

Figure 6: Michelson two-beam interferometer. S – source, D – detector, M$_1$ – stationary mirror, M$_2$ – movable mirror, BMS – beamsplitter, PM$_1$ and PM$_2$ – parabolic mirrors.

The polarizing interferometer was described by D. H. Martin and E. Puplett [76] to solve the inefficiency problem with a Michelson interferometer. A basic Martin-Puplett type interferometer is depicted in Fig. 7. The high efficiency is achieved with the use of a polarizing wire-grid beamsplitter. A wire grid transmits the component of light having electric field perpendicular to the wires and reflects the orthogonal polarization. This description holds if the wavelength λ is longer than the grid spacing d.

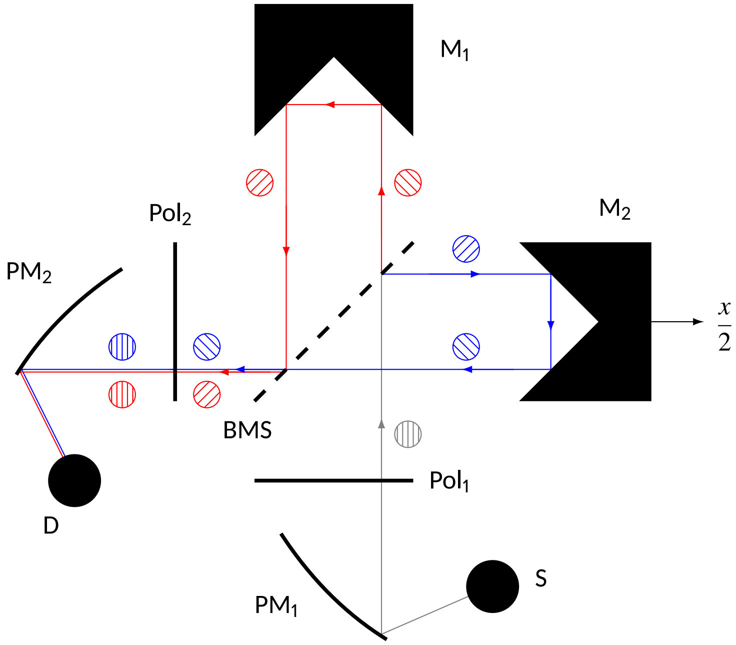

Figure 7: Martin-Puplett interferometer. S – source, D – detector, M$_1$ – stationary roofmirror, M$_2$ – movable roofmirror, BMS – beamsplitter, Pol$_1$ and Pol$_2$ – polarizers, PM$_1$ and PM$_2$ – parabolic mirrors. Polarizers Pol$_1$ and Pol$_2$ transmit light with the electric field vector in the vertical direction (out from the paper plane), while the polarization axis of the BMS is rotated around the beam propagation direction by 45° from the vertical direction. Gray line shows the beampath before the BMS divides it into two beams - the red and the blue. The component of light that was parallel to the BMS wires is reflected (blue path) and the orthogonal polarization is transmitted through the BMS (red path). Polarization is rotated by 90° by reflection from the roof mirror and the beam previously reflected goes through the BMS whereas the beam previously transmitted at the BMS now reflects from it.

Let's examine a monochromatic beam traveling through the Martin-Puplett interferometer in more detail. The $\mathbf{E}$ vector for the light polarized by the linear polarizer Pol$_1$ is divided into two components by the beamsplitter

$$\mathbf{E}_i = a\hat{p}\cos\omega t = \frac{a}{\sqrt{2}}\hat{n}\cos\omega t + \frac{a}{\sqrt{2}}\hat{t}\cos\omega t, \tag{32}$$

where $\hat{p}$ is in the direction of the optical axes of two parallel polarizers Pol$_1$ and Pol$_2$ whereas the angle between $\hat{p}$ and $\hat{n}$ is 45° and $\hat{p}$ and $\hat{t}$ is –45°; $\hat{n}$ and $\hat{t}$ are orthogonal unit vectors. The roofs of the roof mirrors are parallel to polarization directions of polarizers, $\hat{p}$. The beam is reflected back by the roof mirrors which rotate the polarization angle by 90° upon reflection. Now the beamsplitter acts as a reflector for the beam going through the beamsplitter and vice versa which allows the beam to recombine near lossless

$$\mathbf{E}_j = \frac{a}{\sqrt{2}}\hat{n}\cos(\omega t + \Delta_A) + \frac{a}{\sqrt{2}}\hat{t}\cos(\omega t + \Delta_B), \tag{33}$$

where Δ_A and Δ_B are the phase shifts for the beams A (blue) and B (red) in Fig. 7. Because the two beams have traveled different distances, the recombined beam will be elliptically polarized with the ellipticity and the direction of the major axis being determined by the phase differences of the two beams. The cycle-averaged intensity of the beam is [1]

$$\langle \mathbf{E}\cdot\mathbf{E}\rangle \quad = \quad \frac{1}{T}\int_0^T \mathbf{E}\cdot\mathbf{E}\,\mathrm{d}t. \tag{34}$$

For the beam $\mathbf{E}_j$ the cycle-averaged intensity is independent of phase difference $\Delta = \Delta_A - \Delta_B$, $\left\langle \mathbf{E}_j\cdot\mathbf{E}_j\right\rangle = I_p^0$, where $I_p^0 = a^2/2$ is the intensity after Pol$_1$ and $\left\langle \cos^2(\omega t + \Delta)\right\rangle = 1/2$ was used. To create the phase-difference dependent intensity a second polarizer Pol$_2$ is placed at the output of the Martin-Puplett interferometer.

Light, after going through the output polarizer Pol$_2$, is now

$$E_p = \mathbf{E}_j\cdot\hat{p} = \frac{a}{2}\left[\cos\left(\omega t + \Delta_A\right) + \cos\left(\omega t + \Delta_B\right)\right] = a\cos(\omega t + \overline{\Delta})\cos\frac{\Delta}{2}, \tag{35}$$

where $\overline{\Delta} = \frac{\Delta_A+\Delta_B}{2}$. The intensity of the beam after Pol$_2$ is

$$I_p = \left\langle E_p^2\right\rangle = \frac{a^2}{2}\cos^2\frac{\Delta}{2} = \frac{a^2}{4}(1+\cos\Delta) = \frac{I_p^0}{2}(1+\cos\Delta). \tag{36}$$

The beamsplitter in Sciencetech SPS200 spectrometer is made of 0.4 μm thick and 2 μm wide aluminum grid with a 4 μm spacing on a 12 μm Mylar substrate.

2.2 TeslaFIR Experimental Setup

The main experimental setup for terahertz spectroscopy in Tallinn is TeslaFIR. It consists of a Martin-Puplett interferometer, a superconducting 17 T magnet, a ^{4}He cryostat and 0.3 K bolometers. The spectral range is from 100 GHz to 6 THz. Sample temperature can be controlled from 2 K up to 300 K. The system measures the intensity of transmitted or reflected radiation and does not measure the phase shift introduced by the sample. A simplified layout of the TeslaFIR is shown in Fig. 8.

Terahertz radiation is produced by a mercury arc lamp. The quartz envelope of the lamp is transparent below 3 THz to the radiation emitted by the arc plasma [78]. This EM radiation goes through a Martin-Puplett type interferometer and the resulting beam is focused into the 16 mm diameter light pipe leading to the cryostat. Most of the visible and UV radiation is filtered out with a black polyethylene film before entering the cryostat. Stepper-motor controlled polarizer is positioned just before the sample. There are several different probes with different sample orientations and functions. In the Faraday configuration, light propagates parallel to the magnetic field; in the Voigt configuration, it propagates perpendicular to the magnetic field (Fig. 9). The most straightforward one is the Faraday probe where up to six samples can be positioned. This work focuses on two Voigt probes (see section 2.3) where the beam is reflected perpendicular to the magnetic field before going through the sample and then reflected towards the bolometer. Both Voigt probes accept one sample at a time.

---

[1] For the complex representation of the electromagnetic field $\mathbf{E}(\mathbf{r},t) = \mathbf{E}(\mathbf{r})\exp(-i\omega t)$ the cycle-averaged intensity is [77, p. 6] $\langle \Re(\mathbf{E})\cdot\Re(\mathbf{E})\rangle = \frac{1}{2}\Re(\mathbf{E}\cdot\mathbf{E}^*)$. $\Re(\mathbf{E})$ is the real part of $\mathbf{E}$.

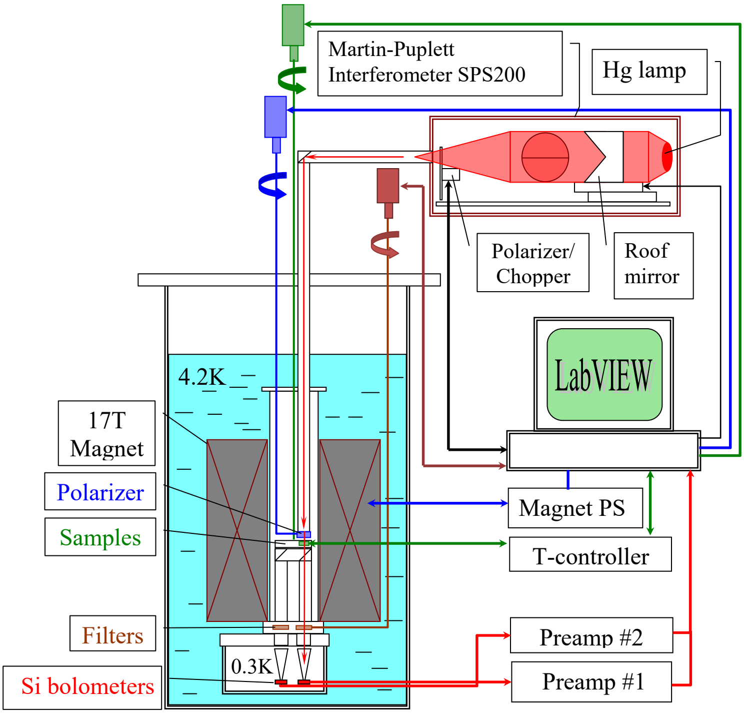

Figure 8: Layout of TeslaFIR spectrometer. Sample chamber, superconducting 17 T solenoid and the 0.3 K bolometer chamber share the same liquid He bath cryostat. The beam path in the sample chamber is shown for the Faraday configuration.

The detection side, that is, the light path after the sample, including the detector, is insensitive to the polarization of light. After the sample, the beam goes through a filter wheel (see section 2.4.) with 8 positions. The filter wheel is immersed in liquid Helium for better cooling, otherwise the filters would warm above liquid He temperature radiating as black body at this elevated temperature. Liquid helium would bubble in the beam path but this can be overcome by pumping down the helium (reducing the equilibrium pressure above the liquid) below 2.17 K to superfluid state where the boiling stops. The filter wheel contains low-pass multi-mesh filters with 0.3, 0.6, 2, 3 and 6 THz cutoffs and a scatter-absorbing Fluorogold [79] with a 1.2 THz cutoff. The filter wheel is described in more detail in Sec. 2.4. An additional fixed-position 6 THz cutoff multi-mesh filter lies on the sample chamber window. The THz light then travels inside the bolometer chamber, which houses two composite bolometers, each consisting of a Si chip mounted on a 5 mm diameter absorber disc made of sapphire and having an anti-reflection coating. The sensitivity of these bolometers operating at 0.3 K is 4.5×10^{7} V/W, two orders of magnitude greater than that of a 4.2 K bolometer. The bolometers are positioned about 29 cm below the field center of a 17 T solenoid, where the magnetic field has only a moderate effect on the bolometers. The electrical signals from the bolometers are amplified by a preamplifier and then digitized by an ADC board. For the absorption measurements one bolometer is used at a time.

2.3 Voigt Probes

In Voigt geometry, the applied magnetic field $\mathbf{B}$ is perpendicular to the beam wavevector $\mathbf{k}$ as shown in Fig. 9(b). This is an additional method to Faraday geometry where the beam is traveling along the magnetic field direction, Fig. 9(a). Specifically, in the Voigt geometry there are two polarizations, $\mathbf{B}_\omega \parallel \mathbf{B}$ and $\mathbf{E}_\omega \parallel \mathbf{B}$, which are not possible in the Faraday geometry. Combining these two methods allows us to determine all the selection rules for light absorption for the crystals in magnetic field. Two different Voigt probes were designed and constructed as part of this work.

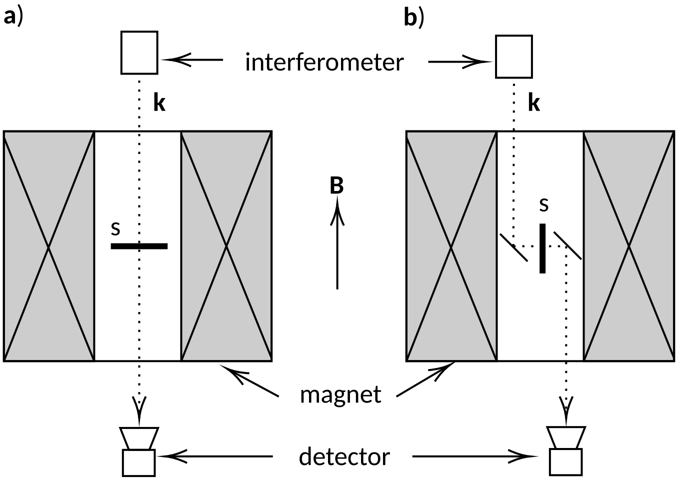

Figure 9: a) Faraday and b) Voigt geometry layouts. Gray is the magnet coil, s *is sample in the center of the magnet,* $\mathbf{B}$ *is the magnetic field in the center of the magnet which can also be in the opposite direction, and* $\mathbf{k}$ *is the beam traveling direction. In Faraday geometry the beam travels through the sample parallel to the magnetic field,* $\mathbf{k} \parallel \mathbf{B}$*. In Voigt geometry the beam is traveling perpendicular to the applied field,* $\mathbf{k} \perp \mathbf{B}$*, which for a solenoid is accomplished with two mirrors.*

2.3.1 Rotating Voigt Probe

The Voigt probe used already before this thesis author's joining the research group at NICPB is called static Voigt probe. In the static Voigt probe the sample is fixed in place for the duration of an experiment. This means two Voigt experiments are needed, $\mathbf{a} \parallel \mathbf{B}$ and $\mathbf{b} \parallel \mathbf{B}$ per one *ab* face sample, costing time and resources. What is more, the sample axis needed to be aligned precisely relative to the magnetic field while assembling the experiment. Therefore another probe, rotating Voigt probe, was designed and constructed (Fig. 10) where the sample is rotated in the cryostat about the light wavevector after the probe has been closed and cooled down. This design allows to choose any angle between the magnetic field and the crystal axis in the plane perpendicular to the light wavevector and also use the magnetic field dependence of spectra to make precise sample alignment relative to $\mathbf{B}$.

On the probe's vertical axis is a shaft connected to the stepper motor at room temperature. On the other end of this shaft is a set of beveled gears turning the rotation axis 90° to be perpendicular to the magnetic field. The bigger gear has a large opening in the center allowing a bearing and lightpipe to be fitted. Sample disk holder is attached to this gear in the center of the magnetic field. Because there are no wires attached to the rotating parts the unlimited rotation of the sample disk holder is possible.

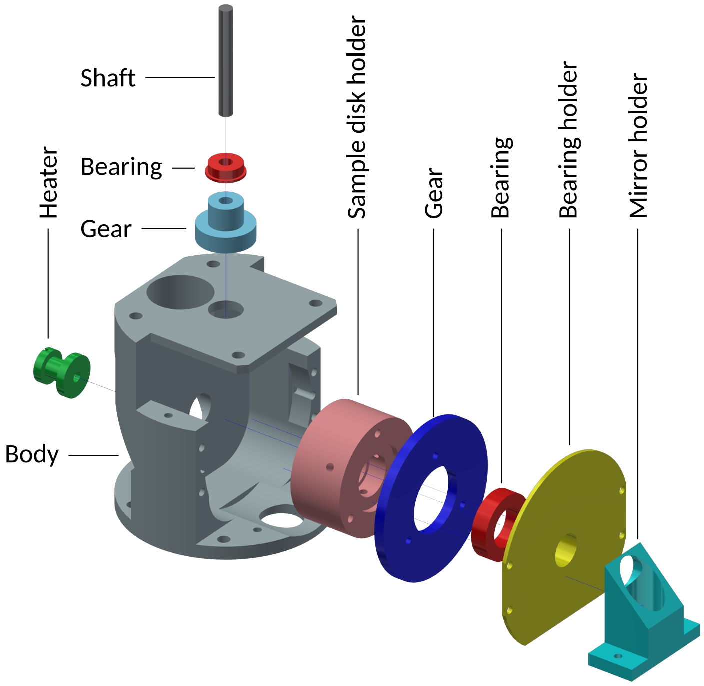

Figure 10: Rotating Voigt probe exploded layout. Fasteners have been omitted for clarity. Light enters the probe from the opening on the top left, is reflected horizontally, passes the sample disk holder and is reflected down towards the bolometer. Mirrors, not shown on the picture, are glued to the ends of the openings on the horizontal optical axis.

Three slip rings are attached to the body of the probe for finding the exact position of the sample disk holder. One slip ring acts as the ground connection between the body and sample disk holder and is always in electrical contact. The other two slip rings, one at a time, are disconnected when a narrow strip of cigarette paper glued on the outer surface of the sample disk holder electrically isolates one of them. These slip rings act as positive and negative end limit switches. An exact sample disk orientation is known when it triggers negative end limit switch and all following rotations are done relative to that position.

Attached to the back of the main body are a thermometer and a heater to control the sample temperature. The heater is made of a supporting copper post onto which a resistance wire is wound with a total resistivity of 60 Ω. Maximum of 50 W of heat can be produced by applying current to the heater. The sample is not that well connected thermally to the heater and thermometer whereas the rest of the probe is. Heater heats up the whole probe and above 10 K the signal is lost because of the thermal radiation overloading the bolometer. Therefore, the heater on the rotating Voigt probe is used only for keeping the sample temperature between 2.5 K to around 7 K.

The main body of the probe was a complex manufacturing job and was outsourced. Aluminum beveled gears and stainless steel bearings were a commercial product. The rest was manufactured in house. All the materials are non-magnetic. The body of the probe and the holder for the larger gear are made from brass whereas the sample disk holder is made out of copper for it’s higher heat conductivity. Mirrors for reflecting the beam are cut from a brass sheet and glued to the probe body and to the mirror holder.

The rotating Voigt probe was designed and built specifically for the experiment described in section 4.1 but it has been the most used Voigt probe since then. A different sample disk holder was later designed, which holds a thermometer and a heater. Although the rotation of the sample holder is limited to around $\pm 60^\circ$ because of the wires attached to it, the temperature of the sample is controlled in much broader range and with higher accuracy.

2.3.2 High-Temperature High-Voltage Voigt Probe

A probe was designed and built for high-temperature (up to 100 K) and high voltage (up to 1500 V) measurements in the Voigt geometry (Fig. 11). The copper sample disk holder (shown in blue) has grooves along the circumference which are filled with nylon line for isolating the sample from the rest of the probe thermally and electrically. One larger groove is filled with resistance wire with resistance of 60 Ω which acts as a heater coil. A Cernox thermometer is mounted near the sample for accurate temperature measurements. The sample disk holder is held in place with nylon screws.

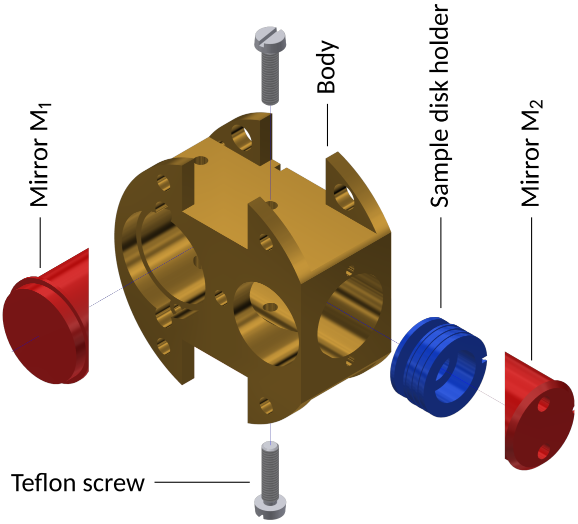

Figure 11: High-temperature high-voltage Voigt probe exploded layout. Fasteners have been omitted for clarity.

To apply high voltage gold wire leads are glued with silver paste to two opposing sides of the sample crystal (see Fig. 13). The gold wires are wrapped in insulating teflon tape and guided to the outside of the probe where a connection with copper wiring is made by pressing the gold wires into indium and soldering the copper wires. For usual sample sizes the electric field can be up to $5{\cdot}10^6$ V·m.

The body of the probe (shown in gold) and mirrors (shown in red) are made of brass for low thermal conductivity. Mirrors are fixed to the body of the probe and reflect the light from parallel the magnetic field to perpendicular (M_1) before the sample and back to parallel the magnetic field again after the sample (M_2). This probe was used for high voltage $LiCoPO_4$ measurements as described in section 4.3.

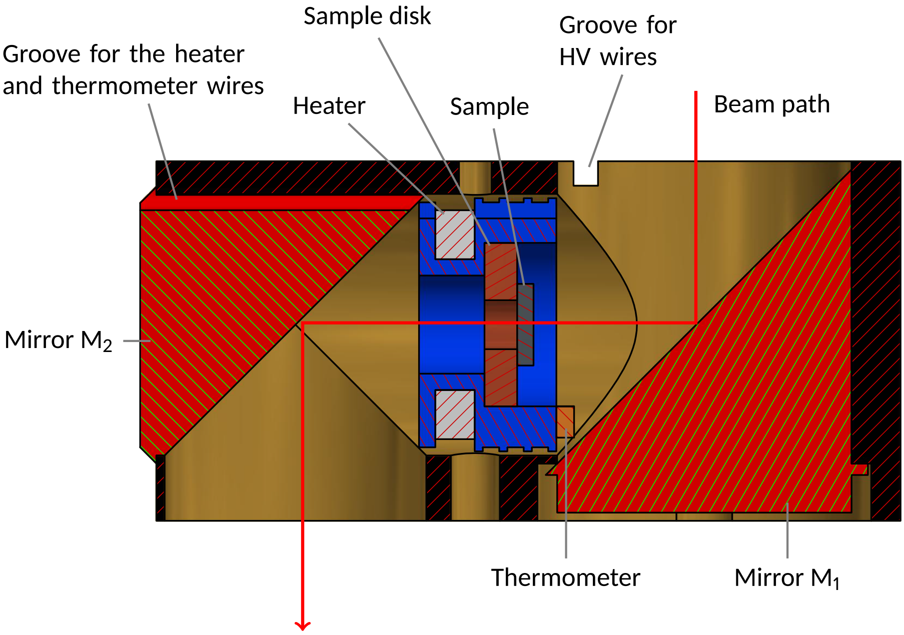
Sample disk
Groove for HV wires
Groove for the heater and thermometer wires
Heater
Sample
Beam path
Mirror M_2
Thermometer
Mirror M_1

Figure 12: High-temperature high-voltage Voigt probe cutaway side view showing the beam path through the probe.

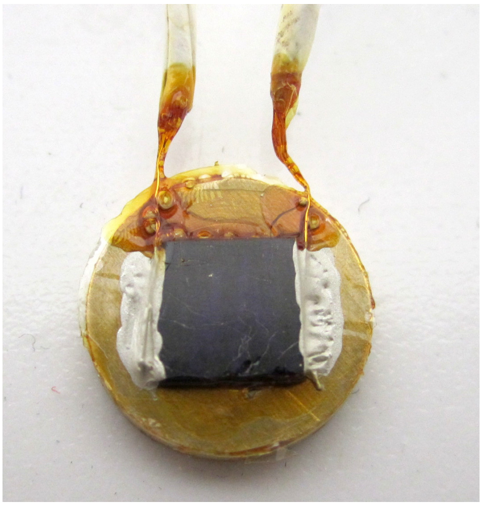

Figure 13: $LiCoPO_4$ sample with gold wires attached for a high voltage experiment. The sample is electrically isolated from the ⌀ 10 mm sample disk by a Mylar film. Gold wires are glued to the sides of the sample with a silver conductive paste and additionally glued with a non-conductive GE varnish to the Mylar film. The wires leaving the sample are wrapped in teflon tape for insulation.

2.4 Filter Wheel

A new rotatable filter wheel was designed and constructed as can be seen in Fig. 14. The previous filter wheel was lacking in reproducibility and reliability. The new design is based on three interlocking gears with the filters mounted on the last largest gear. The gears are rotated by a rod connecting the first smallest gear and a stepper motor outside the cryostat. A limit switch was added to find the precise position of the wheel after starting the stepper motor controller.

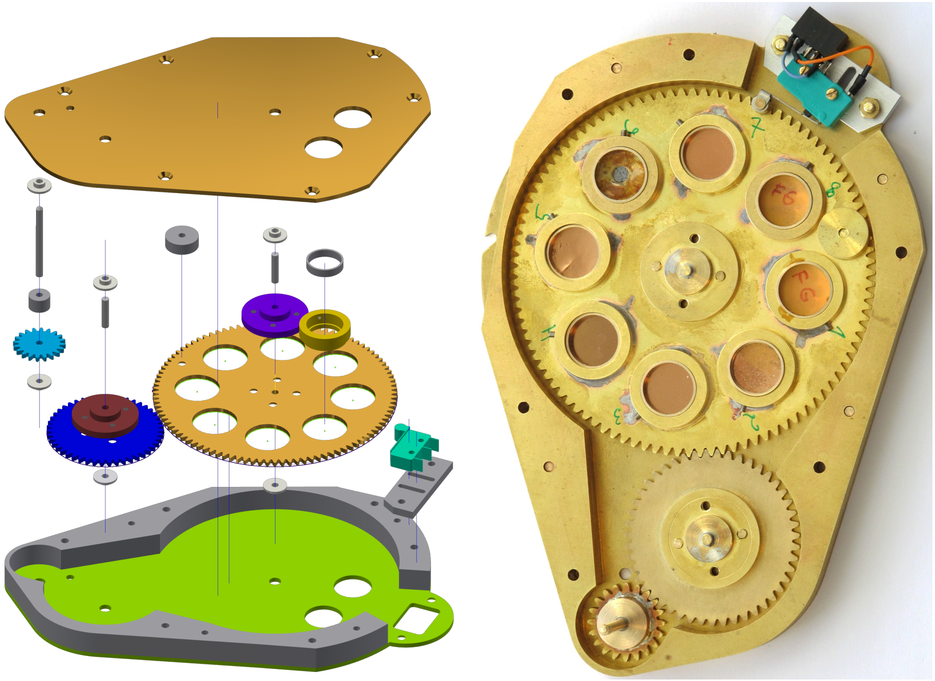

Figure 14: Exploded view of the filter wheel housing on the left without fasteners for clarity. Picture of the completed filter wheel housing without the top plate on the right.

Filter wheel gears, bottom, top and sides were laser cut from 2 mm non-magnetic L63 grade brass sheet. All openings were drilled over in the machine shop to get correct sizes and some openings were then threaded with a tap. Five identical pieces for the sides were pressed together with the bottom using dowel pins to form a solid body. Gears are held in the correct position by a copper shaft with a sliding bearing made out of polyether ether ketone (PEEK) with a 30% glass fiber filling. PEEK was selected for bearings because it's mechanical properties will not degrade with cooling and because it's thermal expansion parameter is similar to the surrounding brass. Ball bearings could not be used because they are susceptible to freezing inside the cryostat if they have any air inside while cooling.

Multi-mesh low pass filters from QMC were installed in addition to previously used Fluorogold and Kodak filters. All the used filters are described in Tab. 1 and the bolometer signal with the most used filters are shown in Fig. 15. QMC multi-mesh filters are layers of fine copper meshes pressed on dielectric spacers. These filters provide high in-band transmission efficiency and excellent out-of-band rejection [80]. Additionally, these filters cycle reliably between ambient and cryogenic temperatures for use inside the cryostat. Fluorogold is a glass-filled teflon, widely used as a low pass filter in the far IR region [79]. Kodak filter is made of layers of polyethylene pressed between pieces of Kodak 35 mm

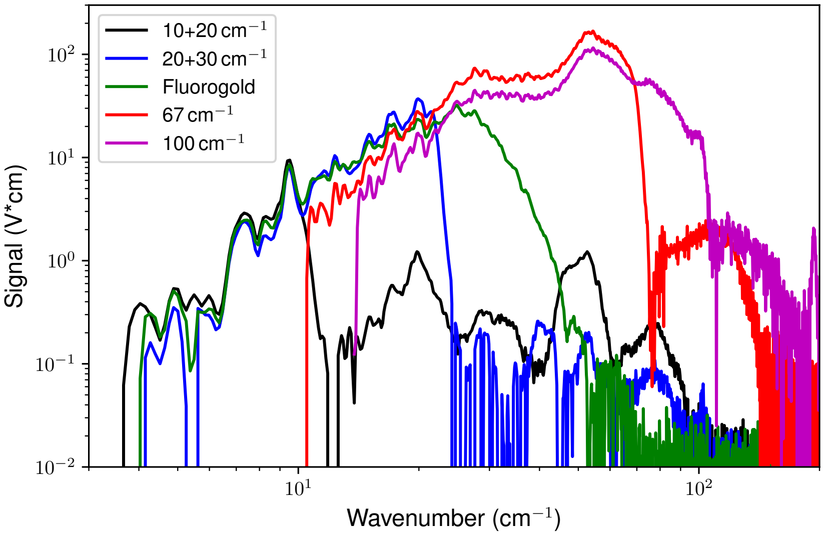

Figure 15: Bolometer signal of a 3 mm empty hole at 10 K measured with different filters. Spectra needs to be measured with several filters and combined later if the whole spectral range is needed.

film canister gray plastic cover.

Table 1: Filters and their low pass frequencies used in the filter wheel. Positions #1, #2 and #3 consist of two stacked filters.

Position	Filter	Low pass frequency	
		cm^{-1}	THz
#1	Fluorogold + Kodak	40	1.2
#2	QMC 10 + 20 cm^{-1}	10	0.3
#3	QMC 20 + 30 cm^{-1}	20	0.6
#4	QMC 67 cm^{-1}	67	2
#5	QMC 200 cm^{-1}	200	6
#6	Kodak ⌀4 mm	200	6
#7	QMC 100 cm^{-1}	100	3
#8	Fluorogold	40	1.2

2.5 Thermometry

The previously described probes need cryogenic thermometers for measuring the sample temperature during the experiments at low temperatures in high magnetic field. Cernox CX-1010-SD-HT thin film resistance temperature sensors were selected because of their small size, temperature range and low magneto-resistance. The calibrated sensor costs more than three times the price of an uncalibrated on. Therefore, one calibrated sensor and several uncalibrated sensors were ordered and a Cernox calibration probe was designed and built (Fig. 16).

Probe was designed to be inserted into a LHe transport Dewar with 18 mm clear access from the top. The design is centered on a stainless steel tube with an outside diameter of 18 mm acting as the main body of the probe. The top part is a brass housing for connectors to Lakeshore thermometer controllers and a Leybold flange for connecting the LHe pumping line to a turbo pump. The copper bottom part holds the connectors for thermometer wiring, thermometers and a stainless steel cover for mechanical protection.

Up to 8 temperature sensors can be mounted on the copper bottom part what ensures the thermometers are at the same temperature. The thermometer contacts were glued with varnish on the copper part to ensure additional thermal anchoring. The probe is cooled down to 1.5 K by pumping on LHe and then slowly warmed to room temperature. After that the probe is dismantled and the copper part holding the sensors and the protecting cover is put on a heat plate to warm the sensors up to 400 K. A calibration curve can then be calculated for all the sensors as the temperature of one of the sensors is accurately known.

Fitting procedure for the calibration curve was as following. Uncalibrated sensor resistance dependence on measured temperature was fitted with a third degree polynomial. Datapoints being further than 5% from the fitted polynomial were regarded as outliers and removed from further analysis (less than 0.5% of datapoints were removed). The cleaned dataset was fitted with a 10th degree polynomial that was used as a calibration curve for the uncalibrated sensor. These thermometers have found their place in several probes, including but not limited to rotating Voigt probe and high-temperature high-voltage Voigt probe.

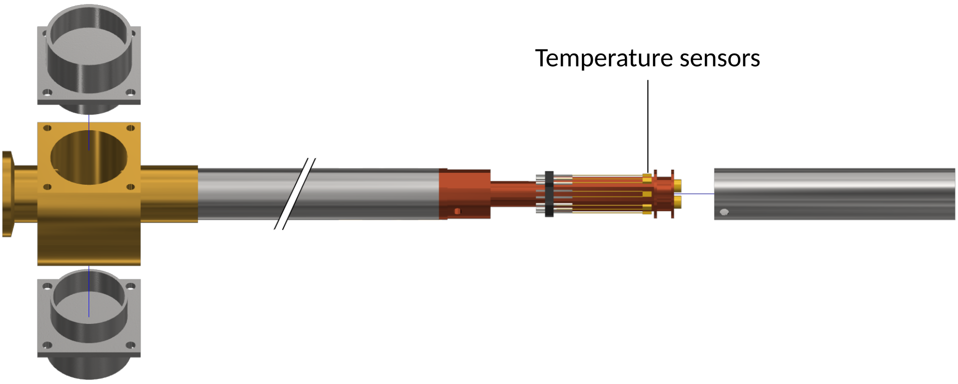

Figure 16: Temperature sensor calibration probe assembly drawing. Temperature sensors are the small golden pieces on the copper mounting part. Length of the probe has been reduced for easier viewing. The middle stainless steel ⌀18 mm pipe is 1300 mm long for the probe to reach the bottom of LHe Dewar.

2.6 Resistive Bitter Magnet Measurement System in Nijmegen

Measurements in magnetic fields between 17 T and 33 T were conducted in High Field Magnet Laboratory (HFML) in Nijmegen, Netherlands using a Michelson type interferometer Bruker IFS113V and resistive magnet in cell 3 (Fig. 17). A quasi-optical telescope was used to transport the radiation from the spectrometer down to the sample probe. A 1.6 K bolometer inside the probe was used as a detector. Spectral range of the system is from 12 cm to 700 cm. Magnetic fields up to 33 T were provided by a Bitter magnet with a bore size of ⌀32 mm. 18 MW of power is consumed for the maximum field of 33 T and 150 l/s of water is pumped through the magnet for cooling independent on the magnetic field. Noteworthy is that the cooling system alone consumes more than 15 MW of power.

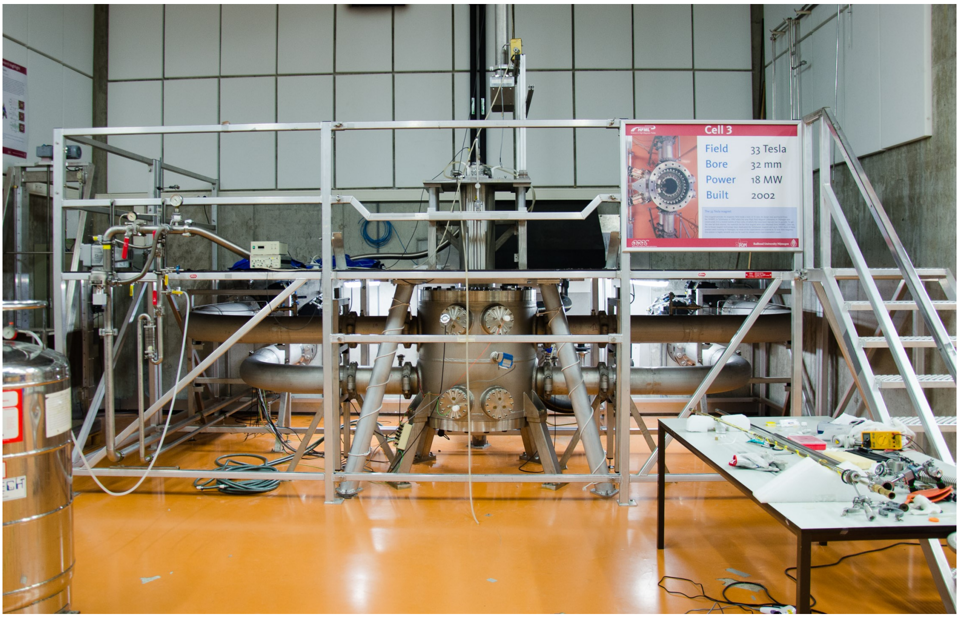

Figure 17: Nijmegen Cell 3 Bitter magnet setup. Bitter magnet housing is the wide upright cylinder in the center of the picture. Horizontal cooling water pipes are connected to both sides of the magnet housing. Liquid helium bath of the cryostat is visible above the magnet housing. Power cables are the black vertical cables on the back wall and the gray oversized lightpipe is to the right of the power cables.

3 Data Analysis

At the heart of any Fourier transform IR spectrometer is an interferometer (see section 2.1), which outputs an interferogram which can be seen in Fig. 18.a. It should be pointed out, that the Fourier transform of a single interferogram would yield a single beam spectrum, which is a plot of arbitrary infrared intensity versus wavenumber, encompassing the effects of the sample, measurement system and the light source. Therefore, there are several steps between the measurement of the interferogram and the final sample absorbance (or transmission) spectrum. This chapter gives a brief overview on what needs to be done to get this sample spectrum.

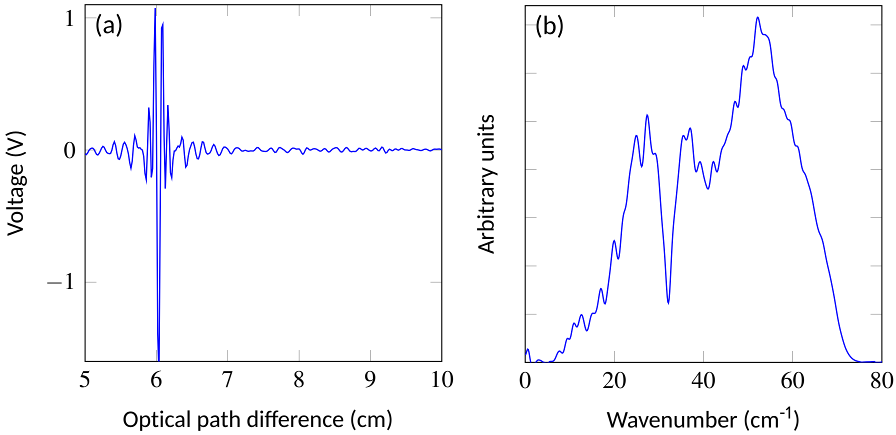

Figure 18: Example (a) interferogram and (b) resulting transmission spectrum of $Sr_2CoSi_2O_7$ crystal measurement with TeslaFIR spectrometer. This interferogram and spectrum characterize the whole measuring system, including the sample.

The measured interferogram is in space-domain. Fast Fourier transform (FFT) is used to turn this raw data into an actual spectrum (Fig. 18.b), which is still the spectrum of the whole measurement system. Usually we are not interested in the whole measuring system spectrum and only want to see the effects of magnetic field or temperature or some other parameter on the sample. In that case, we can divide the measured spectrum with a reference spectrum which can be the same measurement, except done at a different magnetic field or temperature or some other parameter - this is called a *transmittance* (Fig. 19.a):

$$t = \frac{I(B,T)}{I(B_{\text{ref}},T_{\text{ref}})}, \tag{37}$$

where t is transmission coefficient and I is transmitted THz light intensity as measured by the bolometer. Transmission is just the ratio between the measured intensity and some reference measurement. One can also calculate the *differential absorbance* (Fig. 19.b) as:

$$\alpha = -\frac{1}{d}\ln\frac{I(B,T)}{I(B_{\text{ref}},T_{\text{ref}})}, \tag{38}$$

where α is absorption coefficient and d is sample thickness. If one is interested in the actual sample spectrum, then one needs to measure the spectrum of an empty hole *(instrument response function)* in addition to the sample spectrum. Then the sample spectrum can be calculated with Eqs. (37) and (38) with the instrument response function as a reference. One could compare the absolute spectra measured at some different parameter, e.g. magnetic field (Fig. 20) or temperature. This is not usually done because the difference in the signal between two measurements has to be relatively strong to be easily distinguishable.

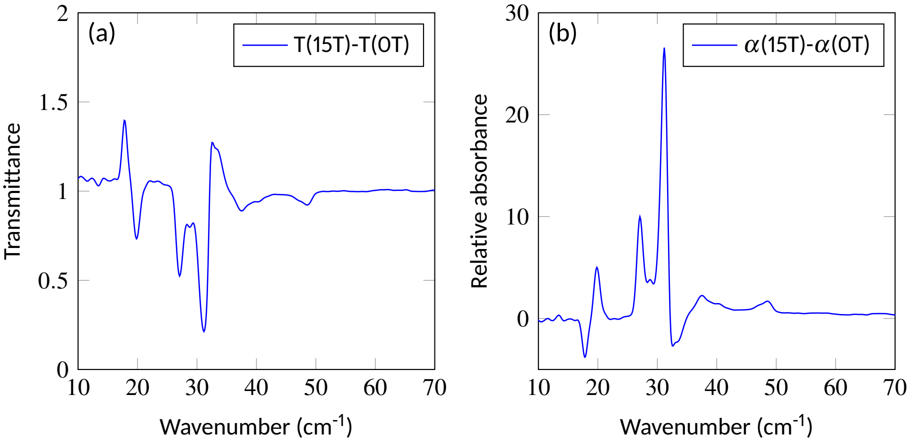

Figure 19: Relative (a) transmittance and (b) absorbance spectra as a ratio of 15 T and 0 T measurements. In case of transmittance, the reference spectrum peaks are pointing upwards and in case of absorbance, the reference spectrum peaks are pointing downwards.

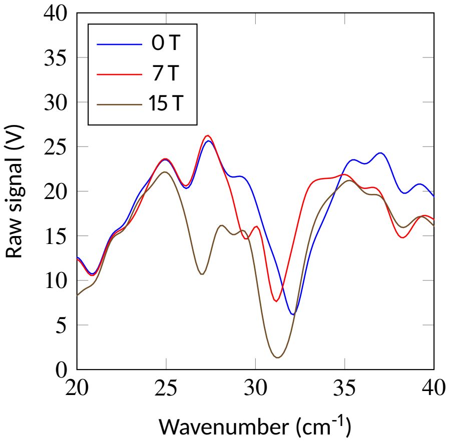

Figure 20: Spectra measured at 0 T, 7 T and 15 T with other parameters being the same. One can see a strong absorption around 30 wavenumbers in the 15 T spectrum compared to the 0 T and 7 T spectrum. Most of the time the difference is much harder to distinguish.

Our group is mostly using the differential absorbance, so we will focus on it from now on. Differential absorbance spectrum as calculated using Eq. (38) has components from both the chosen spectrum (peaks pointing up) and the reference (peaks pointing down) as can be seen in Fig. 19.b. The downward facing peaks can be removed by subtracting a baseline. We have three methods in use for calculating that baseline: minimum values, median of negative values or median of all values. All of these need several measured spectra to be effective. For minimum values, baseline consists of minimum values for each specific wavenumber from all of the spectra. Median of negative values method calculates the median of the negative values for each wavenumber whereas median of all values calculates the median of all the values for each wavenumber to get the reference spectrum. For the $Sr_2CoSi_2O_7$ measurement, minimum of all values gave the best baseline which is shown in Fig. 21. This calculated baseline is the calculated spectra for the reference measurement.

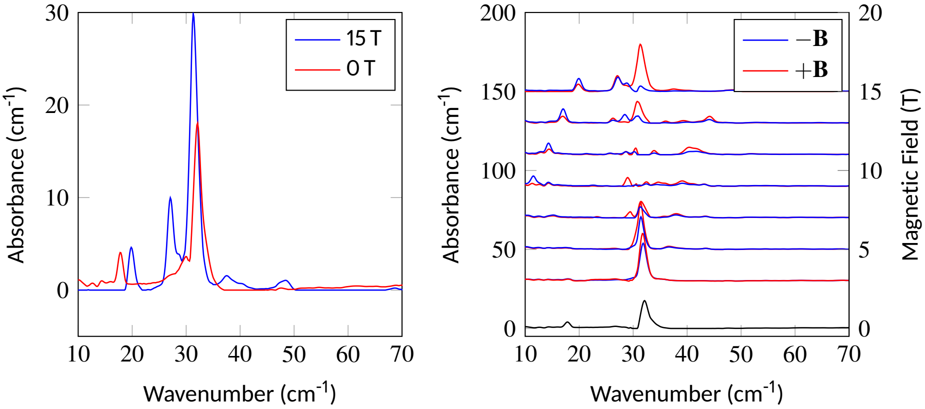

Figure 21: Resulting calculated absorbance a) spectra at 0 T and 15 T and b) stacked spectra from 0 T up to 15 T. Spectra measured at each magnetic field are shifted by a constant baseline relative to the magnetic field size.

Magnetic field affects the response function of the bolometer. If not taken into account, the resulting field ratios have a tilted baseline. To remove this effect, a linear fit of the spectrum is subtracted from it. Everything described in this section is done using RatioCalc software developed with LabVIEW in the group before the author of this thesis joined it. The spectra are saved from RatioCalc with all these corrections already applied. Further data processing is usually done using Python software described in section 3.2.

3.1 Fitting Software FitPeaks

A software with a graphical interface was developed as part of this thesis for fitting multiple peaks in several spectra. The software is written in Python with the help of different libraries, most notably NumPy [81] for fast numeric computation, Matplotlib [82] for the plotting and PyQT5 for the graphical user interface. The purpose of the software is to fit not too complex peaks in several spectra very quickly.

Starting the application opens the file selection box (Fig. 22) where desired spectra files can be selected or dragged into the window. The software tries to find the parameter differentiating the files and that value is shown in the parameter column. User can change the decimal separator and delimiter symbols used in the file names. Our lab convention is to use the unit of the parameter as the decimal separator and separate different parameters by an underscore as seen in Fig. 22. Pressing *'FIT'* button opens the fitting window.

The fitting window (Fig. 23) consists of the plot showing spectra and peaks in the middle, buttons for navigating the plot on the top, buttons and sliders allowing to configure the fitting procedure on the bottom. The first step (but not required) is usually selecting the *x* axis limits. This changes the plot start and end positions for the *x* axis, which are also used as the limits for the fitting function. This is needed as the start and end of the spectra are usually very noisy due to low signal. Preliminary peak positions are found by

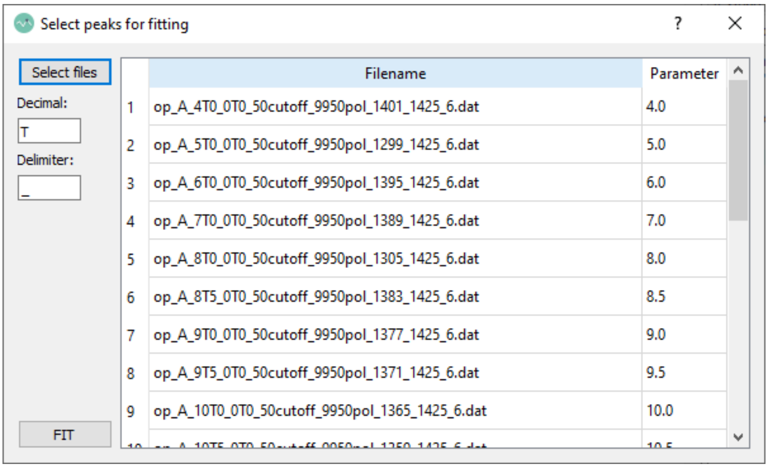

Decimal: T

Delimiter: _

	Filename	Parameter
1	op_A_4T0_0T0_50cutoff_9950pol_1401_1425_6.dat	4.0
2	op_A_5T0_0T0_50cutoff_9950pol_1299_1425_6.dat	5.0
3	op_A_6T0_0T0_50cutoff_9950pol_1395_1425_6.dat	6.0
4	op_A_7T0_0T0_50cutoff_9950pol_1389_1425_6.dat	7.0
5	op_A_8T0_0T0_50cutoff_9950pol_1305_1425_6.dat	8.0
6	op_A_8T5_0T0_50cutoff_9950pol_1383_1425_6.dat	8.5
7	op_A_9T0_0T0_50cutoff_9950pol_1377_1425_6.dat	9.0
8	op_A_9T5_0T0_50cutoff_9950pol_1371_1425_6.dat	9.5
9	op_A_10T0_0T0_50cutoff_9950pol_1365_1425_6.dat	10.0

Figure 22: FitPeaks file selection box. Software detects the the parameter that differentiates the files. In this case, the files are part of field dependence measurements and the resulting parameter is the external magnetic field.

pressing *'Find peaks'* button. The user can now add or remove peaks with the left or right button of the mouse, respectively or use the 'threshold' and 'minimum distance' sliders for fine-tuning the automatic peak finding. *'Add peak'* button on the top toolbar activates more controlled peak adding method – by clicking on the desired peak position and dragging in the horizontal and vertical axis allows the user to define the initial width and height of the Gaussian as the initial values for the fit function. Number of peaks to be fitted per spectra is not limited. If needed, the baseline can be subtracted using the Asymmetric Least Squares (ALS) smoothing [83]. Pressing *'Fit peaks'* starts the fitting procedure with the spectra and the preliminary peak positions as the input parameters. Trust Region Reflective algorithm [84] is used to fit the Gaussians to the spectra as it is optimized for a bound-constrained minimization problems. Peaks are fitted with the FWHM version of the Gaussian peak function:

$$y = A\exp\left(\frac{-4\ln(2)(x-x_c)^2}{w^2}\right), \tag{39}$$

where A is the area, x_c is the center of the peak, w is the full width at half maximum (FWHM). These three values are the results of the fit and they can be visualized (Fig. 24) by pressing the *'Show fit plot'* button. Other fitting functions than Gaussian are easy to implement if needed. *'Save fit results'* exports the fit results in a CSV formatted file for further processing or analyzing.

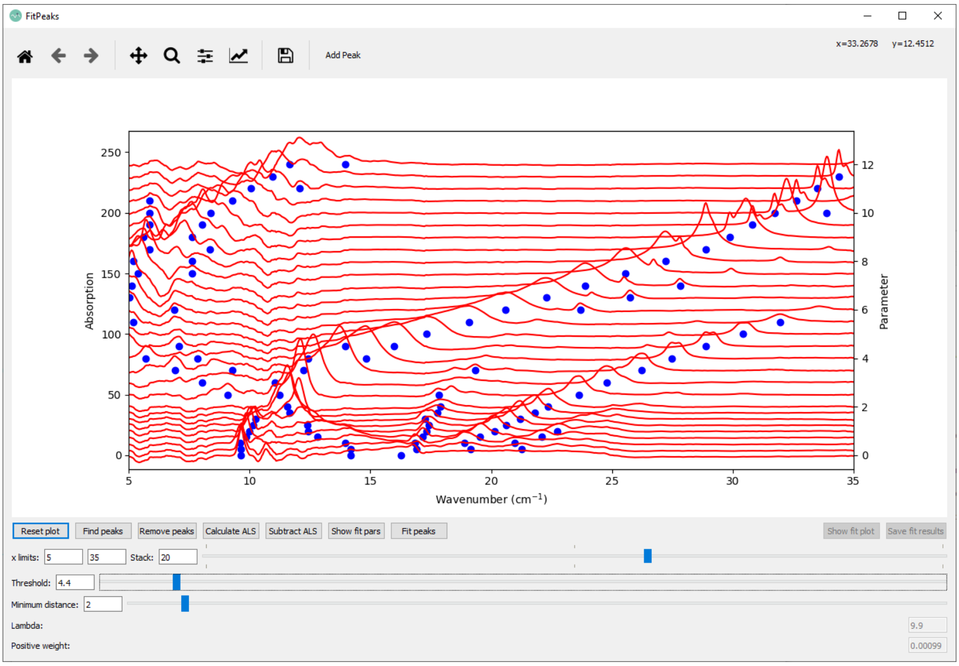
FitPeaks
Add Peak
Absorption
Parameter
Wavenumber (cm^{-1})
0
50
100
150
200
250
0
2
4
6
8
10
12
5
10
15
20
25
30
35
Reset plot
Find peaks
Remove peaks
Calculate ALS
Subtract ALS
Show fit pars
Fit peaks
Show fit plot
Save fit results

x=33.2678 y=12.4512

x limits: 5 35 Stack: 20

Threshold: 4.4

Minimum distance: 2

Lambda: 9.9

Positive weight: 0.00099

Figure 23: FitPeaks fitting window. Red lines are stacked spectra, blue dots are starting peak positions for the input of the fitting function.

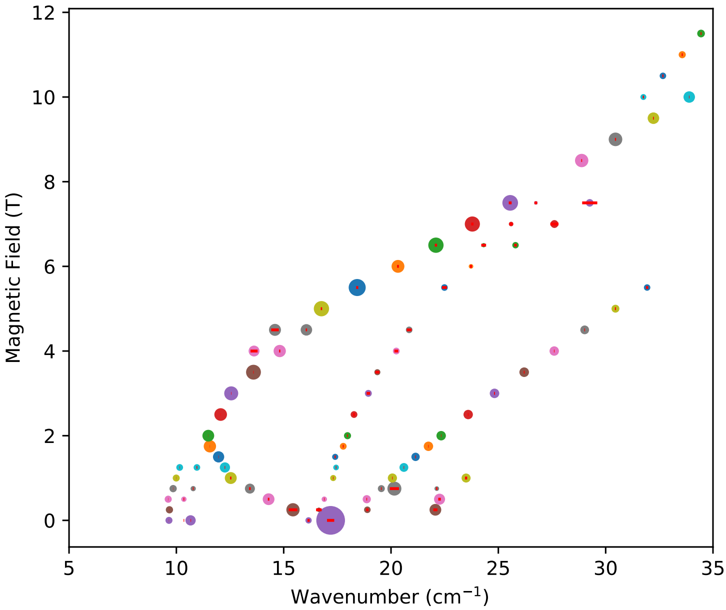

Figure 24: FitPeaks fit results visualized. Size of the rings corresponds to the area of the peak, red lines are the peak center error bars. Color of the bubbles is arbitrary. This figure gives a good overview how the excitations change their position and line area.

3.2 BdepTools - Python Library for Preparing Figures for Publishing

Until recently, figures of the measured data for publishing in scientific journals were done in a commercial software Origin Pro. The issue with this kind of software is that the final figure made in Origin Pro is only loosely coupled to the spectra files calculate with the RatioCalc. For example, if spectra are recalculated, then sometimes the figures have to be prepared again from start. Additionally, similar figures formats are needed very often. A Python library called BdepTools was developed to solve this problem. Running the BdepTools library on a new set of spectra gives a nice figure reasonably quickly saving a lot of time. The plotting part is done mostly automatically, the user just has to insert the measurement data (e.g. sample name and magnetic field and polarization directions). When doing all the calculations on the spectra and producing the final publishable figure in one Python code, then changes in any of the steps are recorded in the Pyhton code. The code is stored along with the figure.

Existing libraries were used to speed up the development time. Most notably, NumPy [81] library was used for fast numeric computation on array objects and Matplotlib [82] was used for producing the publication quality figures. Unit tests are included to reduce the chance of introducing errors in the codebase. The library is designed to be flexible, allowing to do different figures. Most commonly used cases are the stacked spectra and intensity map plots. For example, Fig. 30 was done with the BdepTools library. There were a number of revisions until the figure was published and the BdepTools library saved countless hours of mundane work. Almost all the figures showing spectra, made by our research group in the last few years, have been done using this library.

4 Results and Discussion

4.1 $CaBaCo_4O_7$

The pyroelectric ferrimagnet $CaBaCo_4O_7$ is a type-I multiferroic compound with the largest magnetic-order induced ferroelectric polarization ($\Delta P = 17\ mC/m^2$) reported, so far [85]. $CaBaCo_4O_7$ belongs to a *swedenborgite* family [86] having members with multiferroic phases close to room temperature [87]. $CaBaCo_4O_7$ and $CaBaFe_4O_7$ are the only members of the *swedenborgite* family with long-range magnetic order allowing the investigation of the dynamic magnetoelectric effect through spin-wave excitations. At room temperature $CaBaCo_4O_7$ has an orthorhombic, noncentrosymmetric crystal structure with a $Pbn2_1$ space group with alternating triangular and Kagome layers along *c*. These sublattices with the strong antiferromagnetic exchange coupling between the cobalt ions are textbook examples of geometrical frustrated systems. In $CaBaCo_4O_7$ an orthorhombic distortion releases the frustration, and a ferrimagnetic order develops below T_C=70 K [88, 89]. The magnetic state of $CaBaCo_4O_7$ can be described as a triangular array of ferrimagnetically aligned bitetrahedral *c*-axis chains with a net moment along *b*, Fig. 25. Competing interactions within each chain produce a noncollinear spin state. The strong electric polarization of $CaBaCo_4O_7$ below T_C is induced by the exchange striction mechanism – displacement of oxygen atoms surrounding the bonds that couple those chains [62].

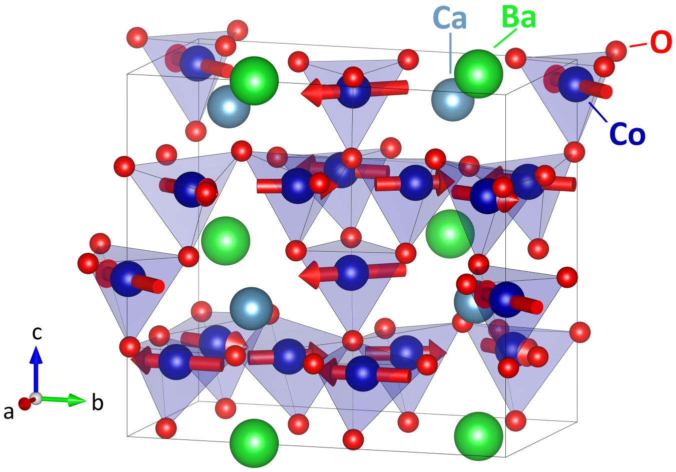

Figure 25: $CaBaCo_4O_7$ crystal structure where the CoO_4 tetrahedra are three-dimensionally interconnected and form a geometrically frustrated network. Each unit cell contains 16 Co ions on two Kagome and two triangular layers.

Optical measurements were performed in our lab in NICPB previously [90] in both Faraday and Voigt geometry showing the magnetic resonances and their selection rules in $CaBaCo_4O_7$. Single crystals were characterized at room temperature with XRD and polarized optical microscopy which revealed that orthorhombic twinning occurs in the sample on a microscopic scale. Voigt geometry results for one polarization are shown in Fig. 26. The lowest-energy mode at 36 cm^{-1} (1.07 THz) is a mixed magnetic and electric dipole resonance and splits asymmetrically, almost linearly with increasing field with slopes of $\sim$0.45 cm^{-1}/T and $\sim$0.96 cm^{-1}/T, respectively. The higher energy mode at 47 cm^{-1} (1.41 THz) can be excited only by the electric-field component of the light and is shifted in proportion to the field with $\sim$0.46 cm^{-1}/T ratio. The hypothesis is that the two lines starting from 36 cm^{-1} are from two different domains. If they are from two different domains

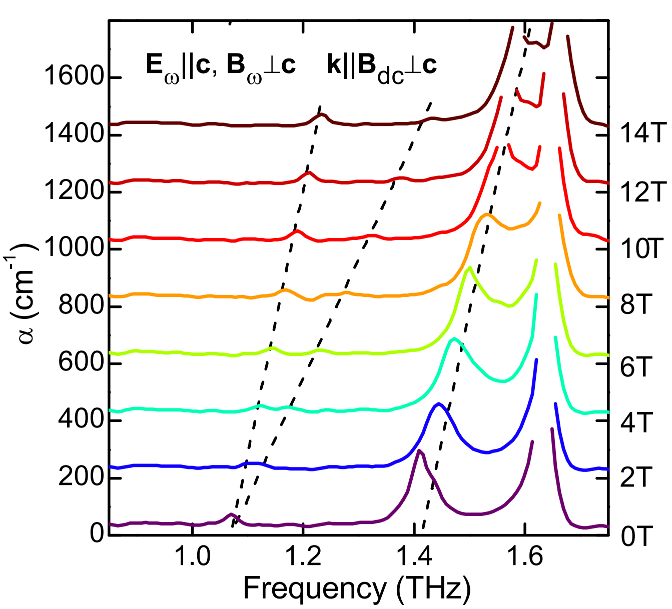

Figure 26: Magnetic field dependence of absorption spectra of $CaBaCo_4O_7$ at 4 K. Dashed lines show the evolution of the resonance frequencies in field. The vertical offset of spectra is proportional to the magnetic field. Lower frequency absorption at 36 cm^{-1} (1.07 THz) splits in magnetic field whereas the higher energy mode at 47 cm^{-1} (1.41 THz) is not split. Figure reproduced from [90].

they should change their position when magnetic field changes its direction within the *ab* plane. Verifying this was the aim of this work.

The THz spectra of the same $CaBaCo_4O_7$ sample as described previously were measured with TeslaFIR measuring system using the rotating Voigt probe (see section 2.3.1). In addition to general magnetic field dependence measurements, the sample was rotated 10° between each measurement in fixed 15 T magnetic field – the sample was rotated about **c**=[0,0,1] while the magnetic field was fixed in the laboratory reference frame. Median of all the negative absorption values of the resulting spectra were used as a baseline and added to all the spectra. The resulting plot is seen in Fig. 27. Points of interest are the peaks between 33 and 50 cm^{-1} that change it's position for different sample rotations. The locations of these peaks were fitted and the resulting peak positions can be seen in Fig. 28. The threefold splitting of the spin-wave frequencies shows that the sample is hexagonally twinned with a common **c**=**z**=[0,0,1] axis. Each of the three hexagonal domains contributes one branch with a period of π. Together with additional measurement techniques it was revealed that the complex spin order in the domains can be characterized as a triangular array of bi-tetrahedral *c*-axis chains that are ferrimagnetically coupled to each other in the *ab* plane.

Previous magnetization measurements on $CaBaCo_4O_7$ [88, 89, 91–93] are rather scattered, probably due to excess or deficient oxygen [94]. Therefore, new magnetization measurements were performed at 4 K, results can be seen in Ref. I Fig. 3. All three magnetizations in **a**, **b** and **c** directions increase monotonically at least up to 32 T magnetic field. In domain I, **a** lies along the laboratory direction **x**=[1,0,0] and **b** lies along **y**=[0,1,0], in domain II, **a**=[-1/2,$\sqrt{3}$/2,0] and **b**=[-$\sqrt{3}$/2,-1/2,0], and in domain III, **a**=[-1/2,-$\sqrt{3}$/2,0] and **b**=[$\sqrt{3}$/2,-1/2,0]. If p_l are the domain populations, then the magnetizations M_x and M_y measured with fields along **x** and **y** only depend on p_1 and p_2+p_3=1-p_1. Of course, M_z

measured with field along **z** is independent of p_l.

The optical absorption of any mode in domain l is proportional to p_l. So at nonzero field, the lower frequency absorption is proportional to p_2+p_3 whereas the higher frequency absorption is proportional to p_1. At zero field, all domains have the same mode spectrum so that both the lower and higher energy mode absorptions are proportional to $p_1+p_2+p_3=1$. Comparison between the theoretical and experimental results suggests that roughly 20% of the sample is in domain I with the **a** axis along [1,0,0] and that 80% of the sample is in one of the two other domains. Different domain populations or even orthorhombic twinning in other samples may explain the discrepancies between the reported magnetization measurements.

From the optical measurements and magnetization data R. Fishman produced a spin model theory as well as fitted exchange and anisotropy parameters. Further analysis of the spin model can be found in Ref. I on p. 72.

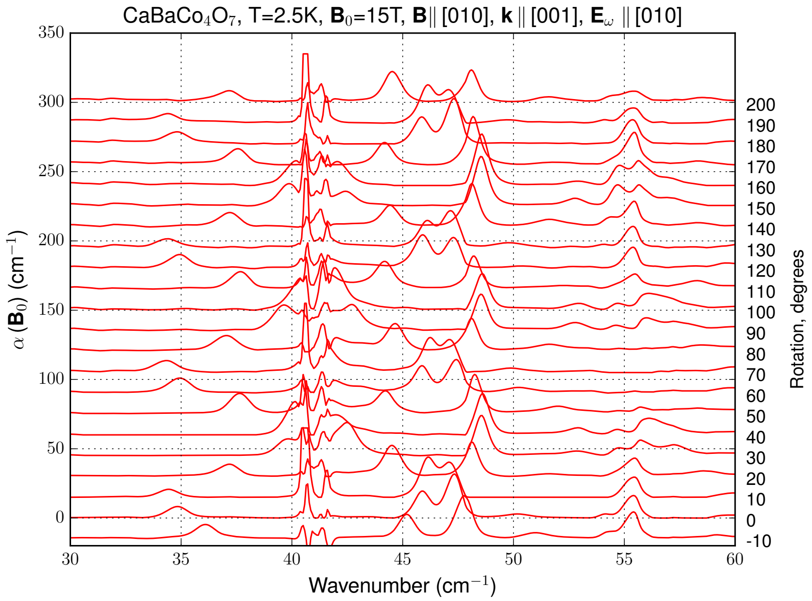

Figure 27: Spectra as a function of angle between the magnetic field direction and crystal [0$\bar{1}$0] axis at 2.5 K. Polarizer was fixed in the lab frame at $\mathbf{E}_\omega \| \mathbf{B}$. Sharp lines between 40 and 42 cm^{-1} are noise because of a saturated absorption due to a strong phonon.

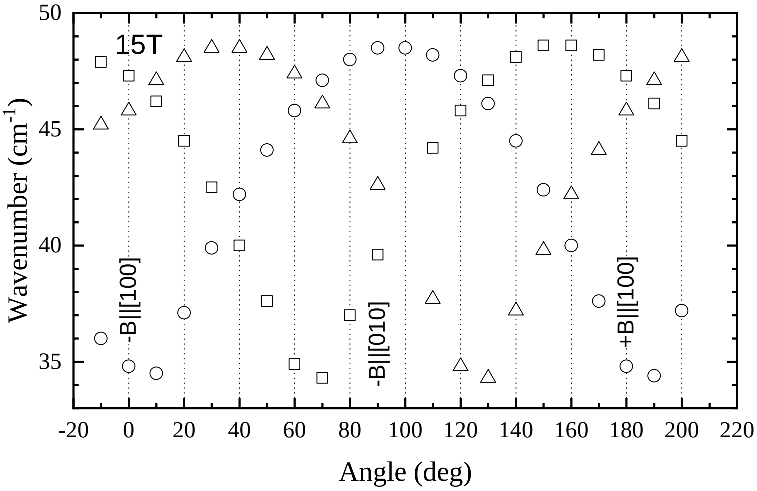

Figure 28: $CaBaCo_4O_7$ line positions as a function of angle between $\mathbf{B}$=15 T and crystal [100] axis at 2.5 K. Each hexagonal domain contributes one branch (shown using different symbols) with a period of π. Cusps in the mode frequencies for each domain are caused by flipping the b *component of the magnetization.*

4.2 $Sr_2CoSi_2O_7$

Melilite $Sr_2CoSi_2O_7$ is a type-II multiferroic with an åkermanite structure and $P\bar{4}2_1m$ space group. Schematic crystal structure is shown in Fig. 29. Co^{2+} spins S=3/2 have an easy plane anisotropy in the (001) plane with a hard axis in the *c* direction. $Sr_2CoSi_2O_7$ crystals develop staggered easy-plane antiferromagnetic order below the Néel temperature T_N=7 K [71]. The crystal structure of melilites lacks the inversion symmetry. Applying magnetic field, the time-reversal symmetry will be broken in the paramagnetic phase and the necessary conditions for NDD are then fulfilled. Akaki et al. [39,69] demonstrated that the static ME effect persists in the paramagnetic regime, see Fig. 3, where the field-induced polarization scales with the square of the magnetization. Since the static ME susceptibility is related to NDD by the ME sum rule [45], we expect that NDD appears also in the paramagnetic phase of $Sr_2CoSi_2O_7$.

The $Sr_2CoSi_2O_7$ crystals were grown by a floating-zone method and characterized by V. Kocsis in RIKEN, Japan. $SrCO_3$, Co_3O_4 and de-hydrated SiO_2 were mixed in stoichiometric amount and sintered for 120 hours at 1200 °C in air with one intermediate re-grinding. The resulting product was pressed into a rod shape and re-sintered for 60 hours. The polycrystalline rod was melted into a single crystal ingot in a halogen-incandescent lamp floating zone apparatus. Samples cut from the ingot were disk-shaped with a diameter of 4 mm and thicknesses of d=0.2 and 0.5 mm in the [100] direction. The orientation of the crystallographic axes of the single crystal ingots was identified by means of X-ray back-reflection Laue technique.

THz absorption spectra were measured in NICPB in Tallinn (up to 17 T) using the TeslaFIR setup and in HFML in Nijmegen, Netherlands (up to 33 T) using far-infrared setup described in section 2.6. Magnetic field was applied in [100] direction which induces magnetization parallel the field. The point group in the paramagnetic state is then reduced to the magnetic point group 22'2' [95]. Measurements were performed in Faraday geometry, i.e. $\mathbf{k} \,||\, \mathbf{B}$. The absorption spectra were determined for two polarizations of THz radiation,

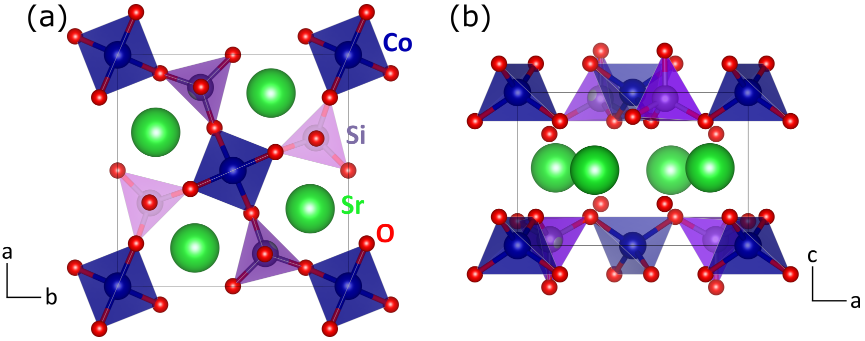

Figure 29: Schematic crystal structure of $Sr_2CoSi_2O_7$ along (a) c *axis and (b)* b *axis. CoO_4 and SiO_4 tetrahedra are connected at their corners forming two-dimensional layers stacked along* c *axis with Sr atoms between the layers. The two inequivalent CoO_4 tetrahedra are located at (0, 0, 0) and (0.5, 0.5, 0.5) and connected by a SiO_4 tetrahedron.*

$\mathbf{E}_\omega \parallel$ [010] and $\mathbf{E}_\omega \parallel$ [001]. In this chiral symmetry state of the crystal our experiments show that the spectra measured in positive and negative fields are markedly different as can be seen in Fig. 30. The DD was detected by changing the direction of the magnetic field from $+$B to $-$B, i.e., from $\mathbf{B} \uparrow\uparrow \mathbf{k}$ to $\mathbf{B} \uparrow\downarrow \mathbf{k}$. Due to the twofold rotation symmetry about the [001] axis, the reversal of $\mathbf{B}$ is equivalent to the reversal of $\mathbf{k}$ [8].

Temperature dependence of absorption spectra in magnetic fields $\pm$14 T in two polarizations is shown in Fig 30. Below 7 K, in the magnetically ordered phase, the spectrum is dominated by three resonances at 18, 28, and 32 cm^{-1}. Since the resonance frequencies of the spin-wave modes are located at almost the same position in $Sr_2CoSi_2O_7$ and $Ba_2CoGe_2O_7$ [41], and the magnetic field dependence of $\mathbf{M}$ and $\mathbf{P}$ is also similar in the two compounds [39, 68], we use the same assignment of spin waves as for $Ba_2CoGe_2O_7$ [96]. The 18 cm^{-1} mode is the Goldstone mode of the easy-plane antiferromagnet gapped by the in-plane magnetic field whereas the latter two resonances correspond to the spin-stretching modes. When the field is parallel or antiparallel to the light propagation direction, the spectra are markedly different. The absorption difference is due to the MChD [41, 95].

As the temperature increases, the spin-stretching modes at 28 and 32 cm^{-1} merge and eventually disappear above 30 K. However, the lowest-energy mode, the Goldstone mode in the ordered phase, is visible even at 100 K. The MChD has pronounced polarization dependence in the paramagnetic phase. A strong MChD is observed for all resonances in polarization $\mathbf{E}_\omega \parallel$ [010] – the absorption coefficient is nearly zero for positive fields whereas finite absorption is detected for negative fields. In the orthogonal polarization $\mathbf{E}_\omega \parallel$ [001], the lowest-energy resonance has weak MChD and changes sign between 10 and 15 K.

Additionally, magnetic field dependencies at 10 K and 30 K were measured in magnetic fields up to 16 T and 30 T, respectively (see Ref. II on p. 82). At 30 K the average intensity of the single resonance line $(\alpha^+ + \alpha^-)/2$ is nearly the same for both polarizations and it grows gradually as the field is increased. For polarization $\mathbf{E}_\omega \parallel$ [010] a strong NDD is observed while only a small absorption difference is detected in $\mathbf{E}_\omega \parallel$ [001].

We have shown that $Sr_2CoSi_2O_7$ exhibits NDD even at 100 K, way above it's magnetic ordering temperature. Furthermore, the experimental data goes well with the exact diagonalization of a four-spin cluster. Further analysis and figures about this work can be found in Ref. II on p. 82.

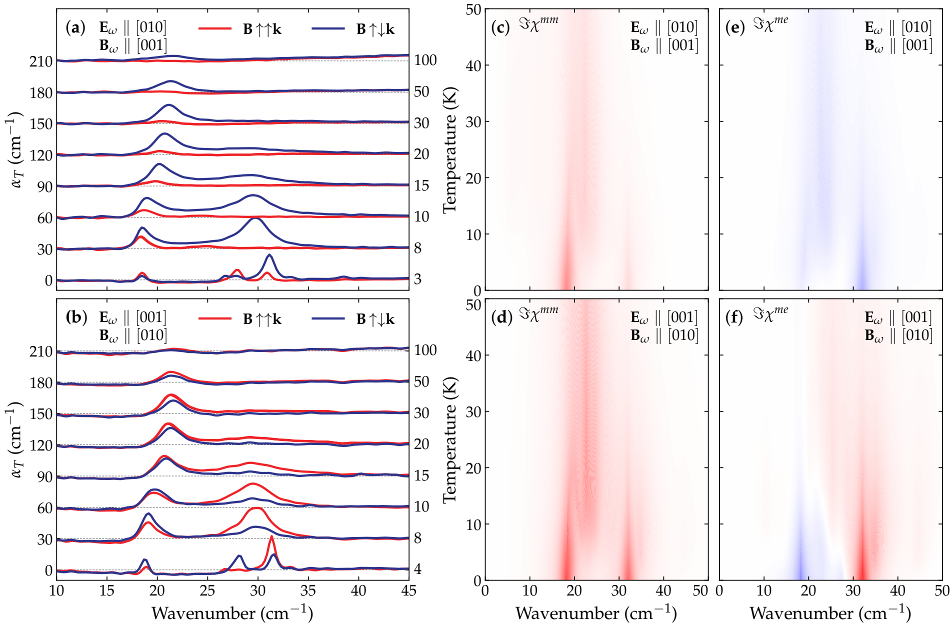

Figure 30: Temperature dependence of (a), (b) measured THz absorption spectra and (c)-(f) calculated susceptibilities of $Sr_2CoSi_2O_7$ *at* ± 14 *T. Applied magnetic field was* $\mathbf{B} \uparrow\uparrow \mathbf{k} \parallel [100]$ *for the red line and* $\mathbf{B} \uparrow\downarrow \mathbf{k}$ *for the blue line. Spectra measured at different temperatures are shifted by a constant baseline. (c), (d) are Imaginary parts of magnetic susceptibility* $\Im\chi^{\mathrm{mm}}(\omega)$ *and (e), (f) are imaginary part of time-reversal odd ME susceptibility* $\Im\chi^{\mathrm{me}}(\omega)$ *(Eq. 16) plots. Red and blue colors corresponds to the sign of susceptibility, positive or negative, respectively. The saturation of the color corresponds to the magnitude of the corresponding susceptibility matrix elements. The susceptibilities were calculated by the exact diagonalization of a four-site cluster. Figure reproduced from Ref. II*

4.3 LiCoPO$_4$

The lithium orthophosphate family (space group *Pnma*), Li*M*PO$_4$ (*M* = Co, Ni, Mn, Fe), is in many ways an excellent model system for studying the ME effect. All family members exhibit the ME effect in their low-temperature and low-field ground state. Here we will focus on LiCoPO$_4$, which has by far the strongest ME effect in the lithium orthophosphate family [97].

There are four formula units per unit cell [98], Fig. 31. While a local electric polarization is allowed at each Co site due to its low site symmetry, the total polarization of the unit cell vanishes [10]. Below the Néel temperature (T_N=21.8 K) the S=3/2 spins of Co^{2+} ions form a collinear magnetic order while preserving the unit cell [99]. Therefore, the magnetic structure can be described as four magnetic sublattices. The magnetic Co-O-Co superexchange interactions couple the spins within (100) planes while only the long range interactions such as the Co-O-P-O-Co provide the inter-layer coupling [98]. Since the AFM state simultaneously breaks the spatial inversion and time reversal symmetries, the material exhibits a linear ME effect with finite ME susceptibility [97].

Two possible AFM domains of LiCoPO$_4$, labeled α and β (Fig. 31) are characterized by ME couplings of opposite signs [97, 100]. These domains can be transformed into each other by either the spatial inversion or the time reversal. By simultaneously applying crossed $\mathbf{E}$ electric and $\mathbf{B}$ magnetic fields in the *xy* plane during the cooling process through

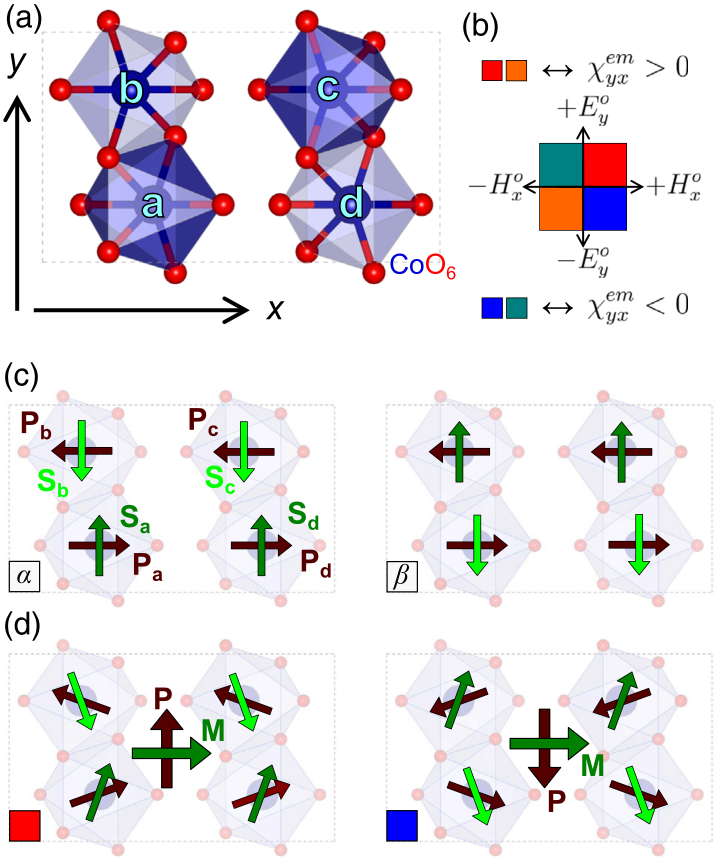

Figure 31: *(a) Unit cell of $LiCoPO_4$ viewed from the z axis, Li and P sites are omitted for clarity. There are four Co sites (a-d) in the unit cell surrounded by O octahedra. (b) The four combinations of the poling fields are presented in four colors. (c) The two AFM domains in $LiCoPO_4$. Magnetic sublattices (green and olive arrows) are interchanged in the AFM domains α and β whereas the AFE polarization pattern (brown arrows) is the same. (c) Domains α and β can be selected by the poling fields (red and blue). Figure reproduced from [10].*

T_N a single domain state, α or β, is established in the whole sample [10]. At low temperatures that state is preserved even after the removal of these poling fields. The other ME domain can be selected by the reversal of one of the poling fields.

When light propagates in the crystal, the oscillating magnetizations in both the α and β domains fluctuate in phase with $\mathbf{B}_\omega$ whereas the magnetically induced polarizations oscillate in antiphase with respect to each other. Therefore, the index of refraction for light traveling along the *z* axis is different for the α and β domains [101]. The directional dichroism along *z* must then also have opposite signs for these two domains as the reversal of the light propagation direction is equivalent to the exchange of the ME domains. In materials with an antisymmetric ME effect ($\chi_{xy} = -\chi_{yx}$) the differences in the refractive indices of the two AFM domains are the same for the two orthogonal light polarizations. Alternatively, if the susceptibility tensor is symmetric ($\chi_{xy} = \chi_{yx}$) then the differences in the refractive indices of the two domains changes sign upon the rotation of light polarization by 90°.

The $LiCoPO_4$ crystals were grown by a floating-zone method by V. Kocsis in RIKEN [10].

For information concerning the crystal growth, space group and symmetry of the sample crystal see SM of Ref. [10]. Optical absorption spectra (Fig. 32) were measured in NICPB using the high-temperature high-voltage Voigt probe described in section 2.3.2. At high temperature (30 K) crossed $\mathbf{E}$ and $\mathbf{B}$ poling fields were applied to the sample along the *y* and *x* axis, respectively, followed by cooling the sample through T_{N} to form a single ME domain state. After this ME poling procedure, the poling fields were switched off. Instead of exchanging the light source and the detector, which would correspond to the reversal of the light propagation direction, experiments with different magnetoelectric poling conditions were compared. The directional optical anisotropy was determined as the difference of the absorption spectra measured after poling the material with opposite signs of the $\mathbf{E}\times\mathbf{B}$ product. Measurements have been repeated for all four possible combinations of the crossed poling fields: $\pm\mathbf{E}\times\pm\mathbf{B}$ and $\mp\mathbf{E}\times\pm\mathbf{B}$. The relative absorption spectra were calculated by subtracting the reference spectrum measured at T=30 K in the paramagnetic phase. Therefore, the low-temperature spectral features are related to excitations emerging in the magnetically ordered state. The poling-field-dependent resonances are ME resonances since the ME response has opposite signs in the α and β domains.

Fig. 32(e) - (h) show the absorption spectra of the magnetic excitations at T=5 K for four different poling configurations. Modes #3, #6, #11-13 show remarkable absorption difference following different poling procedures. As the magnitude of the absorption difference for the ME domains is the highest for resonance #3, in the following we will focus on this mode. The mode only appears for light polarization $\mathbf{E}_\omega \parallel y$, $\mathbf{B}_\omega \parallel x$. Mode #3 has high absorption in Fig. 32 (e) following poling with opposite sign fields, $\pm\mathbf{E}$, $\mp\mathbf{B}$, while its absorption is drastically reduced after poling with same sign fields $\pm\mathbf{E}$, $\pm\mathbf{B}$. When the poling fields are rotated 90° (Fig. 32 (f)), the high and low absorption states of the excitation are interchanged. It means that rotation of the poling fields by 90° results in the selection of the other ME domain. As discussed before, the selection of different ME domains by a 90° rotation of the poling fields implies that the symmetric part of the ME tensor dominates over the antisymmetric part. Since neither component of the ME susceptibility changes sign below T_{N}, we concluded that the symmetric part dominates the low-temperature ME tensor.

Furthermore, selection rules were determined by measuring the absorption spectra with light polarized in all principle directions. In total, 13 resonances were observed, one more than expected from the multiboson spin-wave theory of a four-sublattice AFM with S=3/2 spins [10]. Since the structural symmetry is preserved, no new phonon modes are expected in the magnetically ordered phase; thus, the origin of the extra mode is unclear.

According to the sum rule, excitations with ME character contribute to the static ME effect with Eq. 27. In case the absorption lines are well separated, it is possible to estimate the weight of each excitation to the static ME effect by limiting the integration around the excitation (Fig. 5 in Ref. III). Alternatively, without limiting the integration window, total ME susceptibility can be obtained (Fig. 6 in Ref. III). The results of the zero-field static ME susceptibility obtained from magnetocurrent measurements and the sum of the contributions of the studied optical modes were compared. In case of χ_{yx}/c, the value obtained via the ME spectroscopy was +20.5 ps/m whereas the absolute static value from magnetocurrent measurements was 32 ps/m - the observed ME resonances explain well the bulk of the static ME response. On the other hand, χ_{xy}/c deduced from the optical measurements (-3.1 ps/m) is much smaller than the absolute ME susceptibility (15 ps/m) measured in the static limit. Most likely there are additional ME modes or ME electronic excitations outside the limited frequency range of the THz measurement.

Further analysis and figures about this work can be found in Ref. III on p. 98.

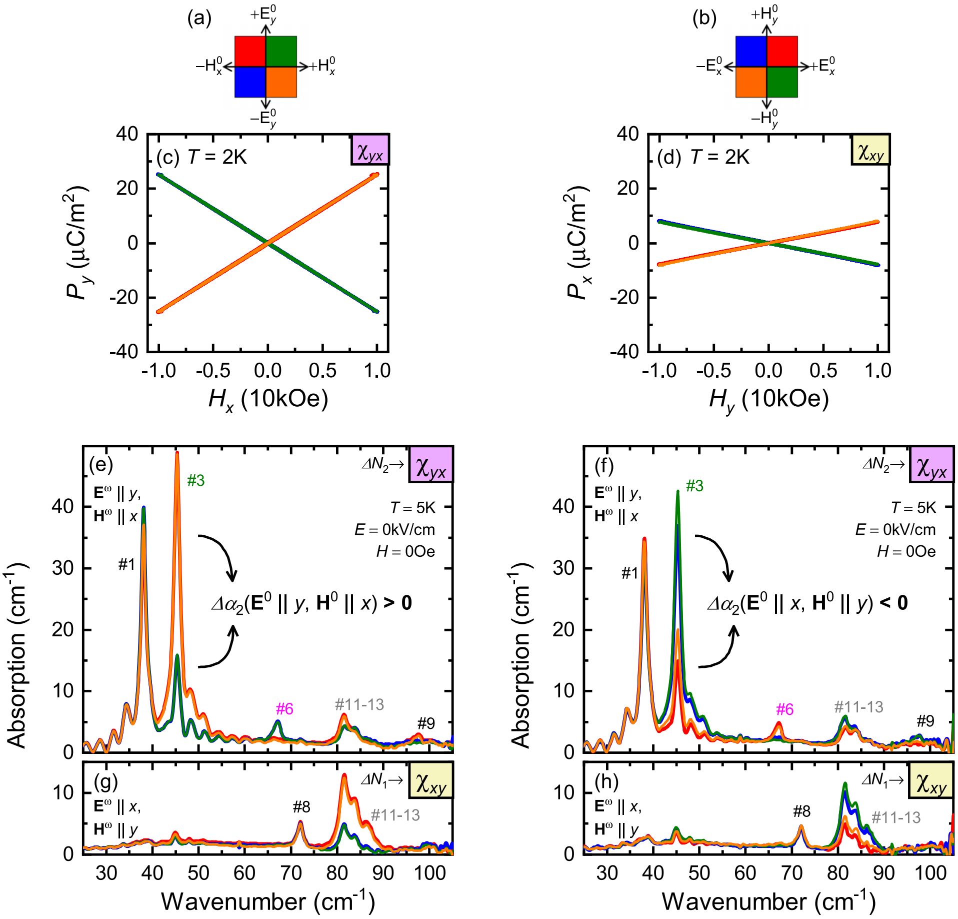

Figure 32: Remnant static and dynamic ME effects in $LiCoPO_4$. (a) and (b) Experimental configuration of the $\mathbf{B}$ and $\mathbf{E}$ poling fields. The color code of (b) corresponds to the simultaneous 90° rotation of the fields of (a). (c) and (d) Poling field dependence of the P–B *curves at* T=*5 K for (c)* $\mathbf{E} \,||\, \mathrm{y}$ *and* $\mathbf{B} \,||\, \mathrm{x}$ *and (d)* $\mathbf{E} \,||\, \mathrm{x}$ *and* $\mathbf{B} \,||\, \mathrm{y}$ *poling field configurations. The color codes of (c) and (d) are shown in (a) and (b), respectively. The slopes of the* P-B *curves correspond to* χ_{yx} *and* χ_{xy} *in (c) and (d), respectively. The sign of the ME effect depends on the relative signs of the poling fields; note the complete overlap of the red and orange as well as the blue and green curves. (e)–(h) Optical absorption spectra measured at* T=*5 K. (e) and (g) with poling configurations indicated in (a) and (f) and (h) with poling configurations shown in (b). Spectra in (e) and (f) were measured using linearly polarized light with* $\mathbf{E}_\omega \,||\, \mathrm{y}$ *and* $\mathbf{B}_\omega \,||\, \mathrm{x}$*, while those in (g,h) were measured with* $\mathbf{E}_\omega \,||\, \mathrm{x}$ *and* $\mathbf{B}_\omega \,||\, \mathrm{y}$*. Figure reproduced from Ref. III.*

5 Achievements

The major achievements of my Ph.D. research are summarized in the following points:

1. I designed and constructed a rotating Voigt probe which is capable of high precision sample rotation inside the magnet bore at cryogenic temperatures. This probe has found a great deal of use as it makes possible to measure several sample orientations during the same cooldown without taking the probe out. Additionally it grants the possibility of measuring a large number of sample rotations which would not have been feasible using the old hardware. This made possible the rotation dependence measurements for $CaBaCo_4O_7$. (Ref. I)

2. I designed and constructed a High Voltage High Temperature Voigt probe that makes it possible for the measurements to be conducted at high temperatures [11] and apply a high voltage to the sample crystal. (Ref. III)

3. I designed and built a filter wheel that is capable of reproducible filter changes during the experiments. What is more, the filters can be changed in high magnetic field. This makes it possible to plan experiments in a considerably more efficient way thus saving a lot of time and, more importantly, producing reproducible results.

4. I measured the angle dependence of $CaBaCo_4O_7$ in magnetic field. The threefold splitting of the spin-wave frequencies proved the crystal to be hexagonally twinned. This information was valuable for the construction of a microscopic spin model of $CaBaCo_4O_7$ consisting of triangular array of bitetrahedral *c*-axis chains ferrimagnetically coupled to each other in the *ab* plane. (Ref. I)

5. Using the optical and magnetization data I estimated that roughly one fifth of the $CaBaCo_4O_7$ sample is in domain I with the **a** axis along [1,0,0] while the rest of the sample is in the two other domains. (Ref. I)

6. I measured and reported the existence of the nonreciprocal directional dichroism in $Sr_2CoSi_2O_7$ at a broad range of magnetic fields and temperatures. I discovered the existence of nonreciprocal directional dichroism in the paramagnetic phase up to temperatures more than 10 times higher than Néel temperature of $Sr_2CoSi_2O_7$. (Ref. II)

7. The measured temperature dependence of the spin-mode frequencies, their intensities and the sign of the nonreciprocal directional dichroism in $Sr_2CoSi_2O_7$ helped to create a detailed theoretical analysis of spin excitations which helps to identify the key paramaters responsible for high-temperature nonreciprocal directional dichroism. (Ref. II)

8. I studied the optical magnetoelectric effect in $LiCoPO_4$ using optical directional anisotropy as measured by the THz absorption spectroscopy of spin resonances. $LiCoPO_4$ has two possible antiferromagnetic domains with opposite signs of the magneto-electric coupling, which can be selected by the application of orthogonal electric $\mathbf{E}$ and magnetic $\mathbf{B}$ fields. I found several magnetic resonances showing large remnant directional anisotropy persisting even after the removal of the crossed poling fields.(Ref. III)

9. I developed several programs for fitting peaks, processing data and plotting the spectra. These programs have been extensively used by most members of our group for analyzing the data and creating publishing-ready figures. This work has saved countless hours of work and produced figures for several publications [102–104].

6 Conclusions

To conclude, the goal of understanding magnetoelectric effects in three selected multiferroic materials is fulfilled. New findings of this thesis are following:

1. We have presented a nearly complete solution for the magnetization, spin state, and mode frequencies of the swedenborgite $CaBaCo_4O_7$. We have constructed a microscopic spin model of $CaBaCo_4O_7$ from the dependence of THz absorption spectra on the direction of magnetic field with respect to the crystal axes. This model shows that competing exchange interactions between *c*-axis spin chains produce the spin-induced electric polarization in this material.

2. We have shown that the directional dichroism of THz absorption occurs above magnetic ordering temperature in $Sr_2CoSi_2O_7$. We have explained the directional dichroism effect with the hybridization mechanism taking place on a single spin site. The applied magnetic field aligns spins above the magnetic ordering temperature and through the hybridization mechanism a macroscopic electric polarization is induced.

3. We have found electromagnons and magnetoelectric excitations in addition to conventional magnon modes in $LiCoPO_4$ with THz spectroscopy. We have determined the static magnetoelectric susceptibility tensor components from the THz non-reciprocal directional dichroism spectra using the magnetoelectric sum rule. We concluded that the static magnetoelectric effect is induced by magnetoelectric spin resonances and the symmetric part of magnetoelectric susceptibility tensor dominates over the antisymmetric part.

List of Figures

1 Multiferroic interactions 13
2 Time-reversal and spatial-inversion symmetry in ferroics 14
3 Static ME effect in $Sr_2CoSi_2O_7$ 15
4 Three major mechanisms of ME coupling 21
5 *p* – *d* hybridization mechanism. 23
6 Michelson interferometer 25
7 Martin-Puplett interferometer 26
8 TeslaFIR spectrometer layout 28
9 Faraday and Voigt geometry 29
10 Rotating Voigt probe layout 30
11 HT HV Voigt probe 31
12 HT HV Voigt probe side view 32
13 $LiCoPO_4$ sample with HV gold wires 32
14 Filter wheel housing 33
15 Different filter spectra 34
16 Temperature sensor calibration probe 35
17 Nijmegen Cell 3 Bitter magnet setup 36
18 Example interferogram and spectrum 37
19 Relative transmittance and absorbance spectra 38
20 0 T and 15 T spectra compared 38
21 Final calculated spectra 39
22 FitPeaks file selection box 40
23 FitPeaks main fitting window 41
24 FitPeaks fit result visualized 41
25 $CaBaCo_4O_7$ crystal structure. 43
26 Magnetic field dependence of absorption spectra of $CaBaCo_4O_7$ at 4 K 44
27 $CaBaCo_4O_7$ spectra as a function of angle 45
28 $CaBaCo_4O_7$ line positions as a function of angle 46
29 Schematic crystal structure of $Sr_2CoSi_2O_7$ 47
30 $Sr_2CoSi_2O_7$ absorption spectra and calculated susceptibilities 48
31 Unit cell and two different domains in $LiCoPO_4$ 49
32 Remnant static and dynamic ME effects in $LiCoPO_4$ 51

References

[1] M. Gajek, M. Bibes, S. Fusil, K. Bouzehouane, J. Fontcuberta, A. Barthélémy, and A. Fert, “Tunnel junctions with multiferroic barriers,” *Nature Materials*, vol. 6, pp. 296–302, Apr. 2007.

[2] F. Matsukura, Y. Tokura, and H. Ohno, “Control of magnetism by electric fields,” *Nat Nano*, vol. 10, pp. 209–220, Mar. 2015.

[3] K. Wang, J.-M. Liu, and Z. Ren, “Multiferroicity: the coupling between magnetic and polarization orders,” *Advances in Physics*, vol. 58, no. 4, pp. 321–448, 2009.

[4] T. Arima, “Magneto-electric optics in non-centrosymmetric ferromagnets,” *J. Phys.: Condens. Matter*, vol. 20, no. 43, p. 434211, 2008.

[5] J. J. Hopfield and D. G. Thomas, “Photon momentum effects in the magneto-optics of excitons,” *Phys. Rev. Lett.*, vol. 4, pp. 357–359, Apr 1960.

[6] G. L. J. A. Rikken and E. Raupach, “Observation of magneto-chiral dichroism,” *Nature*, vol. 390, pp. 493–494, 1997.

[7] G. L. J. A. Rikken, C. Strohm, and P. Wyder, “Observation of magnetoelectric directional anisotropy,” *Phys. Rev. Lett.*, vol. 89, p. 133005, Sep 2002.

[8] I. Kézsmárki, N. Kida, H. Murakawa, S. Bordács, Y. Onose, and Y. Tokura, “Enhanced directional dichroism of terahertz light in resonance with magnetic excitations of the multiferroic $Ba_2CoGe_2O_7$ oxide compound,” *Phys. Rev. Lett.*, vol. 106, p. 057403, Feb 2011.

[9] A. M. Kuzmenko, D. Szaller, T. Kain, V. Dziom, L. Weymann, A. Shuvaev, A. Pimenov, A. A. Mukhin, V. Y. Ivanov, I. A. Gudim, L. N. Bezmaternykh, and A. Pimenov, “Switching of magnons by electric and magnetic fields in multiferroic borates,” *Phys. Rev. Lett.*, vol. 120, p. 027203, Jan 2018.

[10] V. Kocsis, K. Penc, T. Rõõm, U. Nagel, J. Vít, J. Romhányi, Y. Tokunaga, Y. Taguchi, Y. Tokura, I. Kézsmárki, and S. Bordács, “Identification of antiferromagnetic domains via the optical magnetoelectric effect,” *Phys. Rev. Lett.*, vol. 121, p. 057601, Aug 2018.

[11] I. Kézsmárki, U. Nagel, S. Bordács, R. S. Fishman, J. H. Lee, H. T. Yi, S.-W. Cheong, and T. Rõõm, “Optical diode effect at spin-wave excitations of the room-temperature multiferroic $BiFeO_3$,” *Phys. Rev. Lett.*, vol. 115, p. 127203, Sep 2015.

[12] A. Pimenov, A. A. Mukhin, V. Y. Ivanov, V. D. Travkin, A. M. Balbashov, and A. Loidl, “Possible evidence for electromagnons in multiferroic manganites,” *Nature Physics*, vol. 2, pp. 97–100, 2006.

[13] D. Talbayev, A. D. LaForge, S. A. Trugman, N. Hur, A. J. Taylor, R. D. Averitt, and D. N. Basov, “Magnetic exchange interaction between rare-earth and Mn ions in multiferroic hexagonal manganites,” *Phys. Rev. Lett.*, vol. 101, no. 24, p. 247601, 2008.

[14] U. Nagel, R. S. Fishman, T. Katuwal, H. Engelkamp, D. Talbayev, H. T. Yi, S.-W. Cheong, and T. Rõõm, “Terahertz spectroscopy of spin waves in multiferroic $BiFeO_3$ in high magnetic fields,” *Phys. Rev. Lett.*, vol. 110, p. 257201, Jun 2013.

[15] H. Schmid, “Multi-ferroic magnetoelectrics,” *Ferroelectrics*, vol. 162, no. 1, p. 317, 1994.

[16] M. Fiebig, “Revival of magnetoelectric effect,” *J. Phys. D: Appl. Phys.*, vol. 38, pp. R123–R152, 2005.

[17] N. Hur, P. A. Sharma, J. S. Ahn, S. Guha, and S.-W. Cheong, “Electric polarization reversal and memory in a multiferroic material induced by magnetic fields,” *Nature*, vol. 429, pp. 392–395, 2004.

[18] S.-W. Cheong and M. Mostovoy, “Multiferroics: a magnetic twist for ferroelectricity,” *Nature Mater.*, vol. 6, pp. 13–20, 2007.

[19] R. Ramesh, R. and N. A. Spaldin, “Multiferroics: progress and prospects in thin films,” *Nature Materials*, vol. 6, p. 21, 2007.

[20] S. Manipatruni, D. E. Nikonov, and I. A. Young, “Beyond CMOS computing with spin and polarization,” *Nature Physics*, vol. 14, pp. 338–343, Apr. 2018.

[21] S. Manipatruni, D. E. Nikonov, C.-C. Lin, T. A. Gosavi, H. Liu, B. Prasad, Y.-L. Huang, E. Bonturim, R. Ramesh, and I. A. Young, “Scalable energy-efficient magnetoelectric spin-orbit logic,” *Nature*, vol. 565, pp. 35–42, Jan. 2019.

[22] N. A. Spaldin and R. Ramesh, “Advances in magnetoelectric multiferroics,” *Nature Materials*, vol. 18, pp. 203–212, Mar. 2019.

[23] N. A. Spaldin and M. Fiebig, “The renaissance of magnetoelectric multiferroics,” *Science*, vol. 309, no. 5733, pp. 391–392, 2005.

[24] W. Eerenstein, N. D. Mathur, and J. F. Scott, “Multiferroic and magnetoelectric materials,” *Nature*, vol. 442, pp. 759–765, 2006.

[25] C. A. F. Vaz, J. Hoffman, C. H. Ahn, and R. Ramesh, “Magnetoelectric coupling effects in multiferroic complex oxide composite structures,” *Advanced Materials*, vol. 22, no. 26-27, pp. 2900–2918, 2010.

[26] D. Khomskii, “Classifying multiferroics: Mechanisms and effects,” *Physics*, vol. 2, p. 20, Mar 2009.

[27] J. R. Teague, R. Gerson, and W. J. James, “Dielectric hysteresis in single crystal $BiFeO_3$,” *Solid State Commun.*, vol. 8, pp. 1073–1074, 1970.

[28] J. Wang, J. B. Neaton, H. Zheng, V. Nagarajan, S. B. Ogale, B. Liu, D. Viehland, V. Vaithyanathan, D. G. Schlom, U. V. Waghmare, N. A. Spaldin, K. M. Rabe, M. Wuttig, and R. Ramesh, “Epitaxial $BiFeO_3$ multiferroic thin film heterostructures,” *Science*, vol. 299, p. 1719, 2003.

[29] T. Kimura, T. Goto, H. Shintani, K. Ishizaka, T. Arima, and Y. Y. Tokura, “Magnetic control of ferroelectric polarization,” *Nature*, vol. 426, p. 55, 2003.

[30] C. Lu and J.-M. Liu, “$DyMnO_3$: A model system of type-II multiferroics,” *Journal of Materiomics*, vol. 2, no. 3, pp. 213 – 224, 2016.

[31] N. A. Hill, “Why are there so few magnetic ferroelectrics?,” *J. Phys. Chem. B*, vol. 104, pp. 6694–6709, 2000.

[32] T. H. O’Dell, “The field invariants in a magneto-electric medium,” *The Philosophical Magazine: A Journal of Theoretical Experimental and Applied Physics*, vol. 8, no. 87, pp. 411–418, 1963.

[33] N. A. Spaldin, M. Fiebig, and M. Mostovoy, "The toroidal moment in condensed-matter physics and its relation to the magnetoelectric effect," *Journal of Physics: Condensed Matter*, vol. 20, no. 43, p. 434203, 2008.

[34] I. E. Dzyaloshinskii, "On the magneto-electrical effect in antiferromagnets," *Journal of Experimental and Theoretical Physics*, vol. 10, p. 628, Mar. 1960.

[35] D. N. Astrov, "The magnetoelectric effect in antiferromagnetics," *JETP*, vol. 38, pp. 984–985, Sept. 1960.

[36] D. Khomskii, "Multiferroics: Different ways to combine magnetism and ferroelectricity," *Journal of Magnetism and Magnetic Materials*, vol. 306, no. 1, pp. 1 – 8, 2006.

[37] T. Kimura, "Spiral magnets as magnetoelectrics," *Annual Review of Materials Research*, vol. 37, no. 1, pp. 387–413, 2007.

[38] C. M. Leung, J. Li, D. Viehland, and X. Zhuang, "A review on applications of magnetoelectric composites: from heterostructural uncooled magnetic sensors, energy harvesters to highly efficient power converters," *Journal of Physics D: Applied Physics*, vol. 51, p. 263002, Jun 2018.

[39] M. Akaki, H. Iwamoto, T. Kihara, M. Tokunaga, and H. Kuwahara, "Multiferroic properties of an åkermanite $Sr_2CoSi_2O_7$ single crystal in high magnetic fields," *Phys. Rev. B*, vol. 86, p. 060413, Aug 2012.

[40] L. D. Barron, *Molecular Light Scattering and Optical Activity*. Cambridge University Press, 2 ed., 2004.

[41] I. Kézsmárki, D. Szaller, S. Bordács, V. Kocsis, Y. Tokunaga, Y. Taguchi, H. Murakawa, Y. Tokura, H. Engelkamp, T. Rõõm, and U. Nagel, "One-way transparency of four-coloured spin-wave excitations in multiferroic materials," *Nature Comm.*, vol. 5, p. 3203, 2014.

[42] D. Szaller, S. Bordács, and I. Kézsmárki, "Symmetry conditions for nonreciprocal light propagation in magnetic crystals," *Phys. Rev. B*, vol. 87, p. 014421, Jan 2013.

[43] J. D. Jackson, *Classical electrodynamics*. John Wiley & Sons, Inc., third ed., 1998.

[44] S. Miyahara and N. Furukawa, "Theory of magneto-optical effects in helical multiferroic materials via toroidal magnon excitation," *Phys. Rev. B*, vol. 89, p. 195145, May 2014.

[45] D. Szaller, S. Bordács, V. Kocsis, T. Rõõm, U. Nagel, and I. Kézsmárki, "Effect of spin excitations with simultaneous magnetic- and electric-dipole character on the static magnetoelectric properties of multiferroic materials," *Phys. Rev. B*, vol. 89, p. 184419, May 2014.

[46] R. Kubo, "Statistical-mechanical theory of irreversible processes. I. general theory and simple applications to magnetic and conduction problems," *Journal of the Physical Society of Japan*, vol. 12, no. 6, pp. 570–586, 1957.

[47] H. Kuzmany, *Solid-state spectroscopy*. Springer-Verlag, 2nd ed., 2009.

[48] M. Dressel and G. Grüner, *Electrodynamics of solids*. Cambridge University Press, 2002.

[49] S. Dong, J.-M. Liu, S.-W. Cheong, and Z. Ren, "Multiferroic materials and magnetoelectric physics: symmetry, entanglement, excitation, and topology," *Adv. Phys.*, vol. 64, no. 5-6, pp. 519–626, 2015.

[50] C. Jia, S. Onoda, N. Nagaosa, and J. H. Han, "Bond electronic polarization induced by spin," *Phys. Rev. B*, vol. 74, no. 22, p. 224444, 2006.

[51] C. Jia, S. Onoda, N. Nagaosa, and J. H. Han, "Microscopic theory of spin-polarization coupling in multiferroic transition metal oxides," *Phys. Rev. B*, vol. 76, no. 14, p. 144424, 2007.

[52] Y. Tokura, S. Seki, and N. Nagaosa, "Multiferroics of spin origin," *Reports on Progress in Physics*, vol. 77, no. 7, p. 076501, 2014.

[53] Y. J. Choi, H. T. Yi, S. Lee, Q. Huang, V. Kiryukhin, and S.-W. Cheong, "Ferroelectricity in an Ising chain magnet," *Phys. Rev. Lett.*, vol. 100, p. 047601, Jan 2008.

[54] Y. Tokunaga, S. Iguchi, T. Arima, and Y. Tokura, "Magnetic-field-induced ferroelectric state in $DyFeO_3$," *Phys. Rev. Lett.*, vol. 101, p. 097205, Aug 2008.

[55] I. A. Sergienko and E. Dagotto, "Role of the Dzyaloshinskii-Moriya interaction in multiferroic perovskites," *Phys. Rev. B*, vol. 73, no. 9, p. 094434, 2006.

[56] M. Mostovoy, "Ferroelectricity in spiral magnets," *Phys. Rev. Lett.*, vol. 96, no. 6, p. 067601, 2006.

[57] H. Katsura, N. Nagaosa, and A. V. Balatsky, "Spin current and magnetoelectric effect in noncollinear magnets," *Phys. Rev. Lett.*, vol. 95, p. 057205, Jul 2005.

[58] T. Arima, "Ferroelectricity induced by proper-screw type magnetic order," *J. Phys. Soc. Jpn.*, vol. 76, no. 7, p. 073702, 2007.

[59] H. Kimura, S. Kobayashi, Y. Fukuda, T. Osawa, Y. Kamada, Y. Noda, I. Kagomiya, and K. Kohn, "Spiral spin structure in the commensurate magnetic phase of multiferroic $R\mathrm{Mn}_2\mathrm{O}_5$," *Journal of the Physical Society of Japan*, vol. 76, no. 7, p. 074706, 2007.

[60] I. A. Sergienko, C. Şen, and E. Dagotto, "Ferroelectricity in the magnetic E-phase of orthorhombic perovskites," *Phys. Rev. Lett.*, vol. 97, no. 22, p. 227204, 2006.

[61] L. C. Chapon, P. G. Radaelli, G. R. Blake, S. Park, and S.-W. Cheong, "Ferroelectricity induced by acentric spin-density waves in YMn_2O_5," *Phys. Rev. Lett.*, vol. 96, no. 9, p. 097601, 2006.

[62] R. D. Johnson, K. Cao, F. Giustino, and P. G. Radaelli, "$CaBaCo_4O_7$: A ferrimagnetic pyroelectric," *Phys. Rev. B*, vol. 90, p. 045129, Jul 2014.

[63] M. Kenzelmann, A. B. Harris, S. Jonas, C. Broholm, J. Schefer, S. B. Kim, C. L. Zhang, S.-W. Cheong, O. P. Vajk, and J. W. Lynn, "Magnetic inversion symmetry breaking and ferroelectricity in $TbMnO_3$," *Phys. Rev. Lett.*, vol. 95, no. 8, p. 087206, 2005.

[64] T. Goto, T. Kimura, G. Lawes, A. P. Ramirez, and Y. Tokura, "Ferroelectricity and giant magnetocapacitance in perovskite rare-earth manganites," *Phys. Rev. Lett.*, vol. 92, p. 257201, Jun 2004.

[65] Y. Yamasaki, S. Miyasaka, T. Goto, H. Sagayama, T. Arima, and Y. Tokura, “Ferroelectric phase transitions of $3d$-spin origin in $Eu_{1-x}Y_xMnO_3$,” *Phys. Rev. B*, vol. 76, p. 184418, Nov 2007.

[66] R. S. Fishman, J. H. Lee, S. Bordács, I. Kézsmárki, U. Nagel, and T. Rõõm, “Spin-induced polarizations and nonreciprocal directional dichroism of the room-temperature multiferroic $BiFeO_3$,” *Phys. Rev. B*, vol. 92, p. 094422, Sep 2015.

[67] H. T. Yi, Y. J. Choi, S. Lee, and S.-W. Cheong, “Multiferroicity in the square-lattice antiferromagnet of $Ba_2CoGe_2O_7$,” *Appl. Phys. Lett.*, vol. 92, no. 21, pp. –, 2008.

[68] H. Murakawa, Y. Onose, S. Miyahara, N. Furukawa, and Y. Tokura, “Ferroelectricity induced by spin-dependent metal-ligand hybridization in $Ba_2CoGe_2O_7$,” *Phys. Rev. Lett.*, vol. 105, p. 137202, Sep 2010.

[69] M. Akaki, T. Tadokoro, T. Kihara, M. Tokunaga, and H. Kuwahara, “High magnetic field dependence of magnetodielectric properties in $Sr_2CoSi_2O_7$ crystal,” *J. Low Temp. Phys.*, vol. 170, no. 5-6, pp. 291–295, 2013.

[70] H. Murakawa, Y. Onose, S. Miyahara, N. Furukawa, and Y. Tokura, “Comprehensive study of the ferroelectricity induced by the spin-dependent d-p hybridization mechanism in $Ba_2XGe_2O_7$ (X = Mn, Co, and Cu),” *Phys. Rev. B*, vol. 85, p. 174106, May 2012.

[71] M. Akaki, J. Tozawa, D. Akahoshi, and H. Kuwahare, “Gigantic magnetoelectric effect caused by magnetic-field-induced canted antiferromagnetic-paramagnetic transition in quasi-two-dimensional $Ca_2CoSi_2O_7$ crystal,” *Appl. Phys. Lett.*, vol. 94, p. 212904, 2009.

[72] M. Akaki, H. Kuwahara, A. Matsuo, K. Kindo, and M. Tokunaga, “Successive magnetic transitions of $Ca_2CoSi_2O_7$ in high magnetic fields,” *Journal of the Physical Society of Japan*, vol. 83, no. 9, p. 093704, 2014.

[73] J. Chamberlain, G. W. Chantry, and N. W. B. Stone, *The principles of interferometric spectroscopy / John Chamberlain; completed, collated, and edited by G. W. Chantry and N. W. B. Stone*. Wiley, Chichester [Eng.]; New York:, 1979.

[74] C. Porter and D. Tanner, “Correction of phase errors in fourier spectroscopy,” *Int. J. Infrared Millimeter Waves*, vol. 4, no. 2, pp. 273–298, 1983.

[75] K. Button and J. Wiltse, *Infrared and Millimeter Waves: Systems and components*. Infrared and Millimeter Waves, Academic Press, 1982.

[76] D. Martin and E. Puplett, “Polarised interferometric spectrometry for the millimetre and submillimetre spectrum,” *Infrared Phys.*, vol. 10, no. 2, pp. 105 – 109, 1969.

[77] R. Loudon, *The Quantum Theory of Light*. London - New York - Toronto: Oxford University Press, second ed., 1983.

[78] M. Kimmitt, J. Walsh, C. Platt, K. Miller, and M. Jensen, “Infrared output from a compact high pressure arc source,” *Infrared Phys. Technol.*, vol. 37, no. 4, pp. 471 – 477, 1996.

[79] M. Halpern, H. P. Gush, E. Wishnow, and V. De Cosmo, “Far infrared transmission of dielectrics at cryogenic and room temperatures: glass, fluorogold, eccosorb, stycast, and various plastics,” *Appl. Opt.*, vol. 25, pp. 565–570, 1986.

[80] T. Timusk and P. L. Richards, “Near millimeter wave bandpass filters,” *Appl. Opt.*, vol. 20, pp. 1355–1360, Apr 1981.

[81] T. E. Oliphant, *A guide to NumPy*, vol. 1. Trelgol Publishing USA, 2006.

[82] J. D. Hunter, “Matplotlib: A 2D graphics environment,” *Computing in Science & Engineering*, vol. 9, no. 3, pp. 90–95, 2007.

[83] P. Eilers and H. Boelens, “Baseline correction with asymmetric least squares smoothing,” *Unpubl. Manuscr*, Nov. 2005.

[84] M. A. Branch, T. F. Coleman, and Y. Li, “A subspace, interior, and conjugate gradient method for large-scale bound-constrained minimization problems,” *SIAM Journal on Scientific Computing*, vol. 21, no. 1, pp. 1–23, 1999.

[85] V. Caignaert, A. Maignan, K. Singh, C. Simon, V. Pralong, B. Raveau, J. F. Mitchell, H. Zheng, A. Huq, and L. C. Chapon, “Gigantic magnetic-field-induced polarization and magnetoelectric coupling in a ferrimagnetic oxide $\mathrm{CaBaCo_4O_7}$,” *Phys. Rev. B*, vol. 88, p. 174403, Nov 2013.

[86] B. Raveau, V. Pralong, V. Caignaert, and A. Maignan, “Swedenborgite-type cobaltites and ferrites: Tetrahedral frameworks with exceptional magnetic properties,” *Zeitschrift für anorganische und allgemeine Chemie*, vol. 637, no. 9, pp. 1079–1087, 2011.

[87] B. Raveau, V. Caignaert, V. Pralong, D. Pelloquin, and A. Maignan, “A series of novel mixed valent ferrimagnetic oxides with a T_C up to 270 K: $\mathrm{Ca_{1-x}Y_xBaFe_4O_7}$,” *Chem. Mater.*, vol. 20, pp. 6295–6297, Oct. 2008.

[88] V. Caignaert, V. Pralong, A. Maignan, and B. Raveau, “Orthorhombic kagome cobaltite $\mathrm{CaBaCo_4O_7}$: A new ferrimagnet with a of 70 K,” *Solid State Communications*, vol. 149, no. 11-12, pp. 453 – 455, 2009.

[89] V. Caignaert, V. Pralong, V. Hardy, C. Ritter, and B. Raveau, “Magnetic structure of $\mathrm{CaBaCo_4O_7}$: Lifting of geometrical frustration towards ferrimagnetism,” *Phys. Rev. B*, vol. 81, p. 094417, Mar 2010.

[90] S. Bordács, V. Kocsis, Y. Tokunaga, U. Nagel, T. Rõõm, Y. Takahashi, Y. Taguchi, and Y. Tokura, “Unidirectional terahertz light absorption in the pyroelectric ferrimagnet $\mathrm{CaBaCo_4O_7}$,” *Phys. Rev. B*, vol. 92, p. 214441, Dec 2015.

[91] Z. Qu, L. Ling, L. Zhang, L. Pi, and Y. Zhang, “Magnetic properties of the ferrimagnetic cobaltite $\mathrm{CaBaCo_4O_7}$,” *Solid State Communications*, vol. 151, no. 13, pp. 917 – 919, 2011.

[92] H. Iwamoto, M. Ehara, M. Akaki, and H. Kuwahara, “Magnetoelectric property in 3d transition metal oxide with tetrahedral structure,” *Journal of Physics: Conference Series*, vol. 400, p. 032031, dec 2012.

[93] M. M. Seikh, T. Sarkar, V. Pralong, V. Caignaert, and B. Raveau, "Dramatic effect of a-site substitution upon the structure and magnetism of the "114" $CaBaCo_4O_7$ cobaltite," *Phys. Rev. B*, vol. 86, p. 184403, Nov 2012.

[94] M. M. Seikh, V. Caignaert, V. Pralong, and B. Raveau, "High sensitivity of magnetism of the "114" ferrimagnet $CaBaCo_4O_7$ to stoichiometry deviation," *Journal of Physics and Chemistry of Solids*, vol. 75, no. 1, pp. 79 – 85, 2014.

[95] S. Bordács, I. Kézsmárki, D. Szaller, L. Demkó, N. Kida, H. Murakawa, Y. Onose, R. Shimano, T. Rõõm, U. Nagel, S. Miyahara, N. Furukawa, and Y. Tokura, "Chirality of matter shows up via spin excitations," *Nature Physics*, vol. 8, pp. 734–738, 2012.

[96] K. Penc, J. Romhányi, T. Rõõm, U. Nagel, A. Antal, T. Fehér, A. Jánossy, H. Engelkamp, H. Murakawa, Y. Tokura, D. Szaller, S. Bordács, and I. Kézsmárki, "Spin-stretching modes in anisotropic magnets: Spin-wave excitations in the multiferroic $Ba_2CoGe_2O_7$," *Phys. Rev. Lett.*, vol. 108, p. 257203, Jun 2012.

[97] J.-P. Rivera, "The linear magnetoelectric effect in $LiCoPO_4$ revisited," *Ferroelectrics*, vol. 161, no. 1, pp. 147–164, 1994.

[98] I. Kornev, M. Bichurin, J.-P. Rivera, S. Gentil, H. Schmid, A. G. M. Jansen, and P. Wyder, "Magnetoelectric properties of $LiCoPO_4$ and $LiNiPO_4$," *Phys. Rev. B*, vol. 62, pp. 12247–12253, Nov 2000.

[99] A. S. Zimmermann, D. Meier, and M. Fiebig, "Ferroic nature of magnetic toroidal order," *Nat. Commun.*, vol. 5, p. 4796, Sept. 2014.

[100] M. Mercier, J. Gareyte, and E. F. Bertaut, "Une nouvelle famille de corps magnétoélectriques: $LiMPO_4$ (M = Mn, Co, Ni)," *C. R. Acad. Sc. Paris*, vol. 264, pp. 979–982, Mar. 1967.

[101] F. Wooten, *Optical Properties of Solids*. Academic Press Inc., i ed., 1972.

[102] K. Amelin, U. Nagel, R. S. Fishman, Y. Yoshida, H. Sim, K. Park, J.-G. Park, and T. Rõõm, "Terahertz absorption spectroscopy study of spin waves in orthoferrite $YFeO_3$ in a magnetic field," *Phys. Rev. B*, vol. 98, p. 174417, Nov 2018.

[103] L. Peedu, V. Kocsis, D. Szaller, J. Viirok, U. Nagel, T. Rõõm, D. G. Farkas, S. Bordács, D. L. Kamenskyi, U. Zeitler, Y. Tokunaga, Y. Taguchi, Y. Tokura, and I. Kézsmárki, "Spin excitations of magnetoelectric $LiNiPO_4$ in multiple magnetic phases," *Phys. Rev. B*, vol. 100, p. 024406, Jul 2019.

[104] J. Viirok, U. Nagel, T. Rõõm, D. G. Farkas, P. Balla, D. Szaller, V. Kocsis, Y. Tokunaga, Y. Taguchi, Y. Tokura, B. Bernáth, D. L. Kamenskyi, I. Kézsmárki, S. Bordács, and K. Penc, "Directional dichroism in the paramagnetic state of multiferroics: A case study of infrared light absorption in $Sr_2CoSi_2O_7$ at high temperatures," *Phys. Rev. B*, vol. 99, p. 014410, Jan 2019.

Acknowledgements

This work is dedicated to my son. You have made me stronger, better and more fulfilled than I could have ever imagined. I also thank my fiancée for her love, patience and unwavering support. She has made my life richer in countless ways. She has been there for me through it all even as she herself walks the path of graduate school. This work would not have been possible without her absolute trust in me.

I am most thankful to my supervisors T. Rõõm and U. Nagel for taking the time to teach me how scientific discoveries are made in contemporary science and the amount of dedication it demands. Without their expert guidance, advice, stimulating suggestions, and encouragement, this work would not have been possible. I am very happy and lucky to have worked in his group for the past few years and learned a lot from these smart and successful scientists. Furthermore, all the members of the TeslaFIR group, past and present, were good friends and excellent teachers in the workings of the lab.

I acknowledge financial support for this research from the Estonian Ministry of Education and Research with institutional research funding IUT23-3 and by the European Regional Development Fund Project No. TK134. I also acknowledge the support of the HFML-RU/FOM, member of the European Magnetic Field Laboratory (EMFL).

Abstract
The Study of Magnetoelectric Effect in Multiferroics Using THz Spectroscopy

The way in which light interacts with materials is determined by the optical properties of these materials. By measuring these properties one can obtain information about low energy excitations that govern the material's magnetic and electric properties. Electric properties of solids are usually governed by the charge degrees of freedom whereas the magnetic properties are dictated by the spin degrees of freedom and these sets are nearly decoupled. The coexisting magnetic and ferroelectric orders in multiferroic materials give rise to a handful of novel magnetoelectric (ME) phenomena, such as the absorption difference for the opposite propagation directions of light, called the nonreciprocal directional dichroism (NDD). These materials offer the possibility of their future applications in terahertz photonics as optical diodes transmitting unpolarized light in one but not in the opposite direction. Another interesting effect is electric (magnetic) field control of magnetism (polarization) called the magnetoelectric effect. A possible application could be data storage combining the best qualities of ferroelectric and magnetoresistive memories: fast low-power electrical read and write operation inherently coupled to a non-destructive non-volatile magnetic data storage unit. Usually, these effects are restricted to low temperature, where the multiferroic phase develops, seriously limiting the applications.

As the zero frequency (dc) ME effect is determined by the excitations at finite frequencies, the key to understanding the dc effect is an adequate description of low frequency excitations. Linear ME effect is mostly governed by sub-THz frequency spin excitations. Spin excitations are magnetic excitations and do not modulate the electric polarization in general but in ME multiferroics this unusual feature is present. Although inelastic neutron scattering is a powerful tool for studying spin excitations it lacks the sensitivity to electric component induced spin dynamics. Therefore, electromagnetic radiation with oscillating electric and magnetic fields is an ideal tool to probe ME spin excitations. THz spectroscopy is the tool that matches the frequency range of spin excitations in multiferroics.

The spin excitations of three multiferroic materials were studied by infrared absorption spectroscopy in the THz spectral range as a function of magnetic field and temperature. Experiments were mostly carried out in National Institute of Chemical Physics and Biophysics using a Fourier-transform THz spectrometer. Samples were cooled to cryogenic temperatures and magnetic fields were generated by a superconducting magnet. Faraday and Voigt geometry experiments were performed for measuring all the possible orientations of electric and magnetic components of radiation relative to crystal axes. Two Voigt probes with the option to apply electric field for magnetoelectric poling were designed and constructed to make these measurements possible.

Generally, complex magnetic states with spin-induced electric polarizations can be produced by competing exchange interactions. With these competing interactions on alternating triangular and Kagome layers, the swedenborgite $\mathrm{CaBaCo_4O_7}$ may have one of the largest measured spin-induced polarizations of $\sim$1700 nC/cm^2 below its ferrimagnetic transition temperature at 70 K. When the magnetic field is rotated in the *ab* plane, the threefold splitting of the spin-wave frequencies indicates that the sample has hexagonally twinned domains. Several measurement techniques, including our THz spectroscopy, revealed that the complex spin order in the domains can be characterized as a triangular array of bi-tetrahedral *c*-axis chains that are ferrimagnetically coupled to each other in the *ab* plane. Despite its fixed permanent electric polarization, this swedenborgite may yet have important technological applications utilizing the large changes in the spin-induced

polarization when a modest magnetic field below 1 T is applied along *b* in the vicinity of T_C. Above all, our work illuminates a pathway to develop other functional materials with sizable magnetic moments and electrical polarizations.

Spin excitations in the second compound, melilite $Sr_2CoSi_2O_7$, were measured in magnetic fields up to 30 T at temperatures much higher than the magnetic ordering temperature. Almost perfect one way transparency is seen in some spin wave modes at temperatures up to 100 K, although the magnetic ordering temperature is only T_N=7 K. What is more, the NDD increases above the Néel temperature in high magnetic field. This is unusual in multiferroics but is readily explained by the ME coupling mechanism on a single spin site called the spin-dependent hybridization mechanism. The main experimental findings, the temperature dependence of the spin-mode frequencies, their intensities, the selection rules and the sign of the magneto chiral dichroism (MChD) for the different spin modes, are described by the exact diagonalization of a four-spin cluster.

The third compound, a crystal of antiferromagnetic $LiCoPO_4$, was studied by ME poling, i.e. by cooling the sample below the magnetic ordering temperature in applied electric and magnetic fields. This antiferromagnet with olivine-type crystal structure has two antiferromagnetic domain states with opposite signs of the ME coupling. One or the other domain is selected by the simultaneous application of $\mathbf{E}$ and $\mathbf{B}$ poling fields orthogonal to each other. When selecting one of the domains by ME poling, the material shows optical NDD without any external fields. The more transparent and absorbing directions are interchanged for the two domains and therefore the ME domain state could be read out with THz radiation. By analyzing the selection rules and comparing the strengths of the absorption peaks in the different antiferromagnetic domains, electromagnons and ME spin resonances were identified in addition to conventional magnetic dipole active spin-wave excitations.

To summarize, in this thesis we have shown that concurrent exchange interactions in $CaBaCo_4O_7$ create a magnetically ordered state where spin system induces a magnetic field dependent electric polarization. In $Sr_2CoSi_2O_7$ the nonreciprocal directional dichroism of THz absorption occurs also in the paramagnetic phase up to 100 K, much higher than the Néel temperature of 7 K, caused by the excitations of the 3/2 spins of Co^{2+} ions in the anisotropic crystal. The elements of the magnetoelectric susceptibility tensor were determined from the THz range nonreciprocal directional dichroism spectra of $LiCoPO_4$, proving that this method can be used for a broad range of materials in the future.

Kokkuvõte
Magnetelektrilise nähtuse uurimine multiferroidides THz spektroskoopiaga

Valgus ja elektromagnetkiirgus üldisemalt mõjutab laengute ja magnetmomentide liikumist aines. Mõõtes valguse neeldumist ja peegeldusmist saame teadmisi aine ehitusest. Madala energiaga ergastustest saame teadmisi materjali elektriliste ja magnetiliste omaduste kohta. Tahkiste magnetilised omadused on määratud spinnide vabadusastmetega ning elektrilised omadused on määratud laengute vabadusastmetega.

Ferromagneetikus korrastuvad spinnid iseeneslikult ja ferroelektrikus korrastuvad laengud. Magnetelektrilistes multiferroidides eksisteerib magnetiline ja elektriline korrapära samaaegselt. Lisaks võib magnetelektrilistes multiferroidides esineda ka magnetelektriline vastasmõju, mille korral saab elektrivälja (magnetvälja) abil muuta magneetuvust (elektrilist polarisatsiooni). Magnetelektriline vastasmõju tekitab huvitavaid magnetelektrilisi nähtusi nagu näiteks vastassuunas liikuvate valguskiirte erinev neeldumine, mida kutsutakse suunadikroismiks. Sellistest materjalidest on võimalik luua näiteks optilist dioodi, mille valguse läbilaskvuse suunda saab lülitada elektri või magnetväljaga. Üks võimalik magnetelektrilise efekti rakendus oleks magnetelektriline mäluseade, kus saaks kasutada nii ferroelektrilise kui ka magnettakistuse nähtusel töötavate salvestustehnoloogiate positiivseid külgi: kiire ja madala voolutarbega lugemis- ja kirjutamisoperatsioonid ning mittevolatiilne püsimälu andmete hoiustamiseks. Paraku avalduvad magnetelektrilised nähtused enamasti toatemperatuurist oluliselt madalamatel temperatuuridel, mis teeb nende rakendamise ebapraktiliseks.

Magnetilised ergastused ehk spinn-lained on tavaliselt madala energiaga (mõned meV) ja nende uurimise peamine meetod on mitteelastne neutronhajumine, kus mõõdetakse neutronite hajumisel muutunud energiat ja impulssi. Neutronid hajuvad magnetmomentidel ning seega puudub neil tundlikkus spinnide poolt põhjustatud laengute liikumisele. Üks alternatiivne meetod neutronhajumisele on THz sageduspiirkonna infrapuna- ehk THz spektroskoopia, millel on parem energialahutus ning mis võimaldab uurida lisaks kollektiivsetele magnetilistele ergastustele ka lokaalseid spinnergastusi. Mõlemad meetodid annavad ergastuste resonantssageduse ja neeldumisjoonte kuju, mille kaudu on võimalik arvutada magnetiliste interaktsioonide tugevust. THz spektroskoopia meetodiga saab lisaks eelmainitule ka määrata, milline elektromagnetkiirguse komponent, magnetiline või elektriline, spinne ergastab, samas kui neutronhajumine on tundlik ainult ergastuse magnetilisele komponendile. Seega on ostsilleeruvate elektri ja magnetväljadega elektromagnetiline kiirgus ideaalne tööriist uurimaks magnetelektrilisi ergastusi multiferroidides.

Antud töö raames uuriti kolme multiferroidse materjali spinnergastusi kasutades THz spektroskoopiat kõrgetes magnetväljades. Mõõtmised magnetväljapiirkonnas 0-17 T sooritati Keemilise ja Bioloogilise Füüsika Instituudi terahertsspektroskoopia laboris Tallinnas. Mõõtmised suuremates magnetväljades sooritati Kõrgete Magnetväljade Laboris Hollandis, Nijmegenis. Mõõteobjektid jahutati madalale temperatuurile ja kõrge magnetvälja saavutamiseks kasutati Tallinnas ülijuhtivat magnetit ning Nijmegenis Bitteri elektromagnetit. Mõõtmised sooritati nii Faraday kui ka Voigt'i geomeetrias, et määrata valikureeglid kõigis võimalikes staatilise magnetvälja ja elektromagnetkiirguse suundades.

Spinnide poolt indutseeritud elektrilise polarisatsiooniga keerulised magnetilised olekud tekivad üldiselt üksteisega konkureerivate vahetusvastasmõjude tõttu. Tänu sellistele konkureerivatele vastasmõjudele vahelduvates kolmnurksetes ja kagome tasandites on swedenborgiit $CaBaCo_4O_7$ oma ferrimagneetilises faasis üks suurima spinnide poolt indutseeritud polarisatsiooniga ($\sim$1700 nC/cm^2) materjale üldse. Mõõtes THz neeldumisspektrite sõltuvust magnetvälja suunast *ab* tasandis näitasime, et kristallis on samaaegselt kolm struktuurset domeeni. Kasutades mitmeid mõõtmismetoodikaid, s.h. THz spektroskoopiat, näitasime, et igas domeenis olevat kompleksset spinnide korrastatust saab kirjeldada kolmnurkselt asetsevate bitetraeedsete *c* ahelatena, mis on ferrimagneetiliselt üksteisega seotud *ab* tasandis. Selle töö tulemus aitab luua uusi suure magnetmomendi ja elektrilise polarisatsiooniga funktsionaalseid materjale.

Meliliidis $Sr_2CoSi_2O_7$ mõõdeti spinnergastusi kuni 30 T magnetväljas nii magnetilise korrastatuse temperatuurist madalamatel kui ka kõrgematel temperatuuridel. Osadel spinnlainete moodidel on näha peaaegu täielikku ühesuunalist läbipaistvust temperatuuridel isegi kuni 100 K, kuigi $Sr_2CoSi_2O_7$ magnetilise korrastatuse temperatuur on kõigest T_N=7 K. Lisaks sellele mõnede moodide suunadikroism kõrgetes magnetväljades temperatuuri tõustes tugevneb. Suundikroismi suurenemine temperatuuri tõustes on multiferroidides harukordne, kuid seda seletab koobalti spinni magnetelektriline vastasmõju teda ümbritsevate laengutega koobalt-hapnik keemilisel sidemel, ehk spinni suunast sõltuv (anisotroopne) hübridisatsioonimehhanism. Selline ME vastasmõju ei sõltu naaberspinnide omavahelisest suunast ja seega ei ole magnetiline kaugkorrapära vajalik elektrilise polarisatsiooni tekkimiseks. Küll aga on vaja välist magnetvälja spinnide orienteerimiseks kristallvõre suhtes, et tekitada üle kogu kristalli nullist erinev keskmine elektriline polarisatsioon. Meie peamisi eksperimentaalseid avastusi - spinn-moodide sageduste temperatuurisõltuvus, nende intensiivsus, valikureeglid ning suunadikroismi suund - kirjeldab väga hea kokkulangevusega mudel nelja spinniga klastrist, mida oli võimalik täpselt diagonaliseerida.

Kolmandat kristalli - antiferromagneetilist oliviini struktuuriga $LiCoPO_4$ - uuriti ristväljas jahutamise metoodikaga, mille käigus rakendati kristalli antiferromagneetilisse faasi (T_N=21.7 K) jahutamise ajal tugevaid üksteisega risti asetsevaid elektri- ja magnetvälju. $LiCoPO_4$ kristallis on kaks antiferromagneetilist domeeni, milledel on vastasmärgiline ME vastuvõtlikkus. Kuna domeenidel on vastasmärgiline ME vastuvõtlikkus, siis on ka nende suunadikroism vastasmärgiline. Kristalli saab viia kontrollitult ühe-domeensesse olekusse kasutades sobivat elektri- ja magnetvälja kombinatsiooni jahutamise ajal. Pärast kirjeldatud viisil domeeni selekteerimist esineb kristallis suunadikroism ka peale väljade eemaldamist ning domeeni olekut on seega võimalik määrata mõõtes THz kiirguse neeldumise tugevust. Lisaks tavalistele magnetdipool spinn-laine ergastustele määrati ka elektromagnonid ja magnetelektrilised spinnresonantsid analüüsides spinnergastusi ja võrreldes neeldumisjoonte tugevusi erinevates antiferromagneetilistes domeenides.

Kokkuvõttes, oleme uurinud suurima spinn-indutseeritud elektrilise polarisatsiooniga $CaBaCo_4O_7$; $Sr_2CoSi_2O_7$ kristalli, millel on suunadikroism ka magnetiliselt korrastamata olekus, ning $LiCoPO_4$, millel on kaks elektri- ja magnetväljaga kontrollitavat ME seisundit. Näitasime, et terahertsspektroskoopia on kasulik meetod magnetelektriliste ergastuste uurimiseks ja saadaval informatsioonil on oluline väärtus ning ka rakendatavus.

Appendix 1

I

R. S. Fishman, S. Bordács, V. Kocsis, I. Kézsmárki, J. Viirok, U. Nagel, T. Rõõm, A. Puri, U. Zeitler, Y. Tokunaga, Y. Taguchi, and Y. Tokura. Competing exchange interactions in multiferroic and ferrimagnetic $CaBaCo_4O_7$. *Phys. Rev. B*, 95:024423, Jan 2017.

PHYSICAL REVIEW B **95**, 024423 (2017)

Competing exchange interactions in multiferroic and ferrimagnetic $CaBaCo_4O_7$

R. S. Fishman,[1] S. Bordács,[2] V. Kocsis,[2] I. Kézsmárki,[2] J. Viirok,[3] U. Nagel,[3] T. Rõõm,[3] A. Puri,[4] U. Zeitler,[4]
Y. Tokunaga,[5,6] Y. Taguchi,[5] and Y. Tokura[5,7]
[1]*Materials Science and Technology Division, Oak Ridge National Laboratory, Oak Ridge, Tennessee 37831, USA*
[2]*Department of Physics, Budapest University of Technology and Economics*
and MTA-BME Lendület Magneto-optical Spectroscopy Research Group, 1111 Budapest, Hungary
[3]*National Institute of Chemical Physics and Biophysics, Akadeemia tee 23, 12618 Tallinn, Estonia*
[4]*High Field Magnet Laboratory (HFML-EMFL), Radboud University Nijmegen, Toernooiveld 7, 6525 ED Nijmegen, The Netherlands*
[5]*RIKEN Center for Emergent Matter Science (CEMS), Wako, Saitama 351-0198, Japan*
[6]*Department of Advanced Materials Science, University of Tokyo, Kashiwa 277-8561, Japan*
[7]*Department of Applied Physics, University of Tokyo, Hongo, Tokyo 113-8656, Japan*
(Received 19 August 2016; revised manuscript received 19 December 2016; published 23 January 2017)

Competing exchange interactions can produce complex magnetic states together with spin-induced electric polarizations. With competing interactions on alternating triangular and kagome layers, the swedenborgite $CaBaCo_4O_7$ may have one of the largest measured spin-induced polarizations of $\sim 1700\ \mathrm{nC/cm^2}$ below its ferrimagnetic transition temperature at 70 K. Upon rotating our sample about $\mathbf{c} = [0,0,1]$ while the magnetic field is fixed along [1,0,0], the threefold splitting of the spin-wave frequencies indicates that our sample is hexagonally twinned. Magnetization measurements then suggest that roughly 20% of the sample is in a domain with the a axis along [1,0,0] and that 80% of the sample is in one of two other domains with the a axis along either $[-1/2,\sqrt{3}/2,0]$ or $[-1/2,-\sqrt{3}/2,0]$. Powder neutron-diffraction data, magnetization measurements, and terahertz (THz) absorption spectroscopy reveal that the complex spin order in each domain can be described as a triangular array of bitetrahedral c-axis chains ferrimagnetically coupled to each other in the ab plane. The electric-field dependence of bonds coupling those chains produces the large spin-induced polarization of $CaBaCo_4O_7$.

DOI: 10.1103/PhysRevB.95.024423

I. INTRODUCTION

Competing exchange interactions produce complex magnetic states with a wide range of interesting behavior found in spin glass [1], spin ice [2], and magnetic skyrmions [3]. In multiferroic materials, complex spin states can exibit a spin-induced electric polarization $\mathbf{P}$ due to either the spin current, p-d orbital hybridization, or magnetostriction [4,5]. Because the coupling between the electrical and magnetic properties in multiferroic materials is both scientifically and technologically important, the effects of competing exchange interactions have been investigated in a wide range of multiferroic materials such as $R\mathrm{MnO_3}$ (R is a rare-earth element) [6], $CoCr_2O_4$ [7], $CuCrO_2$ [8], $CuFeO_2$ [9], and $MnWO_4$ [10]. While the first four materials [6–9] are geometrically frustrated due to competing interactions on a triangular lattice, $MnWO_4$ [10] exhibits long-range competing interactions [11] on a highly-distorted monoclinic lattice.

Compounds in the "114" swedenborgite family [12] $R\mathrm{Ba}M_4\mathrm{O}_7$ ($M=$ Co or Fe) contain alternating triangular and kagome layers, both of which are geometrically frustrated when undistorted. The "114" cobaltites [13–15] were initially studied to find charge ordering among the Co^{2+} and Co^{3+} ions. An important member of this family, $YBaCo_4O_7$ exhibits antiferromagnetic ordering [16,17] below 110 K and diffuse scattering of neutrons [13,14] indicative of spin disorder below 60 K. The magnetic state between 110 and 60 K is stabilized by a structural transition [18] that relieves the geometric frustration. Both structural and magnetic transitions are quite sensitive to excess oxygen and no magnetic order [19,20] appears in $YBaCo_4O_{7+\delta}$ for $\delta \geqslant 0.12$. Other members of this family, $CaBaFe_4O_7$ and $YbBaCo_4O_7$ undergo structural transitions at 380 K and 175 K that stabilize antiferromagnetic states below 275 K and 80 K, respectively [21,22].

A particularly interesting "114" cobaltite, $CaBaCo_4O_7$ undergoes an orthorhombic distortion [23,24] that relieves the geometric magnetic frustration on both the kagome and triangular layers sketched in Fig. 1. Below the magnetic transition temperature $T_c = 70$ K, $CaBaCo_4O_7$ develops a very large spin-induced polarization $\sim 1700\ \mathrm{nC/cm^2}$ [25], second only to the conjectured [26] spin-induced polarization $\sim 3000\ \mathrm{nC/cm^2}$ of $BiFeO_3$. Also unusual, $CaBaCo_4O_7$ displays a substantial ferrimagnetic moment of about 0.9 μ_B per formula unit (f.u.) [27], which could allow magnetic control of the electric polarization. Although its ferroelectric transition is inaccessible and its permanent electric polarization is not switchable [28], applications of $CaBaCo_4O_7$ might utilize the large spin-induced polarization produced by a magnetic field just below T_c [25].

This paper examines the magnetic properties of $CaBaCo_4O_7$ based on a Heisenberg model with 12 nearest-neighbor interactions and associated anisotropies. The magnetic state of $CaBaCo_4O_7$ can be described as a triangular array of ferrimagnetically aligned, bitetrahedral c-axis chains with net moment along $\mathbf{b}$. Competing interactions within each chain produce a noncollinear spin state. The strong electric polarization of $CaBaCo_4O_7$ below T_c is induced by the displacement of oxygen atoms surrounding bonds that couple those chains.

This paper has six sections. Section II proposes a microscopic model for $CaBaCo_4O_7$. New magnetization and optical

©2017 American Physical Society

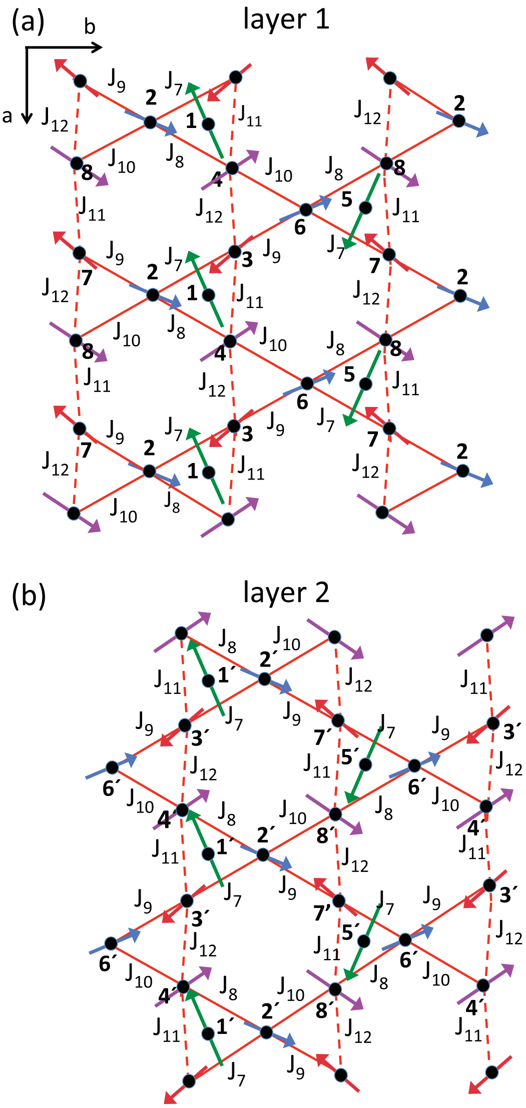

FIG. 1. (a) and (b) The predicted spin configuration for layers 1 and 2 in zero field. Spins 1 and 5 lie on a triangular layer above the first kagome layer in (a); spins 1′ and 5′ lie on a triangular layer above the second kagome layer in (b). Layers are arranged so that spins 1′ and 5′ lie directly above spins 1 and 5.

measurements are presented in Sec. III. Fitting results are discussed in Sec. IV. In Sec. V, we predict the spin-induced electric polarization. Section VI contains a conclusion.

II. MICROSCOPIC MODEL

Each magnetic unit cell of $\mathrm{CaBaCo_4O_7}$ contains 16 Co ions on two kagome and two triangular layers with orthorhombic lattice constants $a = 6.3$ Å, $b = 11.0$ Å, and $c = 10.2$ Å. Four

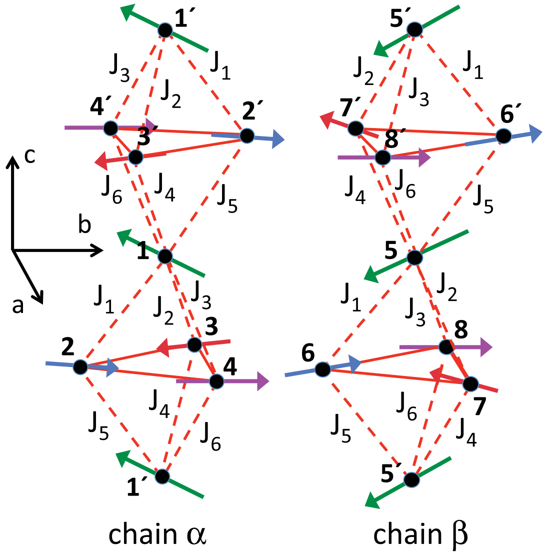

FIG. 2. A sideways view of the zero-field spin configuration showing bitetrahedral c-axis chains α and β.

crystallographically distinct Co ions have three different valences [23,29]. Triangular layers contain mixed-valent $\mathrm{Co^{3+}/Co^{2+}}\underline{L}$ ($\underline{L}$ is a ligand hole) spins 1, 5, 9, and 13 with moments $M_1 = 2.9\,\mu_\mathrm{B}$. Kagome layers contain $\mathrm{Co^{2+}}$ spins 2, 3, 6, 7, 10, 11, 14, and 15 with moments $M_2 = M_3 = 2\,\mu_\mathrm{B}$ and mixed-valent $\mathrm{Co^{3+}/Co^{2+}}\underline{L}$ spins 4, 8, 12, and 16 with $M_4 = 2.4\,\mu_\mathrm{B}$. Because adjacent kagome or triangular layers are related by symmetry, $\mathbf{S}_{i'} = \mathbf{S}_{i+8}$ on layer two is identical to $\mathbf{S}_i$ on layer one. With $\mathbf{S}_i = S_i(\cos\phi_i, \sin\phi_i, 0)$ constrained to the ab plane, the ferrimagnetic moment lies along $\mathbf{b}$ if $\phi_{i+4} = \pi - \phi_i$ ($i = 1,\ldots,4$).

The 12 different nearest-neighbor exchange couplings J_i are drawn in Figs. 1(a), 1(b), and 2. Six of these (J_1 through J_6) couple the kagome and triangular layers as shown in Fig. 2; the other six (J_7 through J_{12}) couple the spins within a kagome layer as shown in Figs. 1(a) and 1(b). The dominance of nearest-neighbor exchange over next-nearest-neighbor exchange [28] justifies setting the exchange interactions between spins on the triangular layers to zero. Our model also includes easy-plane anisotropies D, easy-axis anisotropies C within both kagome and triangular layers, and hexagonal anisotropy A on the triangular layers.

With magnetic field $\mathbf{B}$ along $\mathbf{m}$, the Hamiltonian is

$$\begin{aligned}\mathcal{H} = &-\sum_{\langle i,j\rangle} J_{ij}\mathbf{S}_i\cdot\mathbf{S}_j + D^{\rm tri}\sum_{i,\rm tri} {S_{ic}}^2 + D^{\rm kag}\sum_{i,\rm kag} {S_{ic}}^2\\ &- C^{\rm kag}\sum_{i,\rm kag}(\mathbf{o}_i\cdot\mathbf{S}_i)^2 - C^{\rm tri}\sum_{i,\rm tri}(\mathbf{n}_i\cdot\mathbf{S}_i)^2\\ &- A^{\rm tri}\,\mathrm{Re}\sum_{i,\rm tri}(S_{ia}+iS_{ib})^6 - g\mu_\mathrm{B}B\sum_i \mathbf{m}\cdot\mathbf{S}_i, \qquad (1)\end{aligned}$$

where $\mathbf{S}_i$ is a spin S operator on site i. For simplicity, we set $g = 2$ for all spins.

The easy-axis anisotropy terms proportional to $C^{\rm kag}$ and $C^{\rm tri}$ involve unit vectors $\mathbf{o}_i$ along the "bowtie" directions $\phi_i = \pi/2$ (spins 2 and 6), $5\pi/6$ (spins 3 and 8), and $7\pi/6$ (spins 4 and 7) for the kagome layers and $\mathbf{n}_i$ along the $\phi_i = \pi/6$ (spin 1) and $-\pi/6$ (spin 5) directions for the triangular layers. The hexagonal anisotropy on the triangular layers has expectation value

$$-A^{\rm tri} S_1{}^6 \sum_{i,\rm tri} \sin^6\theta_i \cos 6\phi_i .$$

All anisotropy terms may act to constrain the spins to the *ab* plane.

Spin amplitudes S_n are fixed at their observed values $M_n/2\mu_{\rm B}$ after performing a $1/S$ expansion about the classical limit. Alternatively, the spins S_n could all have been taken as 3/2 but with different g factors for different sets of spins. As discussed below, that would reduce the estimated exchange coupling J_{ij} by a factor of $4S_iS_j/9$.

Static properties are obtained by minimizing the classical energy $\langle\mathcal{H}\rangle$ (the zeroth-order term in the $1/S$ expansion) with respect to the 16 spin angles. The eigenvalues and eigenvectors of a 32×32 equations-of-motion matrix [30] produced by the second-order term in the this expansion give the optical mode frequencies and absorptions, respectively.

III. MAGNETIZATION AND OPTICAL MEASUREMENTS

Perhaps due to excess or deficient oxygen [31] or different domain populations (see below), previous magnetization measurements [23,27,32–34] on $\rm CaBaCo_4O_7$ are rather scattered. Consequently, new magnetization measurements were performed at 4 K on hexagonally twinned crystals with a common $\mathbf{c} = \mathbf{z} = [0,0,1]$ axis. In domain I, $\mathbf{a}$ lies along the laboratory direction $\mathbf{x} = [1,0,0]$ and $\mathbf{b}$ lies along $\mathbf{y} = [0,1,0]$, in domain II, $\mathbf{a} = [-1/2,\sqrt{3}/2,0]$ and $\mathbf{b} = [-\sqrt{3}/2,-1/2,0]$, and in domain III, $\mathbf{a} = [-1/2,-\sqrt{3}/2,0]$ and $\mathbf{b} = [\sqrt{3}/2,-1/2,0]$. If p_l are the domain populations, then the magnetizations M_x and M_y measured with fields along $\mathbf{x}$ and $\mathbf{y}$ only depend on p_1 and $p_2 + p_3 = 1 - p_1$. Of course, M_z measured with field along $\mathbf{z}$ is independent of p_l. Figure 3 indicates that all three magnetizations increase monotonically up to at least 32 T.

Previous optical measurements [35] at the ordering wave vector $\mathbf{Q}$ found two conventional spin-wave modes that couple to the ground state through the magnetization operator $\mathbf{M} = 2\mu_{\rm B}\sum_i \mathbf{S}_i$. These magnetic-resonance (MR) modes are degenerate in zero field with a frequency of 1.07 THz and split almost linearly with increasing field along $\mathbf{y}$, as shown in Fig. 4. For $\mathbf{m} = \mathbf{y}$, the MR modes are excited in two geometries: (*i*) with THz fields $\mathbf{E}_\omega||\mathbf{x}$ and $\mathbf{B}_\omega||\mathbf{z}$ and (*ii*) with $\mathbf{E}_\omega||\mathbf{z}$ and $\mathbf{B}_\omega||\mathbf{x}$. Those measurements also found an electromagnon (EM) that couples to the ground state through the polarization operator $\mathbf{P}$. The EM with zero-field frequency 1.41 THz is only excited in geometry *ii*.

Because the exchange couplings already break every degeneracy in the unit cell, the 16 predicted modes for a single domain are nondegenerate. Therefore the split MR modes must come from different domains. This was verified by measuring [36] the MR mode frequencies as a function of the rotation angle θ for field $\mathbf{B} = B(\cos\theta, \sin\theta, 0) = B(\mathbf{x}\cos\theta + \mathbf{y}\sin\theta)$ in the laboratory reference frame. In practice, this is accomplished by rotating the sample about $\mathbf{c}$ while keeping the field fixed along $\mathbf{x}$. As shown in Fig. 5 for 12 and 15 T, each hexagonal domain then contributes one MR branch with a period of π.

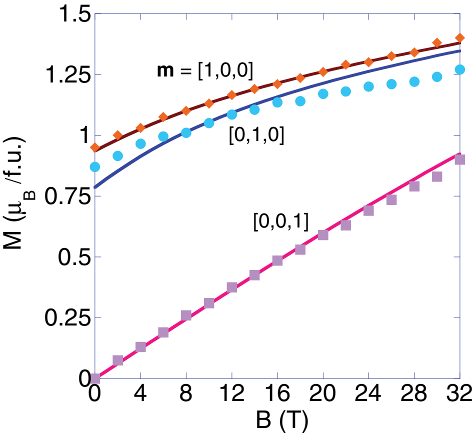

FIG. 3. The measured (symbols) and predicted (solid curves) magnetizations for field along [1,0,0], [0,1,0], or [0,0,1].

With field $\mathbf{B}_{\rm loc} = B(\cos\psi, \sin\psi, 0) = B(\mathbf{a}\cos\psi + \mathbf{b}\sin\psi)$ in the domain reference frame, the upper MR mode in Fig. 4 corresponds to the $\psi = \pi/2$ mode for domain I, while the lower MR mode corresponds to the degenerate $\psi = \pm\pi/6$ modes for domains II and III. Previously measured MR frequencies plotted in Fig. 4 at 12 T correspond to the diamond and triangular points in Fig. 5(b) at $\theta = \pi/2$. Cusps in the MR curves for each domain at $\psi = 0$ and π are caused by flipping the b component of the magnetization [see inset to Fig. 5(b)].

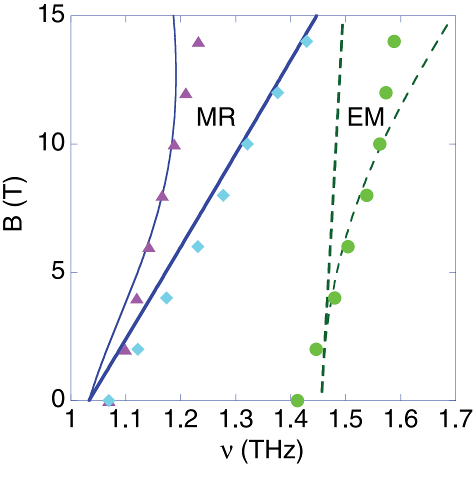

FIG. 4. The predicted MR (solid) and EM (dashed) modes for domain I (thick) and domains II and III (thin). Measured modes are indicated by symbols.

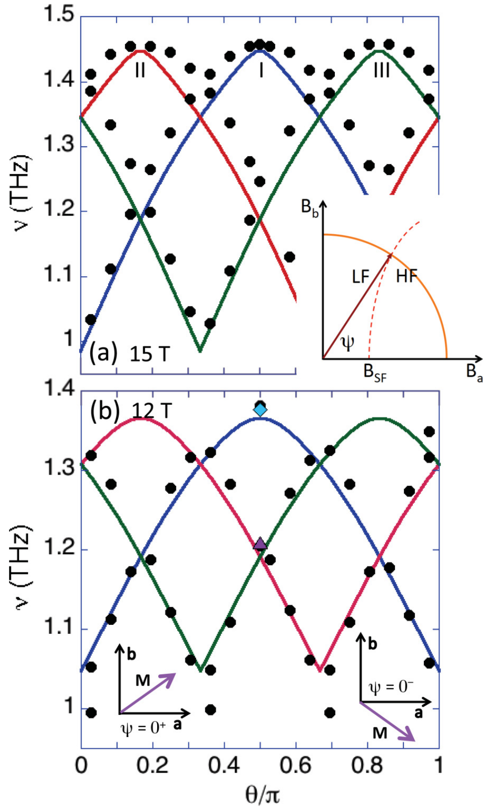

FIG. 5. The measured (solid circles) and predicted (blue, red, and green curves for domains I, II, and III, respectively) angular dependence of the MR mode frequencies for 12 and 15 T. The inset to (a) sketches the angular dependence of $\mathbf{B}_{\rm SF}$ (dashed curve), which separates low-field (LF) and high-field (HF) states. The inset to (b) shows the net magnetization of any domain for angles ψ on either side of 0. Flips of the b-axis spin at $\psi = 0$ and π produce cusps in the mode frequencies.

IV. FITTING RESULTS

Fits for the coupling parameters utilize the field dependence of **M**, the zero-field neutron powder-diffraction data [23], the field dependence of the MR and EM modes at $\theta = \pi/2$ [35], and the MR mode frequencies at $\theta = 0$ and $\pi/3$ for 7, 12, and 15 T. The resulting exchange and anisotropy constants are provided in Table I and the corresponding zero-field spin state is plotted in Figs. 1(a) and 1(b). In contrast to the previously proposed [23] spin state with zigzag chains in the *ab* plane containing spins 2, 3, 6, and 7, our spin state can be better described as an array of *c*-axis chains or connected bitetrahedra [16,37] containing spins {1,2,3,4} (chain α) or {5,6,7,8} (chain β) as sketched in Fig. 2. Chains are coupled by exchanges J_9, J_{10}, and J_{12} in the *ab* plane.

What explains the wide range of J_i values? An orthorhombic distortion [23,24] with $b/(a\sqrt{3}) - 1 \rightarrow 0.018$ as $T \rightarrow 0$ breaks the hexagonal symmetry of the *ab* plane and explains the difference between the pairs $\{J_1, J_2\}$, $\{J_8, J_{11}\}$, and $\{J_{10}, J_{12}\}$. The difference between couplings like $\{J_7, J_8\}$ is caused by charge ordering: whereas J_7 couples moments 2 and 3 with $M_2 = M_3$, J_8 couples moments 2 and 4 with $M_2 \neq M_4$. Charge ordering also explains the difference between the pairs $\{J_2, J_3\}$ and $\{J_9, J_{10}\}$. Although not demanded by symmetry, we set $J_1 = J_5$, $J_2 = J_4$, $J_3 = J_6$, and $J_{11} = J_{12}$ because the spin state and excitations at **Q** only depend on their averages [38].

Given other conditions, our fit chooses the spin state that matches the neutron powder-diffraction data [23] as closely as possible. At zero field, the predicted spin state has angles $\phi_1 = -0.83\pi$, $\phi_2 = 0.40\pi$, $\phi_3 = -0.23\pi$, and $\phi_4 = 0.62\pi$. Based exclusively on powder-diffraction data and symmetry constraints, the previously proposed spin state [23] had $\phi_1 = -0.24\pi$, $\phi_2 = \phi_3 = 0.67\pi$, and $\phi_4 = -0.44\pi$. In both cases, $\phi_{i+4} = \pi - \phi_i$ $(i = 1, \ldots, 4)$ so that the moment $\mathbf{M}_b$ lies along the *b* axis. As shown in Table II, our spin state does not satisfy the powder diffraction data quite as well as the earlier state, primarily because it underestimates the powder diffraction peak $I(112)$.

For the previous spin state, χ^2 is minimized by Lorentzian form factors with $Q_1/4\pi = 0.088$ Å^{-1}, $Q_2/4\pi = Q_3/4\pi = 0.095$ Å^{-1}, and $Q_4/4\pi = 0.088$ Å^{-1} for spins S_n. For the new spin state, $Q_1/4\pi = 0.052$ Å^{-1}, $Q_2/4\pi = Q_3/4\pi = 0.224$ Å^{-1}, and $Q_4/4\pi = 0.102$ Å^{-1}. Note that $Q_2/4\pi$ and $Q_3/4\pi$ are smaller than the scale $Q_0/4\pi \approx 0.3$ Å^{-1} measured by Khan and Erickson [39] for Co^{2+} in CoO.

Our results indicate that the exchange coupling $J_8 \approx 188$ meV between moments 2 (Co^{2+}, $S_2 = 1$) and 4 (Co^{3+}/Co$^{2+}\underline{L}$, $S_4 = 1.2$) is strongly ferromagnetic and larger in magnitude even than the 155 meV antiferromagnetic coupling found in the cuprate Nd$_2$CuO$_4$ [40]. The strength of this coupling might be explained by the double-exchange mediated hopping of ligand holes $\underline{L}$ [19] from site 4 to 2. Bear in mind, however, that the estimated exchange parameters would be significantly reduced if we had taken $S = 3/2$ for all Co spins. In particular, J_8 would then fall from 188 to 100 meV.

Except for J_{10}, the five largest exchange couplings $J_1 = J_5 \approx -92$ meV, $J_3 = J_6 \approx 41$ meV, and $J_8 \approx 188$ meV lie within connected bitetrahedral *c*-axis chains. Inside each chain, competing interactions between spins 1, 2, and 4 produce a noncollinear spin state.

TABLE I. Exchange and anisotropy parameters (mev).

	p_1	$J_1 = J_5$	$J_2 = J_4$	$J_3 = J_6$	J_7	J_8	J_9	J_{10}	$J_{11} = J_{12}$	$D^{\rm kag}$	$D^{\rm tri}$	$C^{\rm kag}$	$C^{\rm tri}$	$S_1{}^4 A^{\rm tri}$
	0.185	−91.5	−10.8	41.4	−29.9	187.8	7.9	108.0	−6.7	−0.67	−1.24	3.70	0.77	0.0064
error	±0.071	±3.6	±0.5	±0.7	±1.9	±7.5	±0.1	±4.5	±0.1	±0.06	±0.03	±0.15	±0.09	±0.0004

TABLE II. Ratios of powder-diffraction peak intensities.

	$I(002)/I(101)$	$I(012)/I(101)$	$I(111)/I(101)$	$I(112)/I(101)$	$I(121)/I(101)$	$I(122)/I(101)$	$M_b(\mu_B/\text{f.u.})$	χ^2
experimental [23]	0.344	0.326	0.322	0.477	0.262	0.404		
previous [23]	0.286	0.414	0.384	0.411	0.232	0.427	0.88	0.021
current	0.360	0.380	0.378	0.286	0.313	0.449	1.33	0.047

Although occupying a triangular lattice, chains α and β are magnetically ordered with moments $\mathbf{M}^{\text{ch}} = (\pm 1.18, 1.33, 0)\mu_B$/f.u.. These chains are primarily coupled by the strongly ferromagnetic interaction $J_{10} \approx 108$ meV between nearly parallel spins $\{4,6\}$ ($\phi_4 = 0.62\pi, \phi_6 = 0.60\pi$) and $\{2,8\}$ ($\phi_2 = 0.40\pi$, $\phi_8 = 0.38\pi$). Above $T_c = 70$ K, the short-range order within each chain may be responsible for the large, negative Curie-Weiss temperature $\Theta_{\text{CW}} \approx -1720$ [27] or -890 K [32], the larger than expected Curie constant [27], and the susceptibility anomaly [32] at 360 K suggestive of short-range magnetic order far above T_c.

Comparison between the theoretical and experimental results for the magnetization in Fig. 3 suggests that roughly 20% of the sample is in domain I. Different domain populations or even orthorhombic twinning in other samples may explain the discrepancies between the reported magnetization measurements [23,27,32–34].

Easy-axis anisotropies A and C favor ferrimagnetic alignment along **b** rather than **a**. The spin-flop (SF) field required to flip the spins towards the **a** direction must increase as the field along **b** increases [41]. As shown in the inset to Fig. 5(a), $B_{\text{SF}}(\psi)$ then increases with ψ. If $B_{\text{SF}}(\psi = 0) < 15$ T, then the MR spectrum for 15 T would show a discontinuity at the transition from a low-field (LF) to a high-field (HF) state below some critical value of ψ. Since the MR mode frequencies in Fig. 5(a) do not exhibit any discontinuities as a function of ψ, we conclude that $B_{\text{SF}}(\psi = 0)$ exceeds 15 T and probably, based on the smooth dependence of the magnetizations on field, exceeds 32 T as well. The apparent small size of B_{SF} [25,42] must reflect the net magnetization of all three domains.

Predicted modes below 5 THz are plotted in Fig. 4. The Goldstone modes for all three domains are lifted by in-plane anisotropies to become the MR modes with zero-field frequencies of 1.07 THz. As remarked earlier, the lower MR mode comes from domains II and III while the upper MR mode comes from domain I. Below 3.5 THz, one EM mode is produced in domain I and another in domains II and III. The degenerate EM modes from domains II and III dominate the optical absorption. The predicted field dependence of the upper MR mode is quite close to the observed dependence. However, the predicted curvatures of the lower MR and the EM modes, both from domains II and III, is not observed.

V. SPIN-INDUCED ELECTRIC POLARIZATION

Below the ferrimagnetic transition, $\text{CaBaCo}_4\text{O}_7$ is reported [25] to develop a very large spin-induced polarization $\sim$1700 nC/cm^2, which is surpassed in type-I multiferroics only by the conjectured [26] spin-induced polarization $\sim$3000 nC/cm^2 of BiFeO_3. Other measurements indicate that the spin-induced polarization of $\text{CaBaCo}_4\text{O}_7$ ranges from 320 nC/cm^2 [33] to 900 nC/cm^2 [43].

The electric-field dependence of any interaction term in the spin Hamiltonian $\mathcal{H}$ can induce an electric polarization below T_c. However, the electric-field dependence of the easy-plane anisotropy D cannot explain the spin-induced polarization along **c** because the expectation value of $P_i = \kappa S_{ic}{}^2$ with $\kappa = -\partial D/\partial E_c$ would vanish in zero magnetic field when all the spins lie in the ab plane. Easy-axis anisotropy A or C in the ab plane could produce a spin-induced electric polarization perpendicular to **c**. But the EM mode would then become observable for a THz electric field in the ab plane, contrary to measurements.

As conjectured previously [25], the spin-induced polarization in $\text{CaBaCo}_4\text{O}_7$ must then be generated by the dependence of the exchange interactions J_{ij} on an electric field, called magnetostriction. Coupling constant $\lambda_{ij} = \partial J_{ij}/\partial E_c$ for bond $\{i,j\}$ is associated with a spin-induced polarization [44] per site of $P_c^{ij} = \lambda_{ij}\,\mathbf{S}_i \cdot \mathbf{S}_j/4$, which accounts for the four equivalent bonds per unit cell. Expanding in the electric field E_c yields an interaction term $-E_c\,\lambda_{ij}\,\mathbf{S}_i \cdot \mathbf{S}_j$, linear in the electric field and quadratic in the spin operators.

Taking $|0\rangle$ as the ground state and $|n\rangle$ as the excited spin-wave state, the MR matrix element $\langle n|M_a|0\rangle$ mixes with the EM matrix element $\langle n|P_c^{ij}|0\rangle$ for domains II and III but not for domain I. Therefore our model can explain the strong asymmetry [45] $\sim$Re$\{\langle n|\mathbf{M}\cdot\mathbf{B}_\omega|0\rangle\langle 0|\mathbf{P}\cdot\mathbf{E}_\omega|n\rangle\}$ in the absorption of counter-propagating light waves [35] for the lower observed MR mode in geometry ii with $\mathbf{E}_\omega || \mathbf{c}$. However, it cannot explain the observed asymmetry of this mode in geometry i with $\mathbf{E}_\omega \perp \mathbf{c}$ if only $\langle 0|P_c|n\rangle$ is significant.

How can we estimate the coupling constants λ_{ij} and the spin-induced electric polarization? The optical absorption of any mode in domain l is proportional to p_l. So at nonzero field, the EM absorption is proportional to $p_2 + p_3 = 1 - p_1$ while the upper MR mode absorption is proportional to p_1. At zero field, all domains have the same mode spectrum so that both the MR and EM mode absorptions are proportional to $p_1 + p_2 + p_3 = 1$. Experimentally, the ratio r of the absorption of the EM mode to the absorption of the upper MR mode rises from $r = 7.5$ at 0 T to $r = 35$ at 10 T. This growth is explained by the $B > 0$ ratio $(1 - p_1)/p_1 = 4.4$.

At both 0 and 10 T, the only sets of bonds that generate spin-induced polarizations of the right magnitude are $\{2,7\}$ and $\{3,4\}$. Each of those bonds couples adjacent c-axis chains through pairs of spins that are almost antiparallel. From the relative absorptions r at 0 or 10 T, we estimate that $\langle P_c^{27}\rangle \approx 2350$ or 2920 nC/cm^2 and $\langle P_c^{34}\rangle \approx 2110$ or 2570 nC/cm^2. Results for both sets of bonds are consistent with the recently observed [25] polarization of 1700 nC/cm^2. By contrast, density-functional theory [28] predicts that the spin-induced polarization along **c** is 460 nC/cm^2. The spin-induced polarization should remain fairly constant with applied magnetic field, decreasing by about 1% for a 10 T field along **b**.

VI. CONCLUSION

We have presented a nearly complete solution for the magnetization, spin state, and mode frequencies of the swedenborgite $\mathrm{CaBaCo_4O_7}$. An orthorhombic distortion above T_c partially relieves the geometric frustration on the kagome and triangular layers and allows ferrimagnetism and ferroelectricity to coexist below T_c. Although occupying a triangular lattice, bitetrahedral c-axis chains are ferrimagnetically ordered in the ab plane. Competing interactions within each chain produce noncollinear spin states. Sets of bonds coupling those chains are responsible for the large spin-induced polarization of $\mathrm{CaBaCo_4O_7}$.

Despite its fixed permanent electric polarization, this swedenborgite may yet have important technological applications utilizing the large changes [25] in the spin-induced polarization when a modest magnetic field below 1 T is applied along **b** in the vicinity of T_c. A big jump in the polarization should also be produced just below T_c by rotating a fixed magnetic field about the c axis. Above all, our work illuminates a pathway to develop other functional materials with sizable magnetic moments and electrical polarizations.

ACKNOWLEDGMENTS

Research sponsored by the U.S. Department of Energy, Office of Science, Basic Energy Sciences, Materials Sciences and Engineering Division (RF), by the Hungarian Research Funds OTKA K 108918, OTKA PD 111756, and Bolyai 00565/14/11 (SB, VK, and IK), by the institutional research funding IUT23-3 of the Estonian Ministry of Education and Research and the European Regional Development Fund project TK134 (TR and UN), and by the Funding Program for World-Leading Innovative R&D on Science and Technology (FIRST Program) (YT, YT, and YT). We also acknowledge the support of the HFML-RU/FOM, member of the European Magnetic Field Laboratory (EMFL).

This manuscript has been authored by UT-Battelle, LLC under Contract No. DE-AC05-00OR22725 with the U.S. Department of Energy. The United States Government retains and the publisher, by accepting the article for publication, acknowledges that the United States Government retains a nonexclusive, paid-up, irrevocable, world-wide license to publish or reproduce the published form of this manuscript, or allow others to do so, for United States Government purposes. The Department of Energy will provide public access to these results of federally sponsored research in accordance with the DOE Public Access Plan (http://energy.gov/downloads/doe-public-access-plan).

---

[1] K. Binder and A. P. Young, Rev. Mod. Phys. **58**, 801 (1986).
[2] M. J. Harris, S. T. Bramwell, D. F. McMorrow, T. Zeiske, and K. W. Godfrey, Phys. Rev. Lett. **79**, 2554 (1997).
[3] S. Mühlbauer, B. Binz, F. Jonietz, C. Pfleiderer, A. Rosch, A. Neubauer, R. Georgii, and P. Böni, Science **323**, 915 (2009).
[4] D. I. Khomskii, J. Magn. Magn. Mater. **306**, 1 (2006).
[5] S.-W. Cheong and M. Mostovoy, Nat. Mat. **6**, 13 (2007).
[6] A. B. Sushkov, R. V. Aguilar, S. Park, S.-W. Cheong, and H. D. Drew, Phys. Rev. Lett. **98**, 027202 (2007).
[7] Y. Yamasaki, S. Miyasaka, Y. Kaneko, J.-P. He, T. Arima, and Y. Tokura, Phys. Rev. Lett. **96**, 207204 (2006).
[8] M. Soda, K. Kimura, T. Kimura, and K. Hirota, Phys. Rev. B **81**, 100406 (2010).
[9] S. Seki, N. Kida, S. Kumakura, R. Shimano, and Y. Tokura, Phys. Rev. Lett. **105**, 097207 (2010).
[10] K. Taniguchi, N. Abe, S. Ohtani, and T. Arima, Phys. Rev. Lett. **102**, 147201 (2009).
[11] F. Ye, R. S. Fishman, J. A. Fernandez-Baca, A. A. Podlesnyak, G. Ehlers, H. A. Mook, Y.-Q. Wang, B. Lorenz, and C. W. Chu, Phys. Rev. B **83**, 140401 (2011).
[12] B. Raveau, V. Caignaert, V. Pralong, and A. Maignan, Z. Anorg. Allg. C **635**, 1869 (2009).
[13] M. Valldor and M. Andersson, Sol. St. Sci. **4**, 923 (2002); M. Valldor, *ibid.* **6**, 251 (2004).
[14] E. V. Tsipis, D. D. Khalyavin, S. V. Shiryaev, K. S. Redkina, and P. Núñez, Mat. Chem. Phys. **92**, 33 (2005); E. V. Tsipis, V. V. Kharton, J. R. Frade, and P. Núñez, J. Sol. St. Electrochem. **9**, 547 (2005).
[15] G. L. Bychkov, S. N. Barilo, S. V. Shiryaev, D. V. Sheptyakov, S. N. Ustinovich, A. Podlesnyak, M. Baran, R. Szymczak, and A. Furrer, J. Cryst. Growth **275**, e813 (2005).
[16] L. C. Chapon, P. G. Radaelli, H. Zheng, and J. F. Mitchell, Phys. Rev. B **74**, 172401 (2006).
[17] D. D. Khalyavin, P. Manuel, B. Ouladdiaf, A. Huq, P. W. Stephens, H. Zheng, J. F. Mitchell, and L. C. Chapon, Phys. Rev. B **83**, 094412 (2011).
[18] A. K. Bera, S. M. Yusuf, and S. Banerjee, Sol. St. Sci. **16**, 57 (2013).
[19] A. Maignan, V. Caignaert, D. Pelloquin, S. Hébert, V. Pralong, J. Hejtmanek, and D. Khomskii, Phys. Rev. B **74**, 165110 (2006).
[20] S. Avci, O. Chmaissem, H. Zheng, A. Huq, P. Manuel, and J. F. Mitchell, Chem. Mat. **25**, 4188 (2013).
[21] A. Huq, J. F. Mitchell, H. Zheng, L. C. Chapon, P. G. Radaelli, K. S. Knight, and P. W. Stephens, J. Sol. St. Chem. **179**, 1136 (2006).
[22] V. Kocsis, Y. Tokunaga, S. Bordács, M. Kriener, A. Puri, U. Zeitler, Y. Taguchi, Y. Tokura, and I. Kézsmárki, Phys. Rev. B **93**, 014444 (2016).
[23] V. Caignaert, V. Pralong, V. Hardy, C. Ritter, and B. Raveau, Phys. Rev. B **81**, 094417 (2010).
[24] S. N. Panja, J. Kumar, S. Dengre, and S. Nair, J. Phys.: Cond. Mat. **16**, 9209 (2016).
[25] V. Caignaert, A. Maignan, K. Singh, Ch. Simon, V. Pralong, B. Raveau, J. F. Mitchell, H. Zheng, A. Huq, and L. C. Chapon, Phys. Rev. B **88**, 174403 (2013).
[26] J.-H. Lee and R. S. Fishman, Phys. Rev. Lett. **115**, 207203 (2015).
[27] V. Caignaert, V. Pralong, A. Maignon, and B. Raveau, Sol. St. Comm. **149**, 453 (2009).
[28] R. D. Johnson, K. Cao, F. Giustino, and P. G. Radaelli, Phys. Rev. B **90**, 045129 (2014).

[29] S. Chatterjee and T. Saha-Dasgupta, Phys. Rev. B **84**, 085116 (2011).

[30] R. S. Fishman, J. T. Haraldsen, N. Furukawa, and S. Miyahara, Phys. Rev. B **87**, 134416 (2013).

[31] Md. M. Seikh, V. Caignaert, V. Pralong, and B. Raveau, J. Phys. Chem. Sol. **75**, 79 (2014).

[32] Z. Qu, L. Ling, L. Zhang, and Y. Zhang, Sol. St. Comm. **151**, 917 (2011).

[33] H. Iwamoto, M. Ehara, M. Akaki, and H. Kuwahara, J. Phys.: Conf. Ser. **400**, 032031 (2012).

[34] Md. Motin Seikh, T. Sarkar, V. Pralong, V. Caignaert, and B. Raveau, Phys. Rev. B **86**, 184403 (2012).

[35] S. Bordács, V. Kocsis, Y. Tokunaga, U. Nagel, T. Rõõm, Y. Takahashi, Y. Taguchi, and Y. Tokura, Phys. Rev. B **92**, 214441 (2015).

[36] The THz spectra of $CaBaCo_4O_7$ were measured at 2.5 K with linear light polarization using Fourier-transform spectroscopy [35]. The reference spectrum was taken in zero field.

[37] M. Valldor, J. Phys.: Cond. Mat. **16**, 9209 (2004).

[38] Spin excitations away from $\mathbf{q} = \mathbf{Q}$ depend separately on these exchange constants. The stability of the coplanar ground state requires that each pair of exchange constants be sufficiently close to one another.

[39] D. C. Khan and R. A. Erickson, Phys. Rev. B **1**, 2243 (1970).

[40] P. Bourges, H. Casalta, A. S. Ivanov, and D. Petitgrand, Phys. Rev. Lett. **79**, 4906 (1997).

[41] While the coplanar LF spin state has a lower energy than the HF state below 32 T, it becomes locally unstable to a buckled state with spins canted out of the *ab* plane between 16 and 32 T for field along **a**. Based on the smooth dependence of the magnetizations on field, the transition from the coplanar to the buckled state must be second order.

[42] V. Pralong, V. Caignert, T. Sarkar, O. I. Lebedev, V. Duffort, and B. Raveau, J. Sol. St. Chem. **184**, 2588 (2011).

[43] V. Kocsis, S. Bordács, and I. Kézsmárki (unpublished).

[44] Based on the symmetry of adjacent layers, it is easy to show that the polarization operator $\mathbf{P}^{12}$ associated with bond $\{1,2\}$ has components

$$\begin{aligned} P_a^{12} &\propto C_{12} - C_{56} - C_{1'2'} + C_{5'6'}, \\ P_b^{12} &\propto C_{12} + C_{56} - C_{1'2'} - C_{5'6'}, \\ P_c^{12} &\propto C_{12} + C_{56} + C_{1'2'} + C_{5'6'}, \end{aligned}$$

where $C_{ij} = \mathbf{S}_i \cdot \mathbf{S}_j$. Similar relations hold for other bonds. Only the c component P_c^{ij} can produce a static polarization but all three components may contribute to the off-diagonal polarization matrix elements $\langle 0|P_\alpha^{ij}|n\rangle$ $(n \neq 0)$.

[45] S. Miyahara and N. Furukawa, J. Phys. Soc. Japan **80**, 073708 (2011).

Appendix 2

II

J. Viirok, U. Nagel, T. Rõõm, D. G. Farkas, P. Balla, D. Szaller, V. Kocsis, Y. Tokunaga, Y. Taguchi, Y. Tokura, B. Bernáth, D. L. Kamenskyi, I. Kézsmárki, S. Bordács, and K. Penc. Directional dichroism in the paramagnetic state of multiferroics: A case study of infrared light absorption in $Sr_2CoSi_2O_7$ at high temperatures. *Phys. Rev. B*, 99:014410, Jan 2019.

PHYSICAL REVIEW B **99**, 014410 (2019)

Directional dichroism in the paramagnetic state of multiferroics: A case study of infrared light absorption in $Sr_2CoSi_2O_7$ at high temperatures

J. Viirok,[1] U. Nagel,[1] T. Rõõm,[1] D. G. Farkas,[2] P. Balla,[2,3] D. Szaller,[2,4] V. Kocsis,[2,5] Y. Tokunaga,[5,6] Y. Taguchi,[5]
Y. Tokura,[5,7] B. Bernáth,[8] D. L. Kamenskyi,[8] I. Kézsmárki,[2,9] S. Bordács,[2,10] and K. Penc[2,3]
[1]*National Institute of Chemical Physics and Biophysics, Akadeemia tee 23, 12618 Tallinn, Estonia*
[2]*Department of Physics, Budapest University of Technology and Economics and MTA-BME Lendület Magneto-optical Spectroscopy Research Group, 1111 Budapest, Hungary*
[3]*Institute for Solid State Physics and Optics, Wigner Research Centre for Physics, Hungarian Academy of Sciences, PO Box. 49, H-1525 Budapest, Hungary*
[4]*Institute of Solid State Physics, Vienna University of Technology, 1040 Vienna, Austria*
[5]*RIKEN Center for Emergent Matter Science (CEMS), Wako, Saitama 351-0198, Japan*
[6]*Department of Advanced Materials Science, University of Tokyo, Kashiwa, Chiba 277-8561, Japan*
[7]*Department of Applied Physics, University of Tokyo, Bunkyo, Tokyo 113-8656, Japan*
[8]*High Field Magnet Laboratory (HFML-EMFL), Radboud University, Toernooiveld 7, 6525 ED Nijmegen, The Netherlands*
[9]*Experimental Physics V, Center for Electronic Correlations and Magnetism, Institute of Physics, University of Augsburg, 86159 Augsburg, Germany*
[10]*Hungarian Academy of Sciences, Premium Postdoctor Program, 1051 Budapest, Hungary*

(Received 28 September 2018; published 9 January 2019)

The coexisting magnetic and ferroelectric orders in multiferroic materials give rise to a handful of novel magnetoelectric phenomena, such as the absorption difference for the opposite propagation directions of light called the nonreciprocal directional dichroism (NDD). Usually, these effects are restricted to low temperature, where the multiferroic phase develops. In this paper, we report the observation of NDD in the paramagnetic phase of $Sr_2CoSi_2O_7$ up to temperatures more than 10 times higher than its Néel temperature (7 K) and in fields up to 30 T. The magnetically induced polarization and NDD in the disordered paramagnetic phase is readily explained by the single-ion spin-dependent hybridization mechanism, which does not necessitate correlation effects between magnetic ions. The $Sr_2CoSi_2O_7$ provides an ideal system for a theoretical case study, demonstrating the concept of magnetoelectric spin excitations in a paramagnet via analytical as well as numerical approaches. We applied exact diagonalization of a spin cluster to map out the temperature and field dependence of the spin excitations, as well as symmetry arguments of the single ion and lattice problem to get the spectrum and selection rules.

DOI: 10.1103/PhysRevB.99.014410

I. INTRODUCTION

Nonreciprocal directional dichroism (NDD) is the property of a material to have different absorption coefficients for light propagation directions $\pm\mathbf{k}$ along and opposite to a given direction in the crystal [1]. Although NDD was observed a long time ago for the exciton transitions of the polar semiconductor CdS [2], it was recognized as a general magneto-optical phenomenon of noncentrosymmetric materials only by the seminal works of Rikken and his co-workers [3,4]. The two basic cases of NDD were identified as the *magnetochiral dichroism* [3] (MChD) and the *toroidal dichroism*. In the case of MChD the absorption coefficient is different for light propagation along and opposite the magnetization of a chiral magnet $\mathbf{k} \parallel \mathbf{M}$ [4]. In the case of toroidal dichroism NDD appears for propagation along and opposite $\mathbf{k} \parallel \mathbf{P} \times \mathbf{M}$, where $\mathbf{P}$ is the ferroelectric polarization of the material. In general, NDD can be finite only when both the spatial inversion and time-reversal symmetries are broken, as these symmetry operations interconnect the light beams propagating in opposite directions. Following the same principle, a recent study rigorously classified the magnetic point groups compatible with NDD [5]. It predicted that beside magnetochiral and toroidal dichroism NDD can arise in previously unclassified cases, which cannot be classified by a static vector quantity, such as the magnetization or the toroidal moment.

Magnetoelectric (ME) multiferroics with coexisting ferroelectric and magnetic orders naturally have the low-symmetry ground states exhibiting magnetochiral or toroidal dichroism, and indeed gigantic NDD was found in their collective excitations, typically in the GHz-THz range [6–12]. At these low frequencies, where the electromagnetic radiation is uniform on the scale of the magnetic unit cell, NDD can solely originate from the coupled dynamics of the magnetization and the electric polarization, the dynamic ME effect. When light beams travel in a ME material, for a beam propagating in one direction the oscillating magnetization generated by the electric field of the light can enhance the conventional magnetization component, induced by the magnetic field of light, whereas these two terms interfere destructively for the counterpropagating beam since the relative phase of the electric and magnetic fields of light changes by π when reversing the propagation direction. The direct connection

2469-9950/2019/99(1)/014410(14)

©2019 American Physical Society

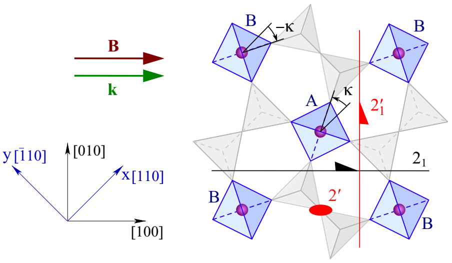

FIG. 1. Schematic illustration of the $Sr_2CoSi_2O_7$ crystal structure, space group $P\bar{4}2_1m$, and the coordinate axes $\mathbf{x} \parallel [110]$ and $\mathbf{y} \parallel [\bar{1}10]$. Purple circles denote the $S = \frac{3}{2}$ Co^{2+} ions in the centers of the O^{2-} tetrahedra (shown in blue). The compound is built up by layers of CoO_4 tetrahedra and Si_2O_7 units (gray), which are separated by Sr ions. For clarity, only a single layer is shown. $\pm\kappa$ is the rotation angle of tetrahedra about the [001] axis away from [110]. A and B denote the two types of tetrahedra with $+\kappa$ and $-\kappa$ tilt. In the experiment, the THz light propagates along the direction of the magnetic field $\mathbf{k} \parallel \mathbf{B} \parallel [100]$. The magnetic field breaks the time-reversal symmetry and for this field direction the remaining unitary symmetry operation is the 2_1 screw axis (black half-arrow). The antiunitary operations including the time reversal are the $2'$ twofold rotation about the [001] axis (red ellipse) and the $2'_1$ screw axis (red half arrow).

between the NDD and the ME effect allows the calculation of the direct current (dc) ME coefficient from the NDD spectrum using the sum rule [13]. Thus, the spectroscopic information about the ME resonances can promote the synthesis of new multiferroics with large ME coefficient.

One-way transparency is an extreme case of gigantic NDD when the light is absorbed only in one direction but not for the opposite propagation direction. Since no physical law prohibits the one-way transparency, an efficient one-way light guide can be realized. Furthermore, the transparent direction can be switched with applied magnetic [6] and possibly with electric field [14,15]. Some of the multiferroics, e.g., melilites $Ba_2CoGe_2O_7$, $Ca_2CoSi_2O_7$, and $Sr_2CoSi_2O_7$, are not far from the ideal realization of one-way transparency [10]. In principle, these materials can find applications in photonics as diodes for THz radiation or directional light switches [12]. However, the multiferroic order possessing large NDD usually develops well below room temperature in the known materials, with the exception of the room-temperature multiferroic $BiFeO_3$ [12], rendering their use in device applications impractical.

Here, we suggest an alternative way of achieving NDD by demonstrating that the spin excitations in $Sr_2CoSi_2O_7$ show NDD well above the antiferromagnetic ordering temperature $T_N = 7$ K. The crystal structure of melilites (see Fig. 1) lacks the inversion symmetry. Applying magnetic field, the time-reversal symmetry will be broken in the paramagnetic phase and the necessary conditions for NDD are then fulfilled. Akaki *et al.* [16,17] demonstrated that in $Sr_2CoSi_2O_7$ the dc ME effect persists in the paramagnetic regime, where the field-induced polarization scales with the square of the magnetization. Since the dc ME susceptibility is related to NDD by the ME sum rule [13], we expect that NDD appears also in the paramagnetic phase of $Sr_2CoSi_2O_7$.

In this paper, motivated by the discovery of the high-temperature dc ME effect in $Sr_2CoSi_2O_7$, we study the NDD in the paramagnetic phase. We measured the THz absorption spectra in magnetic fields up to 30 T over a broad range of temperatures below and well above T_N. The magnetic field was applied along the [100] direction, which induces magnetization parallel to the field. The point group of the $Sr_2CoSi_2O_7$, $\bar{4}2m1'$ in the paramagnetic state, is then reduced to the magnetic point group $22'2'$ [7]. In this chiral symmetry, MChD is expected to emerge for light propagation along the magnetic field, i.e., in the Faraday geometry. Indeed, our experiments show that the spectra are markedly different in positive and negative magnetic field, which is the hallmark of MChD. Using exact diagonalization we reproduced the magnetic field and temperature dependence of the MChD signal. To interpret the numerical results, a single-site analytic model was developed which shows that the finite NDD arises if all three are present: magnetic field, spin anisotropy, and ME coupling.

Recently, Yu *et al.* studied spin excitations of a polar ferrimagnet $FeZnMo_3O_8$ in Ref. [18]. They demonstrated that the toroidal dichroism can be realized in the paramagnetic phase when the light propagates along the cross product of the built-in polarization and the external magnetic-field-induced magnetization $\mathbf{k} \parallel \mathbf{P} \times \mathbf{M}$. In contrast, here we study MChD, a different form of NDD, and develop microscopic spin models to understand NDD in the paramagnetic phase.

The paper is organized as follows. After description of the experimental methods in Sec. II, the experimental results are presented in Sec. III. To understand the observed spin excitations and NDD, first, a spin Hamiltonian and spin-induced polarization of $Sr_2CoSi_2O_7$ are introduced in Sec. IV. The Hamiltonian is numerically diagonalized for a small cluster and the eigenstates are used to calculate magnetic and ME susceptibilities in Sec. V. Second, using a single-ion model in Sec. VI the results of the exact diagonalization are interpreted. Third, the selection rules found for the single-ion case are generalized for the lattice model in Sec. VII. In addition, in this section the effects of the exchange interaction in leading order of perturbation theory are analyzed. Finally, the main experimental and theoretical results are summarized in Sec. VIII.

II. EXPERIMENTAL METHODS

The $Sr_2CoSi_2O_7$ crystals were grown by the floating-zone method. First, $SrCO_3$, Co_3O_4, and dehydrated SiO_2 were mixed in stoichiometric amount and sintered for 120 h at 1200°C in air with one intermediate regrinding. The resulting product was pressed into a rod shape and resintered for 60 h under the same conditions as before. The polycrystalline rod was melted into a single-crystal ingot in a halogen-incandescent lamp floating-zone apparatus (SC-N35HD, NEC).

Samples for THz spectroscopy were disk-shaped single crystals with a diameter of 4 mm and thicknesses of $d = 0.2$ and 0.5 mm in the [100] direction. The external magnetic field $\mathbf{B}$ and the light propagation $\mathbf{k}$ were both in the [100] direction $\mathbf{k} \parallel \mathbf{B} \parallel [100]$. The THz radiation was polarized by a wire-grid polarizer deposited on a dielectric film placed a few millimeters away from the sample in the incident light beam. The transmitted intensity was measured with a Martin-Puplett–type interferometer (SPS200, Sciencetech, Inc., Ontario, Canada) and 0.3 K composite silicon bolometer (Infrared Laboratories) in magnetic fields up to 17 T for both positive and negative fields in the temperature range between 3 and 100 K. Measurements above 17 T were performed with a Genzel-type interferometer (Bruker 113v) and a 1.6 K composite Si bolometer (Infrared Laboratories).

The absorption coefficient $\alpha^{\pm}$ for magnetic fields $\pm B$ was calculated as

$$\alpha^{\pm} = -\frac{1}{d} \ln \frac{I(\pm B, T)}{I(0\,\mathrm{T}, T_{\mathrm{ref}})}, \tag{1}$$

where $I(\pm B, T)$ is the transmitted intensity in magnetic field B at temperature T and $I(0\,\mathrm{T}, T_{\mathrm{ref}})$ is the transmitted intensity in zero magnetic field at temperature T_{ref}. For the magnetic field ratios $T = T_{\mathrm{ref}}$, and the relative absorption spectra are noted as $\alpha_{\mathrm{B}}^{\pm}$. If B is constant and T is varied, the ratio is denoted by $\alpha_{T}^{\pm}$. $\alpha^{\pm}$ was determined for two polarizations of THz radiation $\mathbf{E}_{\omega} \parallel [010]$ and $\mathbf{E}_{\omega} \parallel [001]$.

The NDD was detected by changing the direction of the magnetic field from $+B$ to $-B$, i.e., from $\mathbf{B} \uparrow\uparrow \mathbf{k}$ to $\mathbf{B} \downarrow\uparrow \mathbf{k}$. Due to the twofold rotation symmetry along the [001] axis, the reversal of $\mathbf{B}$ is equivalent to the reversal of $\mathbf{k}$.

III. EXPERIMENTAL RESULTS

Figures 2(a) and 2(b) show the temperature dependence of $\alpha_{T}^{\pm}$ between 3 and 100 K in two polarizations of the THz radiation in magnetic field ±14 T. Below 7 K, in the magnetically ordered phase, the spectrum is dominated by three resonances as 18, 28, and 32 cm^{-1}. Since the resonance frequencies of the spin-wave modes are located at almost the same position [10] in $\mathrm{Sr_2CoSi_2O_7}$ and $\mathrm{Ba_2CoGe_2O_7}$, and the magnetic field dependence of $\mathbf{M}$ and $\mathbf{P}$ is also similar in the two compounds [16,19], we use the same assignment of spin waves as for $\mathrm{Ba_2CoGe_2O_7}$ [20]. The 18-cm^{-1} mode is the Goldstone mode of the easy-plane antiferromagnet gapped by the in-plane magnetic field whereas the latter two resonances correspond to the spin-stretching modes. When the field is parallel or antiparallel to the light propagation direction, the spectra are markedly different. The absorption difference is due to the MChD [7,10].

As the temperature increases, the spin-stretching modes at 28 and 32 cm^{-1} merge and eventually disappear above 30 K. However, the lowest-energy mode, the Goldstone mode

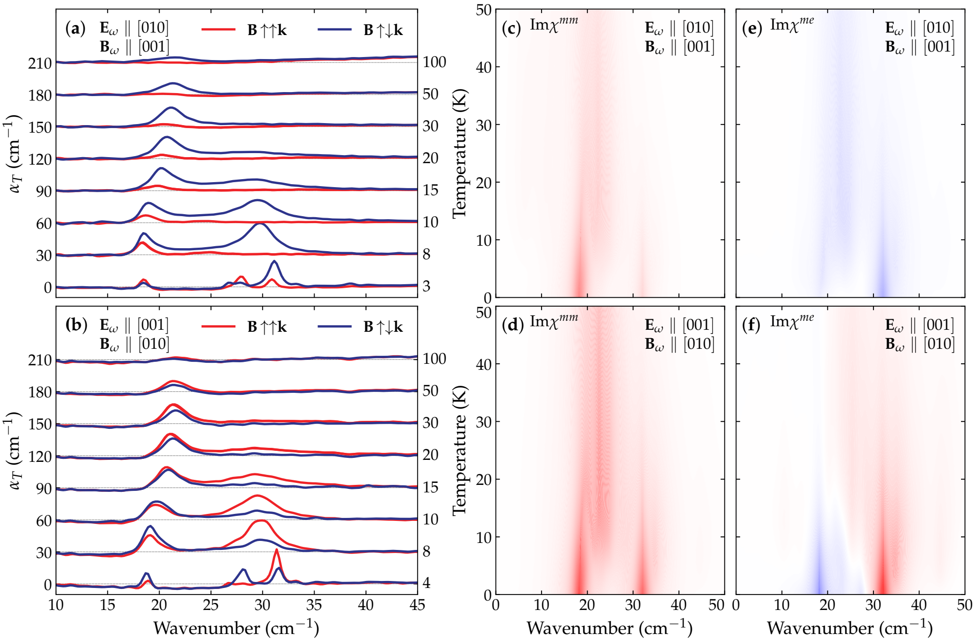

FIG. 2. Temperature dependence of measured THz absorption spectra (a), (b) and calculated susceptibilities (c)–(f) of $\mathrm{Sr_2CoSi_2O_7}$ in 14 T. The THz absorption spectra for magnetic field $\mathbf{B} \uparrow\uparrow \mathbf{k} \parallel [100]$ (red) and $\mathbf{B} \uparrow\downarrow \mathbf{k}$ (blue) are measured using linearly polarized radiation where in (a) $\mathbf{E}_{\omega} \parallel [010]$ and $\mathbf{B}_{\omega} \parallel [001]$, and in (b) the polarization is rotated by $\pi/2$, so that $\mathbf{E}_{\omega} \parallel [001]$ and $\mathbf{B}_{\omega} \parallel [010]$. The spectra measured at each temperature are shifted by a constant baseline. (c) and (e) are the magnetic susceptibility $\mathrm{Im}\chi^{mm}(\omega)$ and the ME susceptibility $\mathrm{Im}\chi^{me}(\omega)$ for the polarizations $\mathbf{E}_{\omega} \parallel [010]$ and $\mathbf{B}_{\omega} \parallel [001]$. (d) and (f) are $\mathrm{Im}\chi^{mm}(\omega)$ and $\mathrm{Im}\chi^{me}(\omega)$ for the polarization $\mathbf{E}_{\omega} \parallel [001]$ and $\mathbf{B}_{\omega} \parallel [010]$. Red (positive) and blue (negative) colors indicate the sign of the susceptibility. The saturation of the color corresponds to the magnitude of the corresponding susceptibility matrix elements, $\mathrm{Im}\chi^{mm}(\omega)$ [Eq. (11)] and $\mathrm{Im}\chi^{me}(\omega)$ [Eq. (12)]. The susceptibilities were calculated by the exact diagonalization of a four-site cluster.

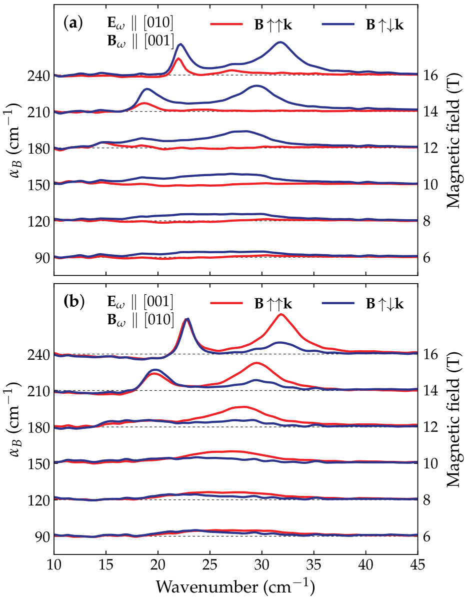

FIG. 3. Magnetic field dependence of absorption spectra of $\mathrm{Sr_2CoSi_2O_7}$ in the paramagnetic state at 10 K, $\mathbf{B}\uparrow\uparrow\mathbf{k}\parallel[100]$ (red) and $\mathbf{B}\uparrow\downarrow\mathbf{k}$ (blue). The spectra are shifted in proportion to the absolute value of the magnetic field.

in the ordered phase, is visible even at 100 K. The MChD has pronounced polarization dependence in the paramagnetic phase. A strong MChD is observed for all resonances in polarization $\mathbf{E}_\omega \parallel [010]$: the absorption coefficient is nearly zero for positive fields whereas finite absorption is detected for negative fields. In the orthogonal polarization $\mathbf{E}_\omega \parallel [001]$, the lowest-energy resonance has weak MChD and changes sign between 10 and 15 K.

In 14 T the MChD is the strongest at 10 K, close to the Néel temperature but already in the paramagnetic phase [see Figs. 2(a) and 2(b)]. The magnetic field dependence of the absorption spectra at 10 K is shown in Figs. 3(a) and 3(b). The Goldstone-type mode suddenly appears above 12 T and it only shows MChD for $\mathbf{E}_\omega \parallel [010]$. The remnant spin-stretching mode arises from the broad absorption feature in low magnetic field and has a strong MChD with opposite signs in the two polarizations.

The magnetic field dependence of the absorption spectra at 30 K is shown in Figs. 4(a) and 4(b). The average intensity of the single resonance line $(\alpha^+ + \alpha^-)/2$ observed at this temperature is nearly the same for both polarizations and it grows gradually as the field is increased. For polarization $\mathbf{E}_\omega \parallel [010]$ a strong MChD is observed while only a small absorption difference is detected in $\mathbf{E}_\omega \parallel [001]$.

IV. SPIN HAMILTONIAN AND MAGNETOELECTRIC COUPLING

We consider the following spin Hamiltonian for $S=\frac{3}{2}$ $\mathrm{Co^{2+}}$ spins coupled within a single layer (Fig. 1) of $\mathrm{Sr_2CoSi_2O_7}$:

$$\mathcal{H} = J\sum_{(i,j)}\left(S_i^x S_j^x + S_i^y S_j^y\right) + J_z\sum_{(i,j)} S_i^z S_j^z + \Lambda\sum_i \left(S_i^z\right)^2 + D_z\sum_{(i,j)}\left(S_i^x S_j^y - S_i^y S_j^x\right) - g\mu_{\mathrm{B}}\mathbf{B}\sum_i \mathbf{S}_i, \tag{2}$$

where J and J_z are the anisotropic exchange parameters, Λ is the onsite anisotropy parameter, D_z is the z component of the Dzyaloshinskii-Moriya vector, and the last term is the Zeeman interaction. (i,j) denotes pairs of nearest-neighbor sites with $i \in \mathrm{A}$ and $j \in \mathrm{B}$ (Fig. 1). The spin-nematic interactions responsible for the weak in-plane anisotropy are neglected [21,22].

From the symmetry point of view, the absence of inversion at the Co site allows the ME coupling. A suitable microscopic mechanism is provided by the spin-dependent p-d hybridization [23]. In the case of a tetrahedrally coordinated magnetic moment (the $\mathrm{Co^{2+}}$ ion in our case), the electric polarization is quadratic in spin components given by [19,24,25]

$$\mathbf{P} \propto \sum_{o=1}^{4} (\mathbf{S}\cdot\mathbf{e}_o)^2\mathbf{e}_o, \tag{3}$$

where $\mathbf{e}_o$ is the unit vector pointing from the center of the (distorted) tetrahedron toward the four $o = 1,\ldots,4$ ligands (the oxygen ions) at the vertices of the tetrahedron.

Since the $\mathrm{Sr_2CoSi_2O_7}$ is composed of alternating tetrahedra, the polarization components are

$$\begin{aligned}
P_j^x &\propto -\cos 2\kappa_j\left(S_j^x S_j^z + S_j^z S_j^x\right) - \sin 2\kappa_j\left(S_j^y S_j^z + S_j^z S_j^y\right),\\
P_j^y &\propto \cos 2\kappa_j\left(S_j^y S_j^z + S_j^z S_j^y\right) - \sin 2\kappa_j\left(S_j^x S_j^z + S_j^z S_j^x\right),\\
P_j^z &\propto \cos 2\kappa_j\left[\left(S_j^y\right)^2 - \left(S_j^x\right)^2\right] - \sin 2\kappa_j\left(S_j^x S_j^y + S_j^y S_j^x\right),
\end{aligned} \tag{4}$$

where j belongs to either sublattice A, with a tilt angle $\kappa_j = \kappa$, or to sublattice B, where $\kappa_j = -\kappa$ [24].

The oscillating magnetic field of the light interacts with the total magnetization

$$\mathbf{M} = \mathbf{M}_{\mathrm{A}} + \mathbf{M}_{\mathrm{B}}, \tag{5}$$

while the electric field interacts with the total polarization

$$\mathbf{P} = \mathbf{P}_{\mathrm{A}} + \mathbf{P}_{\mathrm{B}}, \tag{6}$$

where the sublattice (l = A or B) magnetization and polarization are

$$\mathbf{M}_l = g\mu_{\mathrm{B}}\sum_{j\in l}\mathbf{S}_j \quad \text{and} \quad \mathbf{P}_l = \sum_{j\in l}\mathbf{P}_j. \tag{7}$$

We define the magnetic susceptibility as

$$\chi_{\mu\mu}^{mm}(\omega) = \sum_{i,f}\frac{|\langle f|M^\mu|i\rangle|^2}{\hbar\omega - E_f + E_i + i\delta}\,\frac{e^{-\beta E_f} - e^{-\beta E_i}}{Z}, \tag{8}$$

and the ME susceptibility as

$$\chi_{\mu\nu}^{me}(\omega) = \sum_{i,f}\frac{\langle i|M^\mu|f\rangle\langle f|P^\nu|i\rangle}{\hbar\omega - E_f + E_i + i\delta}\,\frac{e^{-\beta E_f} - e^{-\beta E_i}}{Z}, \tag{9}$$

where $Z = \sum_i e^{-\beta E_i}$ is the partition sum, $\beta = 1/k_{\mathrm{B}}T$ is the inverse temperature, the δ parameter gives a finite broadening

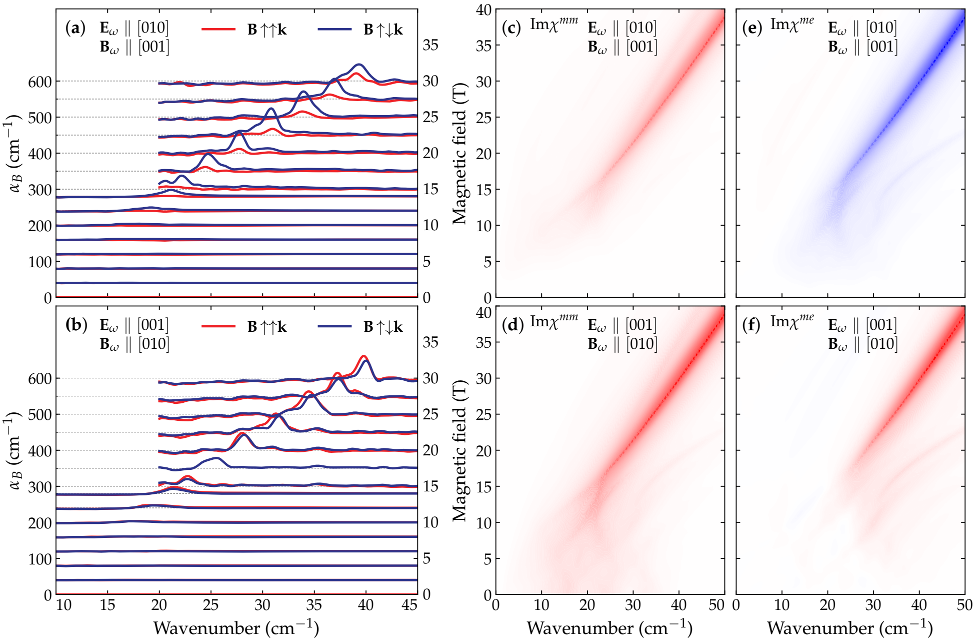

FIG. 4. Magnetic field dependence of measured THz absorption spectra (a), (b) and calculated susceptibilities (c)–(f) of $Sr_2CoSi_2O_7$ at 30 K. The THz absorption spectra for magnetic field $\mathbf{B} \uparrow\uparrow \mathbf{k} \parallel [100]$ (red) and $\mathbf{B} \uparrow\downarrow \mathbf{k}$ (blue) are shown for two polarizations of the THz light. The spectra are shifted in proportion to the absolute value of the magnetic field. (c) and (e) are the magnetic susceptibility $\mathrm{Im}\chi^{mm}(\omega)$ and the ME susceptibility $\mathrm{Im}\chi^{me}(\omega)$ for the polarizations $\mathbf{E}_\omega \parallel [010]$ and $\mathbf{B}_\omega \parallel [001]$. (d) and (f) are $\mathrm{Im}\chi^{mm}(\omega)$ and $\mathrm{Im}\chi^{me}(\omega)$ for the polarizations $\mathbf{E}_\omega \parallel [001]$ and $\mathbf{B}_\omega \parallel [010]$. Red (positive) and blue (negative) colors indicate the sign of susceptibility. The saturation of the color corresponds to the magnitude of the corresponding susceptibility matrix elements $\mathrm{Im}\chi^{mm}(\omega)$ [Eq. (11)] and $\mathrm{Im}\chi^{me}(\omega)$ [Eq. (12)]. The susceptibilities were calculated by the exact diagonalization of a four-site cluster.

to the absorption peaks, and E_i and E_f are the energies of the initial and final spin states, respectively.

The experimentally measured NDD is related to the imaginary *and* time-reversal odd part of ME susceptibility [13,26] as

$$\alpha^+(\omega) - \alpha^-(\omega) = \frac{4\omega}{c_0}\mathrm{Im}\chi^{me}_{\mu\nu}(\omega), \qquad (10)$$

where c_0 is the speed of light in vacuum and frequency is in units of rad/s.

For a given transition $|i\rangle \rightarrow |f\rangle$ the imaginary (dissipative) parts of the magnetic and magnetoelectric susceptibilities are [13]

$$\mathrm{Im}\chi^{mm}_{\mu\mu}(\omega) \propto |\langle i|M^\mu|f\rangle|^2\delta(\omega - \omega_{if}), \qquad (11)$$

$$\mathrm{Im}\chi^{me}_{\mu\nu}(\omega) \propto \mathrm{Re}\{\langle i|M^\mu|f\rangle\langle f|P^\nu|i\rangle\}\delta(\omega - \omega_{if}), \qquad (12)$$

where $\omega_{if} = (E_f - E_i)/\hbar$ is the transition frequency and ω is the frequency of a photon. Only the real part of the matrix element products is time-reversal odd in Eq. (12).

V. EXACT DIAGONALIZATION

To get a first insight into the nature of excitations, we performed an exact diagonalization study of a small cluster containing four Co^{2+} ions, i.e., two unit cells, at finite temperatures [27]. We note that exact diagonalization was also used to study the ME excitations of $Ba_2CoGe_2O_7$ at zero temperature in Ref. [24].

Since the magnetization curves closely follow those of $Ba_2CoGe_2O_7$ [16,19], we assume the same set of parameters describes both $Ba_2CoGe_2O_7$ and $Sr_2CoSi_2O_7$. We use the parameters obtained from absorption spectra of $Ba_2CoGe_2O_7$ in Ref. [20], i.e., $\Lambda = 13.4$ K, $J = 2.3$ K, $J_{zz} = 1.8$ K, $D_z = -0.1$ K, $\kappa = 22.4^\circ$, and $g = 2.3$. This set of parameters provided a remarkable good agreement with the experimentally measured absorptions. The results of these calculations are presented in Figs. 2(c)–2(f) and Figs. 4(c)–4(f).

The exact diagonalization results show, in accordance with the experiment, that a single absorption line is present in high magnetic fields at high temperatures and a second resonance appears as the temperature is lowered below 20 K. Calculation predicts a finite ME effect responsible for the observed NDD. Moreover, the sign change of NDD observed for $\mathbf{E}_\omega \parallel [001]$ between 10 and 15 K is reproduced by the numerical calculations [Figs. 2(b) and 2(f)].

VI. SINGLE-ION PROBLEM

In order to get a deeper understanding of the THz absorption spectra and NDD in the paramagnetic phase of $Sr_2CoSi_2O_7$, we consider a model of a single Co^{2+} spin in

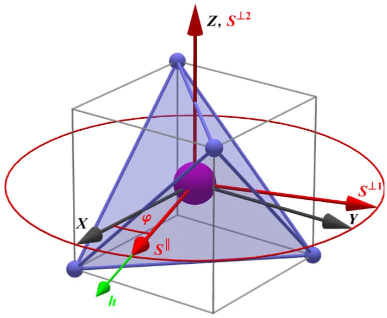

FIG. 5. The tetrahedron-fixed coordinate system $\{X, Y, Z\}$ and the rotated magnetic-field-fixed coordinate system $\{\parallel, \perp 1, \perp 2\}$. Purple ball is the Co^{2+} and the blue tetrahedron is the cage with the oxygen ions at the vertices. The quantization axis (spin component $S^{\parallel}$) is parallel to the direction of the static external magnetic field h (shown in green), while one perpendicular axis (the spin component $S^{\perp 2}$) is parallel to Z.

the center of a tetrahedron. This unit is the building block of the crystal lattice of $Sr_2CoSi_2O_7$, and, at the same time, its symmetry is representative of the field-induced reduction of the point symmetry in the real material. More precisely, in the next two sections we will show that the magnetic space group at the Γ point is isomorphic to the magnetic point group of the tetrahedron. Furthermore, such a simple single-ion model describes the essence of the experiments in the disordered paramagnetic state where the strong thermal fluctuations smear out the coupling to the neighboring spins.

A. Hamiltonian and the symmetries

1. *Spin Hamiltonian and the electric polarization*

We will consider magnetic field in the XY plane of a single tetrahedron with a coordinate system defined in Fig. 5. It is convenient to use the coordinate system where the $\parallel$ axis points in the direction of the field $h = g\mu_B B$, the $\perp 2$ axis is parallel to the Z direction, and the $\perp 1$ direction is chosen so that the three axes form an orthogonal right-handed system. The spin components in the coordinate system of the tetrahedron are related to the spin components in the field-fixed system as

$$\begin{aligned} S^X &= \cos\varphi\; S^{\parallel} - \sin\varphi\; S^{\perp 1},\\ S^Y &= \sin\varphi\; S^{\parallel} + \cos\varphi\; S^{\perp 1},\\ S^Z &= S^{\perp 2}. \end{aligned} \tag{13}$$

Following Eq. (2) the Hamiltonian for a single spin in the field-fixed coordinates is

$$\mathcal{H} = \Lambda (S^{\perp 2})^2 - h S^{\parallel}. \tag{14}$$

The quantization axis is chosen along the magnetic field with eigenvalues and eigenvectors of $S^{\parallel}$ being $\{+3/2, +1/2, -1/2, -3/2\}$ and $\{\Uparrow, \uparrow, \downarrow, \Downarrow\}$, respectively.

The magnetic field and the anisotropy lower the O(3) spatial symmetry to the group generated by inversion and a twofold rotation $C_2^{\parallel}$ about the magnetic field. Time-reversal symmetry alone is broken, but time reversal followed by a rotation perpendicular to the field, denoted by $\Theta C_2^{\perp 2}$, remains a symmetry element.

TABLE I. Character table of the double group corresponding to the group C_2, including the transformation properties of the operators and states. The group element $\bar{\mathbf{1}}$ is the 2π rotation with the property $\bar{\mathbf{1}}^2 = \mathbf{1}$.

Irrep	**1**	$C_2^{\parallel}$	$\bar{\mathbf{1}}$	$\bar{C}_2^{\parallel}$	Operators
A	1	1	1	1	$S^{\parallel}$, $P^{\parallel}$
B	1	−1	1	−1	$S^{\perp 1}$, $S^{\perp 2}$, $P^{\perp 1}$, $P^{\perp 2}$
$\bar{E}_1$	1	i	−1	$-i$	$\lvert\Downarrow\rangle$, $\lvert\uparrow\rangle$, $\langle\Uparrow\rvert$, $\langle\downarrow\rvert$
$\bar{E}_2$	1	$-i$	−1	i	$\lvert\Uparrow\rangle$, $\lvert\downarrow\rangle$, $\langle\Downarrow\rvert$, $\langle\uparrow\rvert$

From Eq. (3) we get for the electric polarization

$$\begin{aligned} P^X &= \eta_{XY}(S^Z S^Y + S^Y S^Z),\\ P^Y &= \eta_{XY}(S^Z S^X + S^X S^Z),\\ P^Z &= \eta_Z(S^X S^Y + S^Y S^X), \end{aligned} \tag{15}$$

where for the regular tetrahedron $\eta_{XY} = \eta_Z$. The relation to the components in the field-fixed coordinates is

$$\begin{aligned} P^X &= \cos\varphi\; P^{\parallel} - \sin\varphi\; P^{\perp 1},\\ P^Y &= \sin\varphi\; P^{\parallel} + \cos\varphi\; P^{\perp 1},\\ P^Z &= P^{\perp 2}. \end{aligned} \tag{16}$$

2. *Solution of the Hamiltonian*

The matrix representation of the Hamiltonian (14) in the spin basis $\{\Uparrow, \uparrow, \downarrow, \Downarrow\}$ is

$$\hat{\mathcal{H}} = \begin{pmatrix} \frac{3}{4}\Lambda - \frac{3}{2}h & 0 & -\frac{\sqrt{3}}{2}\Lambda & 0\\ 0 & \frac{7}{4}\Lambda - \frac{1}{2}h & 0 & -\frac{\sqrt{3}}{2}\Lambda\\ -\frac{\sqrt{3}}{2}\Lambda & 0 & \frac{7}{4}\Lambda + \frac{1}{2}h & 0\\ 0 & -\frac{\sqrt{3}}{2}\Lambda & 0 & \frac{3}{4}\Lambda + \frac{3}{2}h \end{pmatrix}. \tag{17}$$

The eigenvalues $\pm i$ of the rotation operator $\hat{C}_2^{\parallel}$,

$$\hat{C}_2^{\parallel} = e^{i\pi \hat{S}^{\parallel}} = \begin{pmatrix} -i & 0 & 0 & 0\\ 0 & i & 0 & 0\\ 0 & 0 & -i & 0\\ 0 & 0 & 0 & i \end{pmatrix}, \tag{18}$$

are good quantum numbers as the operator commutes with the Hamiltonian $[\hat{\mathcal{H}}, \hat{C}_2^{\parallel}] = 0$. Therefore, only the states with the same eigenvalue of $\hat{C}_2^{\parallel}$ are mixed. We use $\pm i$ to label the eigenstates $|\psi_j^{(\pm i)}\rangle$ and corresponding energies $\varepsilon_j^{(\pm i)}$. For the detailed form of the energies and eigenvectors, we refer the reader to Appendix B 1.

3. *Transition matrix elements*

Based on the transformation properties under the rotation $C_2^{\parallel}$, as summarized in Table I, we can construct selection rules for the matrix elements of the spin and polarization components. A matrix element for an operator $\mathcal{O}$ between states $|\psi_\alpha\rangle$ and $|\psi_\beta\rangle$ can only be nonvanishing if it transforms according to the totally symmetric A irrep of the group

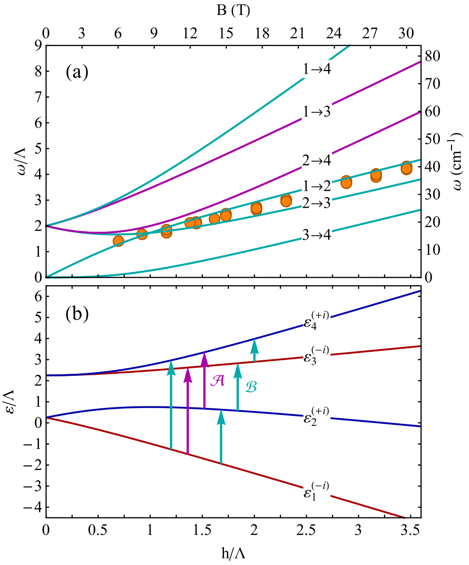

FIG. 6. (a) Transition energies ω and (b) energy levels ε of the single-ion model with easy-plane anisotropy Λ in a magnetic field $h = g\mu_B B$ within the easy plane as a function of h/Λ, with $\Lambda = 13.4$ K and $g = 2.3$ from Ref. [20]. States 1 and 3 (red curves) are multiplied by $-i$ after a π rotation about the field ($C_2^{\parallel}$), while states 2 and 4 (blue) get an i. Magenta arrows represent transitions between the states of the same symmetry, induced by operator $\mathcal{A}$, even under the $C_2^{\parallel}$, such as $S^{\parallel}$, $P^{\parallel}$ (see Table I). Cyan arrows connect states with different symmetries induced by operator $\mathcal{B}$, odd under $C_2^{\parallel}$, such as the perpendicular components of spin and polarization operator. The color of the curves corresponds to the color of the arrows in (b). The filled circles show the experimental results.

$\mathsf{A} \subseteq \Gamma^{\beta} \otimes \Gamma(\mathcal{O}) \otimes \Gamma^{\alpha}$. In order to describe the transformation properties of the states of a half-integer spin, we need to consider the double group corresponding to the group C_2. If an operator $\mathcal{A}$ transforms as A and an operator $\mathcal{B}$ as B, and the spin states as $\overline{\mathsf{E}}_1$ and $\overline{\mathsf{E}}_2$ of the double group of C_2 (Table I), the nonvanishing matrix elements are

$$\left\langle\psi_{\alpha}^{(\pm i)}\middle|\mathcal{A}\middle|\psi_{\beta}^{(\pm i)}\right\rangle \quad \text{and} \quad \left\langle\psi_{\alpha}^{(\mp i)}\middle|\mathcal{B}\middle|\psi_{\beta}^{(\pm i)}\right\rangle. \tag{19}$$

Allowed transitions between states of the same symmetry are of type $\mathcal{A}$ and allowed transitions between states of different symmetry are of type $\mathcal{B}$. The corresponding transition energies are shown in Fig. 6(a) and the energy levels involved in Fig. 6(b).

In what follows, we take into account the effects of antiunitary symmetries containing the time-reversal operation Θ on the matrix elements. We show in the Appendix A that any linear operator $\hat{\mathcal{O}}$, if the symmetry operation $\Theta C_2^{\perp 2}$ is present (as in the case of a magnetic field applied in the XY plane), must satisfy $\hat{\mathcal{O}} = \pm\hat{\mathcal{O}}^*$. Thus, the matrix elements of any linear operator even (odd) under the symmetry operation $\Theta C_2^{\perp 2}$ are real (imaginary).

In conclusion, the unitary symmetries of the single-ion model determine the selection rules, i.e., the nonvanishing matrix elements, whereas the antiunitary symmetry constrains the matrix element to a real or to an imaginary value.

TABLE II. Matrix elements of the spin and polarization operators, first in small field h, then for small anisotropy Λ, in the single-ion model. The first nonvanishing order in either h or Λ is shown. c stands for a real constant.

Transition	$S^{\parallel}$	$S^{\perp 1}$	$S^{\perp 2}$	$P_{\text{chiral}}^{\parallel}$, $P_{\text{polar}}^{\perp 1}$	$P_{\text{chiral}}^{\perp 1}$, $P_{\text{polar}}^{\parallel}$	$P_{\text{chiral}}^{\perp 2}$	$P_{\text{polar}}^{\perp 2}$
$1 \to 2$		c, c	ic, ic		ih, ic	h, c	
$2 \to 3$		c, c	ih, ic		$ic, i\Lambda$	c, Λ	
$3 \to 4$		h^2, c	ic, ic		ih, ic	h, c	
$1 \to 3$	c, Λ			ic, ic			c, c
$2 \to 4$	c, Λ			ic, ic			c, c
$1 \to 4$		c, Λ^2	$ih, i\Lambda^2$		$ic, i\Lambda$	c, Λ	

B. Directional dichroism in the single-ion model

Imaginary part of the ME susceptibility $\mathrm{Im}\chi_{\mu\nu}^{me}(\omega)$ causes NDD [6,7,28] [Eq. (10)]. For a given transition $|i\rangle \to |f\rangle$ the dissipative and time-reversal odd part of the ME susceptibility is proportional to the real part of the matrix element product $\mathrm{Re}\{\langle f|M^{\mu}|i\rangle\langle f|P^{\nu}|i\rangle\}$ [Eq. (12)]. Thus, NDD is nonzero if both matrix elements are nonzero for the same pair of states $|i\rangle$ and $|f\rangle$. This is allowed by symmetry if M^{μ} and P^{ν} transform according to the same irreducible representation of the group of unitary symmetries.

Furthermore, the product of the M^{μ} and P^{ν} matrix elements has a finite real part only if both matrix elements are real or both are imaginary. Thus, both operators must be even ($\mathcal{A}$ type) or both odd ($\mathcal{B}$ type) under antiunitary symmetry operation, as was shown in the previous section. The summary of all spin and polarization operator amplitudes for $S = \frac{3}{2}$ in the single-ion model is presented in Table II. They are either real, imaginary, or symmetry forbidden.

Below we examine the symmetry properties of the operators for different directions of the external field with respect to the cobalt-oxygen tetrahedron in the easy plane to find out the details of the existence of NDD.

1. *Magnetochiral dichroism (chiral case):* $\varphi = 0$

When the external field is parallel to one of the twofold rotation axes $\varphi = 0$ (see Fig. 5), the system has chiral symmetry $D_2(C_2)$ in Schoenflies notation [see Fig. 7(a)], and the polarization operators in the local coordinate system are

$$P_{\text{chiral}}^{\parallel} = \frac{\eta_{XY}}{2i}[(S^{+})^2 - (S^{-})^2], \tag{20a}$$

$$P_{\text{chiral}}^{\perp 1} = \frac{\eta_{XY}}{2i}[S^{\parallel}(S^{+} - S^{-}) + (S^{+} - S^{-})S^{\parallel}], \tag{20b}$$

$$P_{\text{chiral}}^{\perp 2} = \frac{\eta_{Z}}{2}[S^{\parallel}(S^{+} + S^{-}) + (S^{+} + S^{-})S^{\parallel}], \tag{20c}$$

where $S^{\pm} = S^{\perp 1} \pm iS^{\perp 2}$. This is also the case (up to a sign) when φ is an integer multiple of $\pi/2$ due to the S_4 symmetry of the distorted oxygen tetrahedron. It is worth noting that the perpendicular components $P^{\perp 1}$ and $P^{\perp 2}$ change the $S^{\parallel}$ quantum number by ± 1, creating dipolar spin excitation, but

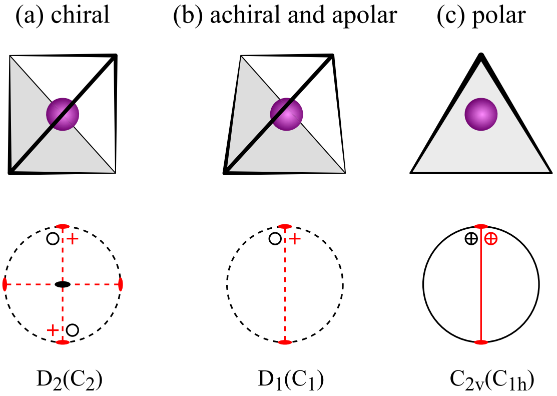

FIG. 7. The tetrahedron in the (a) chiral ($\varphi = 0$), (b) low-symmetry, and (c) polar ($\varphi = \pi/4$) cases as seen from the direction of the magnetic field **B**. The magenta sphere represents the magnetic ion at the center of tetrahedral cage. The stereograms represent the magnetic point group for each case, black refers to the unitary subgroup, and red the antiunitary part combined with the time reversal.

$P^{\parallel}_{\text{chiral}}$ changes by ±2, creating quadrupolar spin excitation [29].

None of the components of **P** transform according to the fully symmetric irreducible representation A_+ (Table III). Therefore, the expectation value for the static polarization is zero in the ground state. Although the chiral case is apolar, the dynamic ME susceptibility is allowed. The operators $S^{\perp 2}$ and $P^{\perp 1}$ belong to the same irreducible representation B_- of $D_2(C_2)$, thus, the dynamic ME susceptibility is allowed. As the oscillating magnetization $S^{\perp 2}$ and polarization $P^{\perp 1}$ are perpendicular to each other and to the external magnetic field, we expect NDD in the Faraday geometry, when the light is propagating parallel to the field. This effect is nothing else but the MChD. The operators $S^{\perp 1}$ and $P^{\perp 2}$, corresponding to the perpendicular polarization of radiation as compared to $S^{\perp 2}$ and $P^{\perp 1}$, belong to the same irreducible representation B_+ and therefore the NDD will appear irrespective of polarizations of the incident light in Faraday geometry. The symmetry argument presented above is supported by the direct evaluation of the matrix elements (see Appendix B and Table II) using the eigenstates given in Eqs. (B2a)–(B2d).

TABLE III. Character table for the magnetic point groups and symmetry-allowed operators for three orientations of the applied magnetic field in the easy plane (see Fig. 5), creating chiral ($\varphi = 0$), polar ($\varphi = \pi/4$), and low-symmetry cases.

		$\varphi = 0$: chiral case, the group is $D_2(C_2)$				
Irrep.	**1**	$C_2^{\parallel}$	$\Theta C_2^{\perp 2}$	$\Theta C_2^{\perp 1}$	Operator(s)	NDD
A_+	1	1	1	1	$S^{\parallel}$	
A_-	1	1	−1	−1	$P^{\parallel}$	
B_+	1	−1	1	−1	$S^{\perp 1}$, $P^{\perp 2}$	Faraday
B_-	1	−1	−1	1	$S^{\perp 2}$, $P^{\perp 1}$	Faraday
		$\varphi = \pi/4$: polar case, the group is $C_{2v}(C_{1h})$				
	1	$\sigma^{\parallel}$	$\Theta C_2^{\perp 2}$	$\Theta \sigma^{\perp 1}$		
A_+	1	1	1	1	$S^{\parallel}$, $P^{\perp 2}$	Voigt
A_-	1	1	−1	−1	$P^{\perp 1}$	
B_+	1	−1	1	−1	$S^{\perp 1}$	
B_-	1	−1	−1	1	$S^{\perp 2}$, $P^{\parallel}$	Voigt
		$\varphi \neq 0$ nor $\pi/4$: the group is $D_1(C_1)$				
	1		$\Theta C_2^{\perp 2}$			
Γ_+	1		1		$S^{\parallel}$, $S^{\perp 1}$, $P^{\perp 2}$	Both
Γ_-	1		−1		$S^{\perp 2}$, $P^{\parallel}$, $P^{\perp 1}$	Both

From Table III we can also infer the selection rules with regard to the quantum numbers $\pm i$, the eigenvalues of the rotation operator $C_2^{\parallel}$. The $S^{\parallel}$ and $P^{\parallel}$ are invariant under $C_2^{\parallel}$, thus, they excite only type-$\mathcal{A}$ transitions between states that have the same quantum number [see Fig. 6(b)], i.e., between states 1 and 3 and between states 2 and 4. However, there is no NDD for the $\mathcal{A}$-type transitions as $P^{\parallel}$ and $S^{\parallel}$ do not transform according to the same irrep.

The perpendicular components of **P** and **S** have matrix elements between states with different $C_2^{\parallel}$ quantum numbers, which corresponds to type-$\mathcal{B}$ transitions, i.e., transitions 1 → 2, 1 → 4, 2 → 3, and 3 → 4 [see Fig. 6(b)]. We also see in Table III that $S^{\perp 2}$ and $P^{\perp 1}$ are both odd under $\Theta C_2^{\perp 2}$, with imaginary matrix elements, and their product is real in Eq. (12), providing a finite imaginary $\chi^{me}_{\perp 2,\perp 1}(\omega)$ and a finite MChD. Similarly, the $S^{\perp 1}$ and $P^{\perp 2}$ are both even, with real matrix elements, providing a finite imaginary $\chi^{me}_{\perp 1,\perp 2}(\omega)$. In any other configuration the $\mathrm{Im}\{\chi^{me}_{\mu\nu}(\omega)\} = 0$. Therefore, the NDD is present only in the Faraday configuration, $\mathbf{k} \parallel \mathbf{B}$.

2. Toroidal dichroism (polar case): $\varphi = \frac{\pi}{4}$

If the field direction is parallel to the upper edge of the tetrahedron, $\varphi = \frac{\pi}{4}$ in Fig. 5, and the polarization operators are

$$P^{\parallel}_{\text{polar}} = \frac{\eta_{XY}}{2i}[S^{\parallel}(S^{+} - S^{-}) + (S^{+} - S^{-})S^{\parallel}], \tag{21a}$$

$$P^{\perp 1}_{\text{polar}} = \frac{\eta_{XY}}{2i}[(S^{-})^2 - (S^{+})^2], \tag{21b}$$

$$P^{\perp 2}_{\text{polar}} = \frac{\eta_{Z}}{4}[4(S^{\parallel})^2 - (S^{-})^2 - (S^{+})^2 - S^{-}S^{+} - S^{+}S^{-}]. \tag{21c}$$

Here, the perpendicular operators are changing the $S^{\parallel}$ quantum number by 0 and ±2, and the $P^{\parallel}$ parallel operator by ±1. We note that $P^{\parallel}_{\text{polar}} = P^{\perp 1}_{\text{chiral}}$ and $P^{\perp 1}_{\text{polar}} = -P^{\parallel}_{\text{chiral}}$, reflecting the spin-quadrupolar nature of the polarization operators.

As shown in Fig. 7(c), the symmetry group of the spin Hamiltonian is now $C_{2v}(C_{1h}) = 2'm'm$ with elements

$$C_{2v}(C_{1h}) = 2'm'm = \{\mathbf{1}, \sigma^{\parallel}, \Theta C_2^{\perp 2}, \Theta\sigma^{\perp 1}\}. \tag{22}$$

The character table and the transformations of physical quantities under this group are given in Table III.

If we compare to the chiral case, first, we observe that the $P^{\perp 2}$ transforms as identity, therefore electric polarization along ⊥ 2 axis is now allowed by the symmetry, hence we refer to this case as the *polar* case. Second, because of the $\sigma^{\parallel}$ symmetry element the $S^{\perp 1}$ and $P^{\perp 2}$ do not belong to the same irreducible representation anymore, and similarly $S^{\perp 2}$ and $P^{\perp 1}$. As a consequence, the NDD in the Faraday geometry vanishes. Indeed, in Faraday geometry $\mathbf{k} \parallel \mathbf{B}$, the

THz field transforms under $\sigma^{\|}$ as $\mathbf{B}_\omega \to -\mathbf{B}_\omega$, $\mathbf{E}_\omega \to \mathbf{E}_\omega$, and $\mathbf{k} \to -\mathbf{k}$. The two directions of the radiation propagation are connected by the symmetry element and NDD is forbidden [5,13].

Instead, the $S^{\perp 2}$ and $P^{\|}$ transform according to the same irreducible representation B_-. As a consequence, a finite ME susceptibility $\chi^{me}_{\perp 2,\|}$ will appear in the Voigt geometry when the $\mathbf{k}$ is parallel to the $\perp 1$ and $\mathbf{E}_\omega \parallel \mathbf{B}$. Similarly, the $S^{\|}$ and $P^{\perp 2}$ both belong to A_+, providing a finite $\chi^{me}_{\|,\perp 2}$. Since the operators belonging to the same irreducible representation in Table III have the same parity under $\Theta C_2^{\perp 2}$ transformation, their matrix elements are either both real (for $S^{\perp 2}$ and $P^{\|}$), or are both pure imaginary (for $S^{\|}$ and $P^{\perp 2}$), allowing NDD in the Voigt configuration in both polarizations of THz radiation.

As the $\sigma^{\|}$ and $C_2^{\|}$ are given by the same matrix in Eq. (18) [30], we can repeat the arguments we used in the chiral case to determine the selection rules. The $S^{\|}$ and $P^{\perp 2}$ operators have finite matrix elements between states with the same $\hat{C}_2^{\|} \equiv \hat{\sigma}^{\|}$ quantum number, i.e., the $\mathcal{A}$-type transitions 1 → 3 and 2 → 4 are allowed. The $S^{\perp 2}$ and $P^{\|}$ change the quantum number $\pm i \to \mp i$ and the $\mathcal{B}$-type transitions 1 → 2, 1 → 4, 2 → 3, and 3 → 4 are allowed.

3. *Low-symmetry case: $\varphi \neq 0$ nor $\frac{\pi}{4}$*

For arbitrary direction of the external magnetic field within the XY plane, the polarization operators can be written as a linear combination of the chiral and polar cases considered above:

$$\mathbf{P} = \cos 2\varphi\, \mathbf{P}_{\text{chiral}} + \sin 2\varphi\, \mathbf{P}_{\text{polar}}. \tag{23}$$

Here, only the $\Theta C_2^{\perp 2}$ symmetry remains and the magnetic point group is reduced to the $D_1(C_1) = 2'$ [see Table III and Fig. 7(b)]. Since neither $C_2^{\|}$ nor $\sigma^{\|}$ is a symmetry element of the full problem, the $\mathbf{P}$ may have finite matrix elements between any of the $(\pm i)$ states, and the selection rules we established for the chiral ($\varphi = 0$) and the polar ($\varphi = \pi/4$) case are not valid. However, as the spin state still respects the quantum number set by the $C_2^{\|}$, the associated selection rules [Eq. (19)] hold for $S^{\|}$, $S^{\perp 1}$, and $S^{\perp 2}$. Furthermore, since the ME susceptibility is composed from a product of matrix elements of $\mathbf{S}$ and $\mathbf{P}$, it inherits the selection rules of the matrix element of $\mathbf{S}$. Putting all this together, the single-ion system shows NDD in the Faraday geometry for the 1 → 2, 2 → 3, 1 → 4, and 3 → 4 transitions with $\chi^{me} \propto \cos 2\varphi$ coming from the chiral part, and NDD in the Voigt geometry according to the selection rules set by the polar case with $\chi^{me} \propto \sin 2\varphi$.

VII. LATTICE PROBLEM

This section describes the selection rules when the tetrahedra form a lattice. Furthermore, we give the analytical form of the transition energies by taking into account the exchange coupling between the spins in the lowest order in perturbation theory.

A. Magnetochiral dichroism and selection rules in the lattice problem

In the material the oxygen tetrahedra are rotated alternatingly, there is no direction of the external field which would show purely either the chiral or the polar case discussed in the section above. However, the situation is not hopeless: if the external field is along the [100] direction (as in the actual experiment), there is a $\{C_2^{\|}|[\frac{1}{2}00]\}$ screw axis (shown in Fig. 1 as 2_1) which is a symmetry operation. The screw axis performs a π rotation about the [100] axis and a half-translation along the same axis to move the A tetrahedra into B and vice versa (see Fig. 1). The screw axis is a symmetry element of the lattice spin Hamiltonian symmetry group, so we can use its irreducible representations to label the eigenstates and the operators. In addition, the $\{\Theta C_2^{\perp 2}|[000]\}$ (the rotation by π about the [001] axes through the center of a tetrahedron followed by a time-reversal operation) is a symmetry element irrespectively from the direction of the in-plane magnetic field. In fact, this nonsymmorphic magnetic point group is isomorphic to the $D_2(C_2) = 22'2'$ magnetic point group of a single tetrahedron in the chiral case:

$$\begin{aligned}&\left\{\mathbf{1}, \{C_2^{\|}|[\tfrac{1}{2}00]\}, \{\Theta C_2^{\perp 2}|[000]\}, \{\Theta C_2^{\perp 1}|[0\tfrac{1}{2}0]\}\right\}\\ &\quad\cong \left\{\mathbf{1}, C_2^{\|}, \Theta C_2^{\perp 2}, \Theta C_2^{\perp 1}\right\}.\end{aligned} \tag{24}$$

Let us examine the selection rules based on what we learned for a single ion. We express the magnetization [Eq. (5)] and the polarization [Eq. (6)] in the magnetic-field-fixed coordinate system and decompose into the irreducible representations of the unitary part of the point group, which consists of the identity and the $\{C_2^{\|}|[\frac{1}{2}00]\}$ screw axis. The screw axis acts on the magnetization as

$$\begin{pmatrix} M_{\rm A}^{\|} \\ M_{\rm A}^{\perp 1} \\ M_{\rm A}^{\perp 2} \end{pmatrix} \to \begin{pmatrix} M_{\rm B}^{\|} \\ -M_{\rm B}^{\perp 1} \\ -M_{\rm B}^{\perp 2} \end{pmatrix}, \tag{25a}$$

$$\begin{pmatrix} M_{\rm B}^{\|} \\ M_{\rm B}^{\perp 1} \\ M_{\rm B}^{\perp 2} \end{pmatrix} \to \begin{pmatrix} M_{\rm A}^{\|} \\ -M_{\rm A}^{\perp 1} \\ -M_{\rm A}^{\perp 2} \end{pmatrix}. \tag{25b}$$

Similar considerations hold for the polarization operators.

Since the unitary part of the point group has two irreducible representations, the $\mathbf{M}$ operator can be decomposed into even ($\mathbf{M_0}$) and odd ($\mathbf{M}_{\boldsymbol{\pi}}$) parts as $\mathbf{M} = \mathbf{M_0} + \mathbf{M}_{\boldsymbol{\pi}}$.

1. *Selection rules for the even* (**0**) *components*

Using the transformation rules given by Eq. (25), the even part of $\mathbf{M}$ is

$$M_{\mathbf{0}}^{\|} = M_{\rm A}^{\|} + M_{\rm B}^{\|}, \tag{26a}$$

$$M_{\mathbf{0}}^{\perp} = 0, \tag{26b}$$

and for the polarizations we get

$$P_{\mathbf{0}}^{\|} = \sin 2\kappa \sum_j (-1)^j P_{j,\text{polar}}^{\|} - \cos 2\kappa \sum_j P_{j,\text{chiral}}^{\|}, \tag{27a}$$

$$P_{\mathbf{0}}^{\perp} = 0, \tag{27b}$$

where $\perp = \perp 1, \perp 2$ and the index j runs over all the sites, being an even integer on A and odd integer on the B sublattice; $P^{\parallel}_{j,\text{chiral}}$ is defined by Eq. (20a) and $P^{\parallel}_{j,\text{polar}}$ by Eq. (21a), with the corresponding spin operators at site j. The light does not interact with the system in the Faraday geometry in the even channel because $P^{\perp}_{\mathbf{0}} = M^{\perp}_{\mathbf{0}} = 0$.

2. Selection rules for the odd (π) components

When we antisymmetrize, we get the odd quantities $\mathbf{M}_{\boldsymbol{\pi}}$ and $\mathbf{P}_{\boldsymbol{\pi}}$, and following the steps we used to obtain the even components above, the corresponding magnetization and polarization components are

$$M^{\parallel}_{\boldsymbol{\pi}} = 0, \tag{28a}$$

$$M^{\perp}_{\boldsymbol{\pi}} = M^{\perp}_{\text{A}} + M^{\perp}_{\text{B}} \tag{28b}$$

and

$$P^{\parallel}_{\boldsymbol{\pi}} = 0, \tag{29a}$$

$$P^{\perp}_{\boldsymbol{\pi}} = \sin 2\kappa \sum_j (-1)^j P^{\perp}_{j,\text{polar}} - \cos 2\kappa \sum_j P^{\perp}_{j,\text{chiral}}\,. \tag{29b}$$

The nonvanishing perpendicular components $\{M^{\perp 1}_{\boldsymbol{\pi}}, P^{\perp 2}_{\boldsymbol{\pi}}\}$ and $\{M^{\perp 2}_{\boldsymbol{\pi}}, P^{\perp 1}_{\boldsymbol{\pi}}\}$ lead to a finite ME susceptibility and NDD in the Faraday geometry for the odd channel.

We now examine the effect of the time reversal. The action of the $\{\Theta C^{\perp 2}_2 | [000]\}$ is given by

$$\begin{pmatrix} M^{\parallel}_{\text{A}} \\ M^{\perp 1}_{\text{A}} \\ M^{\perp 2}_{\text{A}} \end{pmatrix} \to \begin{pmatrix} M^{\parallel}_{\text{A}} \\ M^{\perp 1}_{\text{A}} \\ -M^{\perp 2}_{\text{A}} \end{pmatrix}, \tag{30a}$$

$$\begin{pmatrix} P^{\parallel}_{\text{A}} \\ P^{\perp 1}_{\text{A}} \\ P^{\perp 2}_{\text{A}} \end{pmatrix} \to \begin{pmatrix} -P^{\parallel}_{\text{A}} \\ -P^{\perp 1}_{\text{A}} \\ P^{\perp 2}_{\text{A}} \end{pmatrix}, \tag{30b}$$

and the same equations on the B sublattice. Just like in the single-ion problem, the $M^{\perp 1}_{\boldsymbol{\pi}}$ and $P^{\perp 2}_{\boldsymbol{\pi}}$ belong to the same irreducible representation, as well as the $M^{\perp 2}_{\boldsymbol{\pi}}$ and $P^{\perp 1}_{\boldsymbol{\pi}}$. The matrix elements are therefore real or imaginary, and the product of the magnetization and polarization matrix elements in the ME susceptibility is real.

Although the symmetry classification obtained above did not consider the DM interaction, it describes the selection rules obtained from the exact diagonalization. This is because the DM interaction is compatible with the $D_2(C_2)$ magnetic point group considered above.

B. Perturbative effects of the exchange coupling

So far, we have neglected the interactions between the Co spins. To assess how much the single-ion picture is altered, we take into account the effect of exchange couplings perturbatively: starting from the single-ion limit, $J = J_z = D_z = 0$ in Eq. (2), we derive a tight-binding-like approximation for the exchange part. We denote the onsite and exchange parts as $\mathcal{H}^0$ and $\mathcal{H}'$.

For the noninteracting case, the ground state of $\mathcal{H}^0$ is

$$\left|\Psi^0_1\right\rangle = \prod_j \left|\psi^{(-i)}_1(j)\right\rangle, \tag{31}$$

where j runs over both the A and B sublattice sites. We define the local single-ion excitation at site l as

$$\left|\Psi^0_2(l)\right\rangle = \left|\psi^{(+i)}_2(l)\right\rangle \prod_{j\neq l} \left|\psi^{(-i)}_1(j)\right\rangle. \tag{32}$$

The local wave functions $|\psi^{(\pm i)}_\alpha(l)\rangle$ are given by Eq. (B2). If the number of (all) sites is N, the noninteracting ground-state energy is $E^0_1 = N\varepsilon_1$ and the excited states $|\Psi^0_2(l)\rangle$ have energies $E^0_2 = (N-1)\varepsilon_1 + \varepsilon_2$ and are N-fold degenerate.

In order to calculate the degeneracy lifting in the first order of the degenerate perturbation expansion, we need to diagonalize the perturbing matrix $\mathcal{H}'$ on the subspace spanned by $|\Psi^0_2(l)\rangle$,

$$\left\langle\Psi^0_2(l')\middle|\mathcal{H}'\middle|\Psi^0_2(l)\right\rangle, \tag{33}$$

describing a local excited state which hops with equal amplitudes in different directions. Generally, the hopping problem is diagonalized in the momentum space for a translationally symmetric problem. In our case, the translational symmetry holds for the unit cell containing two lattice sites, with translation vectors $\mathbf{t}'_1 = (1,1,0)$ and $\mathbf{t}'_2 = (1,-1,0)$ in the (x,y,z) coordinate system (see Fig. 1). However, the $\{C^{\parallel}_2|[\frac{1}{2}00]\}$ screw axis and the $\mathbf{t}'_1$ and/or $\mathbf{t}'_2$ translation generate an Abelian group isomorphic to the group constructed from the $\mathbf{t}_1 = (1,0,0)$ and $\mathbf{t}_2 = (0,1,0)$, the translations of the lattice of the Co ions, if we neglect the alternating tetrahedra. The irreducible representations are all one dimensional, with

$$\left\{C^{\parallel}_2\middle|\left[\tfrac{1}{2}00\right]\right\}|\Psi_{\mathbf{k}}\rangle = e^{i\mathbf{k}\cdot\mathbf{t}_1}|\Psi_{\mathbf{k}}\rangle, \tag{34}$$

where $\mathbf{k}$ plays the role of the momentum. As a result, the $\mathbf{k} = (0,0) = \mathbf{0}$ and $\mathbf{k} = (\pi,\pi) = \boldsymbol{\pi}$ states (which, in fact, are both at the Γ point of the Brillouin zone of the lattice defined by the proper translations $\mathbf{t}'_1$ and $\mathbf{t}'_2$) are realized by the following linear combinations:

$$\left|\Psi^0_{2,\mathbf{0}}\right\rangle = \frac{1}{\sqrt{N}}\left(\sum_{j\in A}\left|\Psi^0_2(l)\right\rangle + C^{\parallel}_2 \sum_{j\in B}\left|\Psi^0_2(l)\right\rangle\right),$$

$$\left|\Psi^0_{2,\boldsymbol{\pi}}\right\rangle = \frac{1}{\sqrt{N}}\left(\sum_{j\in A}\left|\Psi^0_2(l)\right\rangle - C^{\parallel}_2 \sum_{j\in B}\left|\Psi^0_2(l)\right\rangle\right). \tag{35}$$

Then, the energies of the excitations are

$$\begin{aligned}\omega^{1\to 2}_{\mathbf{k}} &= E^{(1)}_{\mathbf{k},2} - E^{(1)} \\ &= \left\langle\Psi^0_{2,\mathbf{k}}\middle|\mathcal{H}\middle|\Psi^0_{2,\mathbf{k}}\right\rangle - \left\langle\Psi^0_1\middle|\mathcal{H}\middle|\Psi^0_1\right\rangle.\end{aligned} \tag{36}$$

The evaluation of the expectation values using the single-ion wave functions (B2) is straightforward but tedious.

Keeping only the first-order terms of the perturbation and doing series expansion we get, in the strong magnetic field limit $h \gg \Lambda \gg J, J_z$, and $D_z = 0$,

$$\omega^{1\to 2}_{\mathbf{0}} = h + \Lambda - 9J - 3J_z, \tag{37a}$$

$$\omega^{1\to 2}_{\boldsymbol{\pi}} = h + \Lambda - 3J + 3J_z. \tag{37b}$$

The perturbative approach works well for the experimentally studied paramagnetic case in the high-field limit. In Sec. VII A 2 we have seen that only the $\boldsymbol{\pi}$ modes absorb in Faraday geometry. In the exact diagonalization, we observed the strongest absorption is for the $\omega_{\boldsymbol{\pi}}^{1\to 2}$ mode. This is not surprising, as this is the single-magnon mode in the weak anisotropy limit $\Lambda \ll J, J_z$. In the single-ion model without anisotropy $J, J_z, \Lambda = 0$, it is just the paramagnetic mode with $\omega_{\boldsymbol{\pi}}^{1\to 2} = h$, as it can be inferred from Eq. (37b). More interestingly, the energy of this mode is very close to the single-ion excitation energy $\omega^{1\to 2} = \varepsilon_2 - \varepsilon_1$ [see Eq. (B6)]. The difference is just $3(J - J_z)$ and vanishes for $J = J_z$. This explains why the single-ion model works remarkably well for large magnetic fields $h \gg \Lambda, J, J_z$, as seen from the comparison of the minimal theory and the experiments in Fig. 6.

In the strong single-ion anisotropy limit $\Lambda \gg h, J, J_z$, the energies of these modes are

$$\omega_{\mathbf{0}}^{1\to 2} = 2h - 12J - J_z, \tag{38a}$$

$$\omega_{\boldsymbol{\pi}}^{1\to 2} = 2h - 4J + J_z. \tag{38b}$$

The deviation of $\omega_{\boldsymbol{\pi}}^{1\to 2}$ in the single-ion model becomes noticeable compared to the strong field limit given by Eq. (37b), $-4J + J_z$ vs $-3J + 3J_z$, but still not too large as compared to the deviations of other modes, say Eq. (38a).

VIII. SUMMARY

The coupling of the magnetic moments and electric polarization in a material is responsible for many interesting optical phenomena which happen at low temperatures, usually in the ordered phases. Here, we studied the optical response of a multiferroic material in the paramagnetic phase, at temperatures much higher than the ordering temperature.

We observed MChD for the excitations of the $S = \frac{3}{2}$ spin of the Co^{2+} ion in $Sr_2CoSi_2O_7$ at temperatures up to 100 K, although the magnetic ordering temperature is only $T_N = 7$ K. The main experimental findings, the temperature dependence of the spin-mode frequencies, their intensities, and the sign of the MChD for the different spin modes, are captured well by the exact diagonalization of a four-spin cluster.

The numerical results are interpreted in a simple analytical model of a single spin with an easy-plane anisotropy in an external magnetic field, and its coupling to the THz radiation via magnetization $\mathbf{M}$ and via polarization $\mathbf{P}$, expressed by spin-quadrupolar terms. Finite ME susceptibility arises if the components of the $\mathbf{M}$ and $\mathbf{P}$ transform according to the same irreducible representation of the symmetry group compatible with both, the oxygen tetrahedron around the magnetic ion and the applied magnetic field. Figure 6 shows that in high fields and low temperatures ($\varepsilon_2 - \varepsilon_1 > k_B T$) the NDD spectrum is dominated by the magnetic dipolar transition from the ground state $|1\rangle \to |2\rangle$. By increasing T, another magnetic dipolar transition from the thermally excited state $|2\rangle \to |3\rangle$ appears in the NDD spectrum. Our exact diagonalization calculation showed that the $|2\rangle \to |3\rangle$ peak is very close to the $|1\rangle \to |2\rangle$ in energy and due to the line-broadening effects only a single broad peak is observed. This coincides with the experimental finding at high temperatures, as exemplified in Figs. 2(a) and 2(b).

By considering the real material where the the oxygen tetrahedra are tilted, we showed how the selection rules of the single-ion model are modified when the exchange coupling is turned on, in agreement with the results of the exact diagonalization. Finally, we demonstrated that the exchange correlations are important to accurately describe the mode frequencies in the paramagnetic state.

In conclusion, we demonstrated that MChD can arise in the paramagnetic phase of a noncentrosymmetric material. Furthermore, we presented a detailed theoretical analysis of spin excitations in $Sr_2CoSi_2O_7$ which helps to identify the key parameters responsible for high-temperature NDD both in the chiral and toroidal cases.

ACKNOWLEDGMENTS

This research was supported by the Estonian Ministry of Education and Research with institutional research funding IUT23-3, by the European Regional Development Fund Project No. TK134, by the bilateral program of the Estonian and Hungarian Academies of Sciences under the Contract No. SNK-64/2013, by the Hungarian NKFIH Grants No. K 124176 and No. ANN 122879, by the BME-Nanonotechnology and Materials Science FIKP grant of EMMI (BME FIKP-NAT), by the FWF Austrian Science Fund No. I 2816-N27, and by the Deutsche Forschungsgemeinschaft (DFG) via the Transregional Research Collaboration TRR 80: From Electronic Correlations to Functionality (Augsburg-Munich-Stuttgart) We acknowledge the support of the HFML-RU/FOM, member of the European Magnetic Field Laboratory (EMFL). V.K. gratefully acknowledges support from RIKEN's FY 2016 Incentive Research Projects.

V.K. and Y. Tokunaga grew the crystals, D.G.F., D.Sz., V.K., J.V. and U.N. conducted THz spectroscopy experiments in Tallinn and analyzed the results, D.G.F., D.Sz., B.B. and D.L.K. conducted high magnetic field measurement in Nijmegen, P.B. and K.P. developed the theory, T.R., S.B., P.B., and K.P. wrote the manuscript, D.Sz. and K.P. conceived the project. Every author contributed to the discussion of the results.

APPENDIX A: REALITY OF THE MATRIX ELEMENTS IN A MAGNETIC POINT GROUP

We analyze the case of $\varphi = 0$, which is relevant for the experimental situation and is conceptually the simplest. The symmetry group of this configuration considering both the spin Hamiltonian (14) and the oxygen tetrahedron around the Co^{2+} ion, manifested by the spin-polarization coupling (15), is

$$D_2(C_2) = \left\{\mathbf{1}, C_2^{\parallel}, \Theta C_2^{\perp 1}, \Theta C_2^{\perp 2}\right\}, \tag{A1}$$

with operators in the field-fixed coordinate frame (Fig. 5). Since the inversion, the mirror plane, and the rotoreflection symmetry are absent, the case is termed as chiral. The $D_2(C_2)$ group is generated by the symmetry elements $C_2^{\parallel}$ and $\Theta C_2^{\perp 2}$, and its character table together with the symmetry classification of spin and polarization components is summarized in Table III. We note that our conclusions are equally valid for the $\varphi = \pi/4$ case, where $\Theta C_2^{\perp 2}$ is also present in the corresponding polar symmetry group $C_{2v}(C_{1h})$.

The operator $C_2^{\perp 2}$ is represented on the $S = \frac{3}{2}$ spin space by the matrix

$$\hat{C}_2^{\perp 2} = e^{i\pi \hat{S}^{\perp 2}} = \begin{pmatrix} 0 & 0 & 0 & 1 \\ 0 & 0 & -1 & 0 \\ 0 & 1 & 0 & 0 \\ -1 & 0 & 0 & 0 \end{pmatrix}. \tag{A2}$$

The time-reversal operation Θ is conveniently represented by the antiunitary operation

$$\hat{\Theta} = \hat{C}_2^{\perp 2}\mathcal{K} = e^{i\pi \hat{S}^{\perp 2}}\mathcal{K} = \begin{pmatrix} 0 & 0 & 0 & 1 \\ 0 & 0 & -1 & 0 \\ 0 & 1 & 0 & 0 \\ -1 & 0 & 0 & 0 \end{pmatrix}\mathcal{K}, \tag{A3}$$

where $\mathcal{K}$ is the complex conjugation, conjugating every matrix or vector component on the right, but leaving the basis functions intact [31]. This is analogous to the $S = \frac{1}{2}$ case where Θ is expressed with the help of the Pauli matrix $\hat{\sigma}^y$ as $\hat{\Theta} = i\hat{\sigma}^y\mathcal{K}$. Collecting all this together, the operator for $\Theta C_2^{\perp 2}$ in the Hilbert space reads as

$$\hat{\Theta}\hat{C}_2^{\perp 2} = \hat{C}_2^{\perp 2}\mathcal{K}\hat{C}_2^{\perp 2} = e^{i2\pi \hat{S}^{\perp 2}}\mathcal{K} = -\hat{\mathbf{1}}\mathcal{K}. \tag{A4}$$

When we consider the effect of this symmetry on the matrix elements of physical observables, we find first all representations of $\Theta C_2^{\perp 2}$ are $+1$ or -1 as given in Table III for the chiral and polar cases, respectively. Therefore, any linear operator $\mathcal{O}$, such as the spin or polarization components, is either even or odd, i.e., it transforms as

$$\Theta C_2^{\perp 2}(\mathcal{O}) = \pm\mathcal{O}, \tag{A5}$$

or in matrix representation

$$\left(\hat{\Theta}\hat{C}_2^{\perp 2}\right)\hat{\mathcal{O}}\left(\hat{\Theta}\hat{C}_2^{\perp 2}\right)^{-1} = \pm\hat{\mathcal{O}}. \tag{A6}$$

Next, following Eq. (A4), let us evaluate the left-hand side of the equation above:

$$\left(\hat{\Theta}\hat{C}_2^{\perp 2}\right)\hat{\mathcal{O}}\left(\hat{\Theta}\hat{C}_2^{\perp 2}\right)^{-1} = \mathcal{K}\hat{\mathcal{O}}\mathcal{K} = \hat{\mathcal{O}}^*, \tag{A7}$$

where the last equality follows from the fact that acting on an arbitrary vector v, $\mathcal{K}\hat{\mathcal{O}}\mathcal{K}v = \mathcal{K}\hat{\mathcal{O}}v^* = \hat{\mathcal{O}}^*v$. Equations (A6) and (A7) together mean that

$$\hat{\mathcal{O}}^* = \pm\hat{\mathcal{O}}. \tag{A8}$$

This restricts the matrix elements of the operators even under $\Theta C_2^{\perp 2}$ to be real, and the matrix elements of the odd operators to be pure imaginary.

In conclusion, the unitary symmetries determine the selection rules, i.e., the nonvanishing matrix elements, whereas antiunitary elements give constraints on the reality of them. These rules and the matrix elements given in Appendix B (and calculated by using the explicit wave functions) are in full agreement.

APPENDIX B: SOLUTION OF THE SINGLE-ION PROBLEM

1. Energies and wave functions

The energies in increasing order are

$$\varepsilon_1^{(-i)} = -\frac{h}{2} + \frac{5\Lambda}{4} - \sqrt{h^2 + h\Lambda + \Lambda^2}, \tag{B1a}$$

$$\varepsilon_2^{(+i)} = \frac{h}{2} + \frac{5\Lambda}{4} - \sqrt{h^2 - h\Lambda + \Lambda^2}, \tag{B1b}$$

$$\varepsilon_3^{(-i)} = -\frac{h}{2} + \frac{5\Lambda}{4} + \sqrt{h^2 + h\Lambda + \Lambda^2}, \tag{B1c}$$

$$\varepsilon_4^{(+i)} = \frac{h}{2} + \frac{5\Lambda}{4} + \sqrt{h^2 - gh\Lambda + \Lambda^2}, \tag{B1d}$$

and the corresponding unnormalized eigenstates are

$$\left|\psi_1^{(-i)}\right\rangle \propto \left(2h + \Lambda + 2\sqrt{h^2 + h\Lambda + \Lambda^2}\right)|\Uparrow\rangle + \sqrt{3}\Lambda|\downarrow\rangle, \tag{B2a}$$

$$\left|\psi_2^{(+i)}\right\rangle \propto \left(2h - \Lambda + 2\sqrt{h^2 - h\Lambda + \Lambda^2}\right)|\uparrow\rangle + \sqrt{3}\Lambda|\Downarrow\rangle, \tag{B2b}$$

$$\left|\psi_3^{(-i)}\right\rangle \propto \left(2h + \Lambda + 2\sqrt{h^2 + h\Lambda + \Lambda^2}\right)|\downarrow\rangle - \sqrt{3}\Lambda|\Uparrow\rangle, \tag{B2c}$$

$$\left|\psi_4^{(+i)}\right\rangle \propto \left(2h - \Lambda + 2\sqrt{h^2 - h\Lambda + \Lambda^2}\right)|\Downarrow\rangle - \sqrt{3}\Lambda|\uparrow\rangle. \tag{B2d}$$

The phases for the eigenvectors above are chosen in such a way that we recover the basis $\{|\Uparrow\rangle, |\uparrow\rangle, |\downarrow\rangle, |\Downarrow\rangle\}$ for $h \gg \Lambda$, e.g., $|\psi_1^{(-i)}\rangle \rightarrow |\Uparrow\rangle$, and so on.

2. Large anisotropy and small field: $\Lambda \gg h$

From the series expansion of the single-spin energies (B1) in h/Λ, we get

$$\varepsilon_1 = \frac{\Lambda}{4} - h - \frac{3h^2}{8\Lambda} + \cdots, \tag{B3a}$$

$$\varepsilon_2 = \frac{\Lambda}{4} + h - \frac{3h^2}{8\Lambda} + \cdots, \tag{B3b}$$

$$\varepsilon_3 = \frac{9\Lambda}{4} + \frac{3h^2}{8\Lambda} + \cdots, \tag{B3c}$$

$$\varepsilon_4 = \frac{9\Lambda}{4} + \frac{3h^2}{8\Lambda} + \cdots. \tag{B3d}$$

The spin and polarization operators in leading order of h/Λ are in the matrix representation

$$\hat{S}^{\parallel} = \begin{pmatrix} 1 & 0 & -\frac{\sqrt{3}}{2} & 0 \\ 0 & -1 & 0 & -\frac{\sqrt{3}}{2} \\ -\frac{\sqrt{3}}{2} & 0 & \frac{9h^2}{16\Lambda^2} & 0 \\ 0 & -\frac{\sqrt{3}}{2} & 0 & -\frac{9h^2}{16\Lambda^2} \end{pmatrix}, \tag{B4a}$$

$$\hat{S}^{\perp 1} = \begin{pmatrix} 0 & 1 & 0 & -\frac{\sqrt{3}}{2} \\ 1 & 0 & \frac{\sqrt{3}}{2} & 0 \\ 0 & \frac{\sqrt{3}}{2} & 0 & \frac{9h^2}{16\Lambda^2} \\ -\frac{\sqrt{3}}{2} & 0 & \frac{9h^2}{16\Lambda^2} & 0 \end{pmatrix}, \tag{B4b}$$

$$\hat{S}^{\perp 2} = i\begin{pmatrix} 0 & -\frac{1}{2} & 0 & \frac{\sqrt{3}h}{4\Lambda} \\ \frac{1}{2} & 0 & -\frac{\sqrt{3}h}{4\Lambda} & 0 \\ 0 & \frac{\sqrt{3}h}{4\Lambda} & 0 & -\frac{3}{2} \\ -\frac{\sqrt{3}h}{4\Lambda} & 0 & \frac{3}{2} & 0 \end{pmatrix}, \tag{B4c}$$

$$\hat{P}^{\parallel}_{\text{chiral}} = -\hat{P}^{\perp 1}_{\text{polar}} = i\begin{pmatrix} 0 & 0 & -\sqrt{3} & 0 \\ 0 & 0 & 0 & -\sqrt{3} \\ \sqrt{3} & 0 & 0 & 0 \\ 0 & \sqrt{3} & 0 & 0 \end{pmatrix}, \tag{B5a}$$

$$\hat{P}^{\parallel}_{\text{polar}} = \hat{P}^{\perp 1}_{\text{chiral}} = i\begin{pmatrix} 0 & -\frac{3h}{2\Lambda} & 0 & \sqrt{3} \\ \frac{3h}{2\Lambda} & 0 & -\sqrt{3} & 0 \\ 0 & \sqrt{3} & 0 & \frac{3h}{2\Lambda} \\ -\sqrt{3} & 0 & -\frac{3h}{2\Lambda} & 0 \end{pmatrix}, \tag{B5b}$$

$$\hat{P}^{\perp 2}_{\text{chiral}} = \begin{pmatrix} 0 & \frac{3h}{2\Lambda} & 0 & -\sqrt{3} \\ \frac{3h}{2\Lambda} & 0 & -\sqrt{3} & 0 \\ 0 & -\sqrt{3} & 0 & -\frac{3h}{2\Lambda} \\ -\sqrt{3} & 0 & -\frac{3h}{2\Lambda} & 0 \end{pmatrix}, \tag{B5c}$$

$$\hat{P}^{\perp 2}_{\text{polar}} = \begin{pmatrix} \frac{3h}{2\Lambda} & 0 & -\sqrt{3} & 0 \\ 0 & -\frac{3h}{2\Lambda} & 0 & \sqrt{3} \\ -\sqrt{3} & 0 & -\frac{3h}{2\Lambda} & 0 \\ 0 & \sqrt{3} & 0 & \frac{3h}{2\Lambda} \end{pmatrix}. \tag{B5d}$$

3. Large field and small anisotropy: $h \gg \Lambda$

The energies are

$$\varepsilon_1 = -\frac{3h}{2} + \frac{3\Lambda}{4} - \frac{3\Lambda^2}{8h} + \cdots, \tag{B6a}$$

$$\varepsilon_2 = -\frac{h}{2} + \frac{7\Lambda}{4} - \frac{3\Lambda^2}{8h} + \cdots, \tag{B6b}$$

$$\varepsilon_3 = \frac{h}{2} + \frac{7\Lambda}{4} + \frac{3\Lambda^2}{8h} + \cdots, \tag{B6c}$$

$$\varepsilon_4 = \frac{3h}{2} + \frac{3\Lambda}{4} + \frac{3\Lambda^2}{8h} + \cdots. \tag{B6d}$$

The spin and polarization operators in the leading order of Λ/h are in the matrix representation

$$\hat{S}^{\parallel} = \begin{pmatrix} \frac{3}{2} & 0 & -\frac{\sqrt{3}\Lambda}{2h} & 0 \\ 0 & \frac{1}{2} & 0 & -\frac{\sqrt{3}\Lambda}{2h} \\ -\frac{\sqrt{3}\Lambda}{2h} & 0 & -\frac{1}{2} & 0 \\ 0 & -\frac{\sqrt{3}\Lambda}{2h} & 0 & -\frac{3}{2} \end{pmatrix}, \tag{B7a}$$

$$\hat{S}^{\perp 1} = \begin{pmatrix} 0 & \frac{\sqrt{3}}{2} & 0 & -\frac{9\Lambda^2}{16h^2} \\ \frac{\sqrt{3}}{2} & 0 & 1 & 0 \\ 0 & 1 & 0 & \frac{\sqrt{3}}{2} \\ -\frac{9\Lambda^2}{16h^2} & 0 & \frac{\sqrt{3}}{2} & 0 \end{pmatrix}, \tag{B7b}$$

$$\hat{S}^{\perp 2} = i\begin{pmatrix} 0 & -\frac{\sqrt{3}}{2} & 0 & \frac{3\Lambda^2}{16h^2} \\ \frac{\sqrt{3}}{2} & 0 & -1 & 0 \\ 0 & 1 & 0 & -\frac{\sqrt{3}}{2} \\ -\frac{3\Lambda^2}{16h^2} & 0 & \frac{\sqrt{3}}{2} & 0 \end{pmatrix}, \tag{B7c}$$

$$\hat{P}^{\parallel}_{\text{chiral}} = -\hat{P}^{\perp 1}_{\text{polar}} = i\begin{pmatrix} 0 & 0 & -\sqrt{3} & 0 \\ 0 & 0 & 0 & -\sqrt{3} \\ \sqrt{3} & 0 & 0 & 0 \\ 0 & \sqrt{3} & 0 & 0 \end{pmatrix}, \tag{B8a}$$

$$\hat{P}^{\parallel}_{\text{polar}} = \hat{P}^{\perp 1}_{\text{chiral}} = i\begin{pmatrix} 0 & -\sqrt{3} & 0 & \frac{3\Lambda}{2h} \\ \sqrt{3} & 0 & -\frac{3\Lambda}{2h} & 0 \\ 0 & \frac{3\Lambda}{2h} & 0 & \sqrt{3} \\ -\frac{3\Lambda}{2h} & 0 & -\sqrt{3} & 0 \end{pmatrix}, \tag{B8b}$$

$$\hat{P}^{\perp 2}_{\text{chiral}} = \begin{pmatrix} 0 & \sqrt{3} & 0 & -\frac{3\Lambda}{2h} \\ \sqrt{3} & 0 & -\frac{3\Lambda}{2h} & 0 \\ 0 & -\frac{3\Lambda}{2h} & 0 & -\sqrt{3} \\ -\frac{3\Lambda}{2h} & 0 & -\sqrt{3} & 0 \end{pmatrix}, \tag{B8c}$$

$$\hat{P}^{\perp 2}_{\text{polar}} = \begin{pmatrix} \frac{3}{2} & 0 & -\frac{\sqrt{3}}{2} & 0 \\ 0 & -\frac{3}{2} & 0 & -\frac{\sqrt{3}}{2} \\ -\frac{\sqrt{3}}{2} & 0 & -\frac{3}{2} & 0 \\ 0 & -\frac{\sqrt{3}}{2} & 0 & \frac{3}{2} \end{pmatrix}. \tag{B8d}$$

---

[1] L. Barron, *Molecular Light Scattering and Optical Activity* (Cambridge University Press, Cambridge, 2009).

[2] J. J. Hopfield and D. G. Thomas, Phys. Rev. Lett. **4**, 357 (1960).

[3] G. L. J. A. Rikken and E. Raupach, Nature (London) **390**, 493 (1997).

[4] G. L. J. A. Rikken, C. Strohm, and P. Wyder, Phys. Rev. Lett. **89**, 133005 (2002).

[5] D. Szaller, S. Bordács, and I. Kézsmárki, Phys. Rev. B **87**, 014421 (2013).

[6] I. Kézsmárki, N. Kida, H. Murakawa, S. Bordács, Y. Onose, and Y. Tokura, Phys. Rev. Lett. **106**, 057403 (2011).

[7] S. Bordács, I. Kézsmárki, D. Szaller, L. Demkó, N. Kida, H. Murakawa, Y. Onose, R. Shimano, T. Rõõm, U. Nagel, S. Miyahara, N. Furukawa, and Y. Tokura, Nat. Phys. **8**, 734 (2012).

[8] Y. Takahashi, R. Shimano, Y. Kaneko, H. Murakawa, and Y. Tokura, Nat. Phys. **8**, 121 (2012).

[9] Y. Takahashi, Y. Yamasaki, and Y. Tokura, Phys. Rev. Lett. **111**, 037204 (2013).

[10] I. Kézsmárki, D. Szaller, S. Bordács, V. Kocsis, Y. Tokunaga, Y. Taguchi, H. Murakawa, Y. Tokura, H. Engelkamp, T. Rõõm, and U. Nagel, Nat. Commun. **5**, 3203 (2014).

[11] A. M. Kuzmenko, V. Dziom, A. Shuvaev, A. Pimenov, M. Schiebl, A. A. Mukhin, V. Y. Ivanov, I. A. Gudim, L. N. Bezmaternykh, and A. Pimenov, Phys. Rev. B **92**, 184409 (2015).

[12] I. Kézsmárki, U. Nagel, S. Bordács, R. S. Fishman, J. H. Lee, H. T. Yi, S.-W. Cheong, and T. Rõõm, Phys. Rev. Lett. **115**, 127203 (2015).

[13] D. Szaller, S. Bordács, V. Kocsis, T. Rõõm, U. Nagel, and I. Kézsmárki, Phys. Rev. B **89**, 184419 (2014).

[14] A. M. Kuzmenko, D. Szaller, T. Kain, V. Dziom, L. Weymann, A. Shuvaev, A. Pimenov, A. A. Mukhin, V. Y. Ivanov, I. A. Gudim, L. N. Bezmaternykh, and A. Pimenov, Phys. Rev. Lett. **120**, 027203 (2018).

[15] V. Kocsis, K. Penc, T. Rõõm, U. Nagel, J. Vít, J. Romhányi, Y. Tokunaga, Y. Taguchi, Y. Tokura, I. Kézsmárki, and S. Bordács, Phys. Rev. Lett. **121**, 057601 (2018).

[16] M. Akaki, H. Iwamoto, T. Kihara, M. Tokunaga, and H. Kuwahara, Phys. Rev. B **86**, 060413 (2012).

[17] M. Akaki, T. Tadokoro, T. Kihara, M. Tokunaga, and H. Kuwahara, J. Low Temp. Phys. **170**, 291 (2013).

[18] S. Yu, B. Gao, J. W. Kim, S.-W. Cheong, M. K. L. Man, J. Madéo, K. M. Dani, and D. Talbayev, Phys. Rev. Lett. **120**, 037601 (2018).

[19] H. Murakawa, Y. Onose, S. Miyahara, N. Furukawa, and Y. Tokura, Phys. Rev. Lett. **105**, 137202 (2010).

[20] K. Penc, J. Romhányi, T. Rõõm, U. Nagel, A. Antal, T. Fehér, A. Jánossy, H. Engelkamp, H. Murakawa, Y. Tokura, D. Szaller, S. Bordács, and I. Kézsmárki, Phys. Rev. Lett. **108**, 257203 (2012).

[21] M. Soda, M. Matsumoto, M. Månsson, S. Ohira-Kawamura, K. Nakajima, R. Shiina, and T. Masuda, Phys. Rev. Lett. **112**, 127205 (2014).

[22] J. Romhányi, M. Lajkó, and K. Penc, Phys. Rev. B **84**, 224419 (2011).

[23] T. Arima, J. Phys. Soc. Jpn. **76**, 073702 (2007).

[24] S. Miyahara and N. Furukawa, J. Phys. Soc. Jpn. **80**, 073708 (2011).

[25] K. Yamauchi, P. Barone, and S. Picozzi, Phys. Rev. B **84**, 165137 (2011).

[26] The absorption is given by

$$\alpha^{\pm}(\omega) = \frac{2\omega}{c_0}\mathrm{Im}\mathcal{N}_{\pm}(\omega),$$

where the complex index of refraction $\mathcal{N}_{\pm}$ for the $\pm k$ direction of light propagation is

$$\mathcal{N}_{\pm}(\omega) = \sqrt{\left[\epsilon_{\nu\nu} + \chi^{ee}_{\nu\nu}(\omega)\right]\left[\mu_{\mu\mu} + \chi^{mm}_{\mu\mu}(\omega)\right]} \pm \chi^{me}_{\mu\nu}(\omega),$$

where $\chi^{me}_{\mu\nu}(\omega)$ is the time-reversal odd part of the ME susceptibility. $\epsilon_{\nu\nu}$ and $\mu_{\mu\mu}$ are real background dielectric permittivity and magnetic permeability, respectively, not originating from the spin system. In the limit of a small spin contribution to the susceptibilities, $\chi^{ee}_{\nu\nu}(\omega) \ll \epsilon_{\nu\nu}$, $\chi^{mm}_{\mu\mu}(\omega) \ll \mu_{\mu\mu}$, index of refraction is

$$\mathcal{N}_{\pm}(\omega) \approx \sqrt{\epsilon_{\nu\nu}\mu_{\mu\mu}} + \frac{\sqrt{\mu_{\mu\mu}}}{2\sqrt{\epsilon_{\nu\nu}}}\chi^{ee}_{\nu\nu}(\omega) + \frac{\sqrt{\epsilon_{\nu\nu}}}{2\sqrt{\mu_{\mu\mu}}}\chi^{mm}_{\mu\mu}(\omega) \pm \chi^{me}_{\mu\nu}(\omega).$$

[27] Since the $S = \frac{3}{2}$ has four states, the dimension of the Hilbert space of the four-spin cluster is $4^4 = 256$, and the sums in Eqs. (8) and (9) run over $256^2 = 65536$ terms. Even though the cluster is small, it already provided sufficient information to compare with the experimental data at high temperatures and fields.

[28] L. Barron and J. Vrbancich, Mol. Phys. **51**, 715 (1984).

[29] M. Akaki, D. Yoshizawa, A. Okutani, T. Kida, J. Romhányi, K. Penc, and M. Hagiwara, Phys. Rev. B **96**, 214406 (2017).

[30] S. Altmann and P. Herzig, *Point-group Theory Tables*, Oxford Science Publications (Clarendon, Oxford, 1994).

[31] J. Sakurai and J. Napolitano, *Modern Quantum Mechanics* (Addison-Wesley, Boston, 2011).

Appendix 3

III

V. Kocsis, S. Bordács, Y. Tokunaga, J. Viirok, L. Peedu, T. Rõõm, U. Nagel, Y. Taguchi, Y. Tokura, and I. Kézsmárki. Magnetoelectric spectroscopy of spin excitations in $LiCoPO_4$. *Phys. Rev. B*, 100:155124, Oct 2019.

PHYSICAL REVIEW B **100**, 155124 (2019)

Editors' Suggestion

Magnetoelectric spectroscopy of spin excitations in $LiCoPO_4$

V. Kocsis,[1,2] S. Bordács,[2,3] Y. Tokunaga,[1,4] J. Viirok,[5] L. Peedu,[5] T. Rõõm,[5] U. Nagel,[5]
Y. Taguchi,[1] Y. Tokura,[1,6] and I. Kézsmárki[2,7]

[1] *RIKEN Center for Emergent Matter Science, Wako, Saitama 351-0198, Japan*
[2] *Department of Physics, Budapest University of Technology and Economics and MTA-BME Lendület Magneto-optical Spectroscopy Research Group, 1111 Budapest, Hungary*
[3] *Hungarian Academy of Sciences, Premium Postdoctor Program, 1051 Budapest, Hungary*
[4] *Department of Advanced Materials Science, University of Tokyo, Kashiwa 277-8561, Japan*
[5] *National Institute of Chemical Physics and Biophysics, Akadeemia tee 23, 12618, Tallinn, Estonia*
[6] *Department of Applied Physics and Tokyo College, University of Tokyo, Hongo, Tokyo 113-8656, Japan*
[7] *Experimental Physics 5, Center for Electronic Correlations and Magnetism, Institute of Physics, University of Augsburg, 86159 Augsburg, Germany*

(Received 25 July 2019; published 14 October 2019)

We have studied spin excitations in a single-domain crystal of antiferromagnetic $LiCoPO_4$ by terahertz absorption spectroscopy. By analyzing the selection rules and comparing the strengths of the absorption peaks in the different antiferromagnetic domains, we found electromagnons and magnetoelectric (ME) spin resonances in addition to conventional magnetic dipole active spin-wave excitations. Using the sum rule for the ME susceptibility, we determined the contribution of the spin excitations to all the different off-diagonal elements of the static ME susceptibility tensor in zero and finite magnetic fields. We conclude that the ME spin resonances are responsible for the static ME response of the bulk when the magnetic field is along the x axis, and the symmetric part of the ME tensor with zero diagonal elements dominates over the antisymmetric components.

DOI: 10.1103/PhysRevB.100.155124

I. INTRODUCTION

The magnetoelectric (ME) effect is the cross induction of polarization and magnetization by magnetic and electric field, respectively, as described by the ME tensor forms, $P_\mu = \chi_{\mu\nu}H_\nu$ and $\mu_0 M_\mu = \chi^{\mathrm{T}}_{\mu\nu}E_\nu$, where P_μ (M_μ) and H_ν (E_ν) are the $\mu, \nu = x, y, z$ components of the electric polarization (magnetic dipole moment) and the magnetic (electric) field. The ME effect is often associated with complex magnetic order parameters [1,2], such as the ferrotoroidal [3–8] and ferroquadrupolar moments [9], and magnetically induced chirality [10]. The ME effect provides a handle to manipulate these exotic spin orders and the corresponding magnetic domains even in the absence of spontaneous electric polarization or magnetization; thus, such ME materials have been proposed as building blocks for novel data storage and memory devices [11–13]. In some cases, such spin-multipolar orders have been revealed successfully by spherical neutron polarimetry [5,14] and x-ray spectroscopy [15] and investigated indirectly using static ME measurements [4,6,7,16] and second-harmonic generation microscopy [3,17,18].

In this work, we exploit a different approach to assign ferrotoroidal and ferroquadrupolar orders which is based on the measurement of the optical ME effect [8,19,20] using terahertz (THz) absorption spectroscopy. In a ME medium counterpropagating light beams can experience different indices of refraction, exhibiting optical directional anisotropy (ODA), as schematically shown in Fig. 1(b). This compelling phenomenon can be used to measure the dynamic ME response, also known as the optical ME effect, e.g., in resonance with magnon modes at THz frequencies. From the spectrum of the dynamic ME effect one can also determine the static ME coupling via the ME susceptibility sum rule [21]. Furthermore, THz absorption spectroscopy can measure the ME domain population as it has been successfully utilized to distinguish between the two types of antiferromagnetic (AFM) domains of $LiCoPO_4$ [13] [see Fig. 1(b)]. Here, in the case of $LiCoPO_4$, we demonstrate that the ODA can also be used to investigate the form and the spectral dependence of the ME susceptibility tensor and hence to identify different spin-multipolar orders responsible for the ME effect.

II. ADVANTAGE OF OPTICAL OVER STATIC ME EXPERIMENTS

When the ME phase appears upon a second-order phase transition from a high-temperature centrosymmetric and paramagnetic phase, the ME domains (α and β) connected by the spatial inversion and the time-reversal symmetries have ME susceptibilities of opposite signs, $\hat{\chi}^\alpha = -\hat{\chi}^\beta$. In the absence of electric (E) and magnetic (H) fields, a multidomain state is often realized, and the ME effect is canceled on the macroscopic scale. When a material possesses ferroelectricity or ferromagnetism, the P or M domain with an order parameter parallel to the conjugate electric (E^0) or magnetic (H^0) field is selected, respectively. However, when staggered electric and magnetic dipole orders or higher-order magnetic multipoles give rise to the ME effect, such direct control is not possible. Instead, a single ME domain can be selected by the simultaneous application of E^0 and H^0 fields upon cooling a sample

©2019 American Physical Society

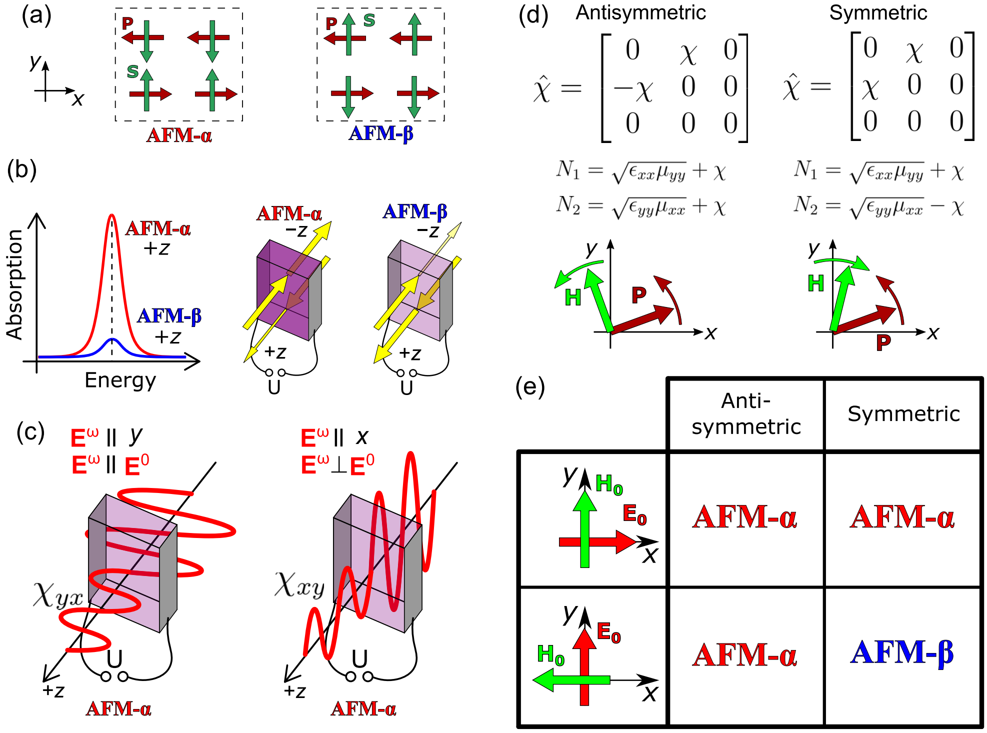
(a)
y
x
P
S
AFM-α
P
S
AFM-β
(b)
Absorption
Energy
AFM-α
+z
AFM-β
+z
AFM-α
−z
+z
U
AFM-β
−z
+z
U
(c)
$E^\omega \parallel y$
$E^\omega \parallel E^0$
χ_{yx}
U
+z
AFM-α
$E^\omega \parallel x$
$E^\omega \perp E^0$
χ_{xy}
U
+z
AFM-α
(d)
Antisymmetric
Symmetric
$\hat{\chi} = \begin{bmatrix} 0 & \chi & 0 \\ -\chi & 0 & 0 \\ 0 & 0 & 0 \end{bmatrix}$
$\hat{\chi} = \begin{bmatrix} 0 & \chi & 0 \\ \chi & 0 & 0 \\ 0 & 0 & 0 \end{bmatrix}$
$N_1 = \sqrt{\epsilon_{xx}\mu_{yy}} + \chi$
$N_2 = \sqrt{\epsilon_{yy}\mu_{xx}} + \chi$
$N_1 = \sqrt{\epsilon_{xx}\mu_{yy}} + \chi$
$N_2 = \sqrt{\epsilon_{yy}\mu_{xx}} - \chi$
y
H
P
x
y
H
P
x
(e)
Anti-symmetric
Symmetric
y
H_0
E_0
x
AFM-α
AFM-α
y
E_0
H_0
x
AFM-α
AFM-β

FIG. 1. (a) The two AFM domains of LiCoPO$_4$; AFM-α and AFM-β are characterized by ME coupling of opposite signs. (b) The dynamical magnetoelectric (ME) effect produces an absorption difference between light beams with the same polarizations propagating along the same directions ($+z$ or $-z$) in the two AFM domains. (c) Polarization of the probing light $\mathbf{E}^\omega$ can be selected either parallel or perpendicular to the poling electric field $\mathbf{E}^0$. Thus, in the dynamic ME measurement both elements of the ME susceptibility, χ_{xy} and χ_{yx}, can be simultaneously measured. (d) Electric polarizations and indices of refractions [Eqs. (1) and (2)] resulting from symmetric or antisymmetric ME susceptibility tensors ($\mathbf{P} = \hat{\chi}\mathbf{H}$) rotate against or together with the magnetic field, respectively. (e) For both the symmetric and antisymmetric forms of $\hat{\chi}$, the poling field combination ($+E_x^0$, $+H_y^0$) selects the AFM-α domain. However, for the 90° rotated poling fields, poling with ($+E_y^0$, $-H_x^0$) selects domain AFM-α or AFM-β in the case of antisymmetric and symmetric $\hat{\chi}$, respectively. This is because, with the former and latter forms of $\hat{\chi}$, the material couples to $E_x^0 H_y^0 \mp E_y^0 H_x^0$, respectively.

through the ordering temperature, which is often referred to as ME poling, while E^0 and H^0 are referred to as poling fields.

In general, the ME susceptibility tensor is the sum of a traceless symmetric part ($\hat{\chi}^{\mathrm{T}} = \hat{\chi}$, quadrupolar part), an antisymmetric part ($\hat{\chi}^{\mathrm{T}} = -\hat{\chi}$, toroidal part), and diagonal (axionlike) elements [2]. In order to visualize using a simple example how the magnetic-field-induced polarization varies with the orientation of the field, depending on the actual form of the ME tensor, we consider a system where the ME tensor has only two nonzero components, χ_{xy} and χ_{yx}. Correspondingly, the symmetric and antisymmetric parts of the ME tensor are given by $(\chi_{xy} + \chi_{yx})/2$ and $(\chi_{xy} - \chi_{yx})/2$, respectively. The symmetric and antisymmetric ME susceptibilities, often associated with quadrupolar and toroidal spin orders, respectively, behave differently upon the rotation of external fields in the xy plane, as shown in Fig. 1(d). If the magnetic-field-induced P is described by an antisymmetric ME susceptibility, it rotates in the same sense as H does, while it rotates in the opposite sense when generated by the symmetric, traceless ME susceptibility. Correspondingly, if the ME susceptibility tensor is fully antisymmetric, the selected domain depends only on the cross product of the poling E^0 and H^0 fields [see Fig. 1(e)]. Thus, poling with orthogonal E^0 and H^0 fields of certain orientation selects the *same* ME domain as poling with E^0 and H^0 fields mutually rotated by 90° in the xy plane. On the contrary, if the ME susceptibility tensor is symmetric and traceless, as shown in Fig. 1(d), the mutual rotation of E^0 and H^0 poling fields by 90° yields the selection of the *other* ME domain.

Static ME (P-H) measurements alone can usually provide limited information about the form of the ME susceptibility tensor. Since the same electric contacts are used to apply the E^0 poling field as well as to detect the magnetic-field-induced P, not all elements of the ME tensor can be measured in a single experimental configuration. More specifically, in a different experimental configuration where the E^0 poling field is perpendicular to the magnetic-field-induced P, it is difficult to perform a reliable measurement. In contrast, if the ME effect is detected optically via the ODA, the polarization of the probing light beam $\mathbf{E}^\omega$ can be chosen independently of the poling field direction, either $\mathbf{E}^\omega \parallel \mathbf{E}^0$ or $\mathbf{E}^\omega \perp \mathbf{E}^0$, as illustrated in Fig. 1(c). Thus, both off-diagonal elements, χ_{xy} and χ_{yx}, can be measured optically for a given ME domain selected by the poling.

III. STATIC ME EFFECT OF LiCoPO$_4$

The paramagnetic phase of LiCoPO$_4$ is described by a centrosymmetric and orthorhombic space group (*Pnma*); that is, this material does not have any spontaneous electric polarization. The site symmetry of the magnetic Co^{2+} ions allows local electric dipoles in the xz plane, which are arranged in a staggered configuration on the four Co sites in the unit cell of this structure [13]. At $T_{\mathrm{N}} = 21.3$ K a four-sublattice Néel-type AFM order emerges with $S = 3/2$ spins mainly coaligned along the y axis [22,23]. The two possible AFM domain states, α and β, which are also the two ME domains with opposite signs of $\hat{\chi}$, are illustrated in Fig. 1(a). In this compound, the Néel-type AFM order simultaneously breaks the inversion and the time-reversal symmetries, which allows finite χ_{xy} and χ_{yx} components of the ME tensor [4,24–26]. Although a small uniform canting of the spins may further reduce the magnetic symmetry and generate finite χ_{xz} and χ_{zx}, these weak secondary effects can be neglected in the present study [3,27]. Previously, the magnetically ordered state was identified as the first example of a ferrotoroidal order [3]; however, the form of the ME tensor, i.e., the relative sign of χ_{xy} and χ_{yx}, has remained an open question due to the experimental limitations discussed above [27].

We studied single-crystal LiCoPO$_4$ samples that were grown using the optical floating-zone method, similar to the procedure described in Ref. [28]. The ingots were aligned using a back-reflection Laue camera and cut into thin slabs with dimensions of $1 \times 5 \times 5\,\mathrm{mm}^3$. Static magnetization measurements up to $H = 140$ kOe were done using a physical property measurement system (PPMS, Quantum Design) equipped with a vibrating-sample magnetometer option. The magnetic-field-induced polarization measurements were carried out in a PPMS using an electrometer (6517A, Keithley) in the charge Q measurement mode.

Following the application of orthogonal poling fields ($\mathbf{E}^0 \parallel y$, $\mathbf{H}^0 \parallel x$) and ($\mathbf{E}^0 \parallel x$, $\mathbf{H}^0 \parallel y$), we measured the ME susceptibility as shown in Figs. 2(c) and 2(d), respectively. The experimental configurations are illustrated in Figs. 2(a) and 2(b), respectively. In both orientations, the measurement was carried out in all four different poling configurations, namely, with selectively reversed signs of the E^0 and H^0 fields. In the ordered phase $\mathbf{E}^0$ was switched off, and the displacement-current measurements were done in sweeping H field between ±1 kOe five times. The magnitudes of the measured ME susceptibilities at $T = 2$ K are $|\chi_{xy}|/c = 15$ ps/m and $|\chi_{yx}|/c = 32$ ps/m and agree well with those previously reported in the literature [4]. Poling E^0 and H^0 fields of the same sign select one ME domain, while poling fields of opposite signs select the other ME domain [13]. However, due to the experimental limitations inherent in the static ME experiments as described above, only the absolute value of one of the two finite off-diagonal components of $\hat{\chi}$ can be measured for a given orientation of the poling fields. In contrast, if the ME effect is investigated optically, one can determine both χ_{xy} and χ_{yx} for each poled state, as will be discussed in detail in the following. This requires only the rotation of the light polarization by 90° in the plane of the poling fields.

IV. OPTICAL DETERMINATION OF THE ME SUSCEPTIBILITY TENSOR

Spin excitations with ME character, the ME resonances [8,29], can be simultaneously excited by the electric ($\mathbf{E}^\omega$) and magnetic ($\mathbf{H}^\omega$) components of light and therefore can be exploited to probe the elements of the dynamic ME susceptibility tensor. Such spin resonances can show a strong absorption difference for the respective ME domains due to the opposite signs of the ME susceptibility in the two domains, α and β. When light propagates in such a material, the oscillating magnetizations in both the α and β domains fluctuate in phase with $\mathbf{H}^\omega$, while the corresponding magnetically induced polarizations in the two domains oscillate in antiphase with respect to each other. As a result, the index of refraction for light propagation along the $+z$ axis of the crystal is different for the two domains [30,31]:

$$N_1^{\alpha/\beta}(\omega) = \sqrt{\epsilon_{xx}(\omega)\mu_{yy}(\omega)} + \chi_{xy}^{\alpha/\beta}(\omega) \tag{1}$$

for $\mathbf{E}^\omega \parallel x$, $\mathbf{H}^\omega \parallel y$, and

$$N_2^{\alpha/\beta}(\omega) = \sqrt{\epsilon_{yy}(\omega)\mu_{xx}(\omega)} - \chi_{yx}^{\alpha/\beta}(\omega) \tag{2}$$

for $\mathbf{E}^\omega \parallel y$, $\mathbf{H}^\omega \parallel x$, where $\epsilon_{\nu\nu}$ and $\mu_{\nu\nu}$ ($\nu = x, y$) are elements of the dielectric permittivity and magnetic permeability tensors, respectively. The light absorption is different for the two ME (AFM) domains as the ME susceptibility has opposite signs for them, $\hat{\chi}^\alpha = -\hat{\chi}^\beta$. We note that the reversal of the light propagation direction from $+z$ to $-z$ is equivalent to the exchange of the ME domains [Fig. 1(a)]; thus, the ODA also has opposite signs for the two ME domains. The sign difference between Eqs. (1) and (2) is related to the rotation of the light polarization. From Eqs. (1) and (2), it follows that in materials with an antisymmetric ME effect ($\chi_{xy} = -\chi_{yx}$) the differences in the refractive indices of the two AFM domains, $\Delta N_1 = (N_1^\alpha - N_1^\beta)/2$ and $\Delta N_2 = (N_2^\alpha - N_2^\beta)/2$, are the same for the two orthogonal light polarizations, $\Delta N_1 = \Delta N_2 = \chi_{xy}$. On the other hand, for systems with symmetric ME susceptibility tensor ($\chi_{xy} = \chi_{yx}$), the differences in the refractive indices of the two domains changes sign upon the rotation of light polarization by 90°, i.e., $\Delta N_1 = -\Delta N_2 = \chi_{xy}$. We note here that such changes in the ODA have to be probed on a single excitation, as the sign of the optical ME susceptibility is specific to the different excited states.

V. MAGNONS, ELECTROMAGNONS, AND ME RESONANCES IN LiCoPO$_4$

Optical absorption spectra of LiCoPO$_4$ were measured at the National Institute of Chemical Physics and Biophysics, Tallinn, using a Martin-Puplett interferometer combined with a superconducting magnet, applying magnetic fields up to $H = 170$ kOe. The relative absorption spectra recorded at $T = 5$ K, using linearly polarized light with $\mathbf{E}^\omega \parallel y$ and x, are shown in Figs. 2(e) and 2(f) and 2(g) and 2(h), respectively. The sample was cooled to a ME single-domain state in $E^0 = 1$ kV/cm and $H^0 = 1$ kOe poling fields, respectively, applied

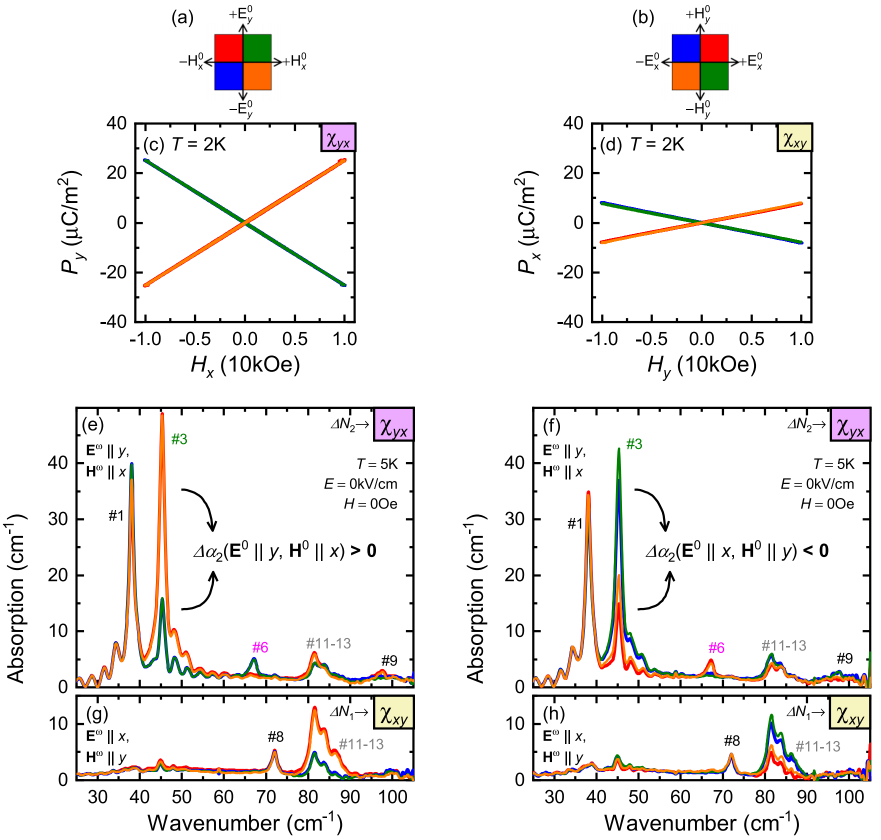

FIG. 2. Remanent static and dynamic ME effects in LiCoPO$_4$. (a) and (b) Experimental configuration of the $\mathbf{E}^0$ and $\mathbf{H}^0$ poling fields. The color code of (b) corresponds to the simultaneous 90° rotation of the fields of (a) [24]. (c) and (d) Poling field dependence of the *P*-*H* curves at $T = 5$ K for (c) $\mathbf{E}^0 \parallel y$ and $\mathbf{H}^0 \parallel x$ and (d) $\mathbf{E}^0 \parallel x$ and $\mathbf{H}^0 \parallel y$ poling field configurations. The color codes of (c) and (d) are shown in (a) and (b), respectively. The slopes of the *P*-*H* curves correspond to χ_{yx} and χ_{xy} in (c) and (d), respectively. The sign of the ME effect depends on the relative signs of the poling fields; note the complete overlap of the red and orange as well as the blue and green curves. (e)–(h) Optical absorption spectra measured at $T = 5$ K (e) and (g) with poling configurations indicated in (a) and (f) and (h) with poling configurations shown in (b). Spectra in (e) and (f) were measured using linearly polarized light with E^{ω}_y, H^{ω}_x, while those in (g,h) were measured with E^{ω}_x, H^{ω}_y. The spectra of the dynamic ME coefficients can be calculated as the absorption difference of the different domains, according to Eqs. (1) and (2). The $\Delta\alpha_2$ ODAs in (e) and (f) as well as in (g) and (h) change sign for the rotation of the poling E^0 and H^0 poling fields, according to Eqs. (3) and (4), respectively.

along the y and x axes. The low-temperature absorption measurements were carried out after switching off the poling fields. The relative absorption spectra were obtained by subtracting a reference spectrum taken in the paramagnetic phase, at $T = 30$ K [24]. Thus, the low-temperature spectral features are related to excitations emerging in the magnetically ordered state: Two strong (1 and 3) and several weaker (6, 8, 9, and 11–13) resonances appear in the AFM phase.

The poling-field-dependent resonances, 1, 3, 6, 9, and 11–13, are ME resonances since the ME response has opposite signs in the α and β domains. For the same signs of the poling fields, $(+E^0_y, +H^0_x)$ and $(-E^0_y, -H^0_x)$, modes 3, 9, and 11–13 have large absorptions, while for opposite signs of the poling fields, $(-E^0_y, +H^0_x)$ and $(+E^0_y, -H^0_x)$, the same modes show lower absorption. As the magnitude of the absorption difference for the ME domains is the highest for resonance 3, in the following we will focus on this mode. It appears when light polarization is $\mathbf{E}^{\omega} \parallel y$ and $\mathbf{H}^{\omega} \parallel x$; thus, according to Eq. (2), it probes $\chi_{yx}(\omega)$. For static poling fields $\mathbf{E}^0 \parallel y$ and $\mathbf{H}^0 \parallel x$ the difference of the absorption coefficients $\Delta\alpha = \frac{2\omega}{c}\mathrm{Im}(\Delta N)$ was found to be positive:

$$\Delta\alpha_2 = \left[\alpha_2\left(+E^0_y, -H^0_x\right) - \alpha_2\left(-E^0_y, -H^0_x\right)\right]/2 > 0, \quad (3)$$

which is clear from Fig. 2(e). On the other hand, for poling fields rotated by 90° to $\mathbf{E}^0 \parallel x$ and $\mathbf{H}^0 \parallel y$ the difference of the absorption coefficients changed sign:

$$\Delta\alpha_2 = \left[\alpha_2\left(+E^0_x, +H^0_y\right) - \alpha_2\left(-E^0_x, +H^0_y\right)\right]/2 < 0, \quad (4)$$

as seen in Fig. 2(f). From this we can conclude that if poling with $(+E^0_y, -H^0_x)$ and $(-E^0_y, -H^0_x)$ has selected domains α and β, respectively, then poling with $(+E^0_x, +H^0_y)$

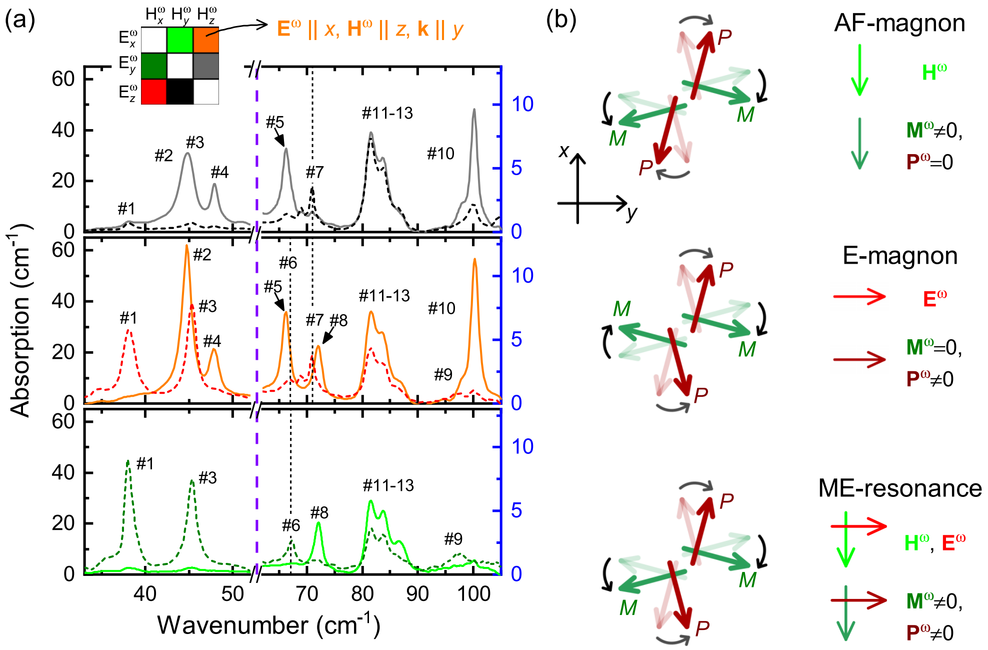

FIG. 3. (a) Optical absorption spectra, measured in six different configurations of $\mathbf{E}^\omega$ and $\mathbf{H}^\omega$ of the light at $T = 5$ K, revealing the selection rules of the magnetic excitations. The inset indicates the color code of the different light polarizations, along with an example where $\mathbf{E}^\omega \parallel x$, $\mathbf{H}^\omega \parallel z$, and $\mathbf{k} \parallel y$. Note the difference in the vertical scales corresponding to the spectral regions below and above the vertical dashed line. (b) Schematic illustration of an antiferromagnetic resonance (AF-magnon), an electromagnon (E-magnon), and a ME resonance. These modes are excited by only the magnetic component, by only the electric component, and simultaneously by both components of the electromagnetic radiation. For the sake of simplicity, we illustrate the excitations with one representative pair of spins M of the magnetic unit cell along with the respective local polarization P. The dynamic nature of the excitations is captured by curved arrows, which represent in-phase or antiphase oscillations of M and P. The net dynamic magnetization and polarization of the unit cell are labeled $\mathbf{M}^\omega$ and $\mathbf{P}^\omega$, respectively.

and $(-E_x^0, +H_y^0)$ must have selected domains β and α. It means that rotation of the poling fields by 90° results in the selection of the other ME domain, as illustrated in Fig. 1(e). As discussed in Sec. II and also visualized in Fig. 1(d), the selection of different ME domains by a 90° rotation of the poling fields implies that the symmetric traceless part of the ME tensor dominates over the antisymmetric one; hence, the symmetric product of the poling fields, $(E_x^0 H_y^0 + E_y^0 H_x^0)$, governs the poling and not their cross product. This also means that the magnetically induced polarization counterrotates with the magnetic field. Since neither component of the ME susceptibility changes sign below T_N [4], we concluded that the symmetric part dominates the low-temperature ME tensor. As a result, the magnitudes of the traceless symmetric

TABLE I. Summary of the magnetic excitations in terms of exciting fields, optical directional anisotropy (ODA), and classification of the resonances. This table is based on the zero-field measurements shown in Fig. 3.

Mode	Excitation	Remanent ODA	Class
1	$\mathbf{H}^\omega \parallel x$, $\mathbf{E}^\omega \parallel y$	+ODA (small)	ME resonance
2	$\mathbf{H}^\omega \parallel z$	no ODA	magnon
3	$\mathbf{H}^\omega \parallel x$, $\mathbf{E}^\omega \parallel y$	−ODA (large)	ME resonance
4	$\mathbf{H}^\omega \parallel z$	no ODA	magnon
5	$\mathbf{H}^\omega \parallel z$	no ODA	magnon
6	$\mathbf{H}^\omega \parallel x$	+ODA (100%)	ME resonance
7	$\mathbf{E}^\omega \parallel z$	no ODA	electromagnon
8	$\mathbf{E}^\omega \parallel x$	no ODA	electromagnon
9	$\mathbf{H}^\omega \parallel x$	−ODA (100%)	ME resonance
10	$\mathbf{H}^\omega \parallel z$	no ODA	magnon
11,12,13	present in each polarization	ODA	character cannot be determined

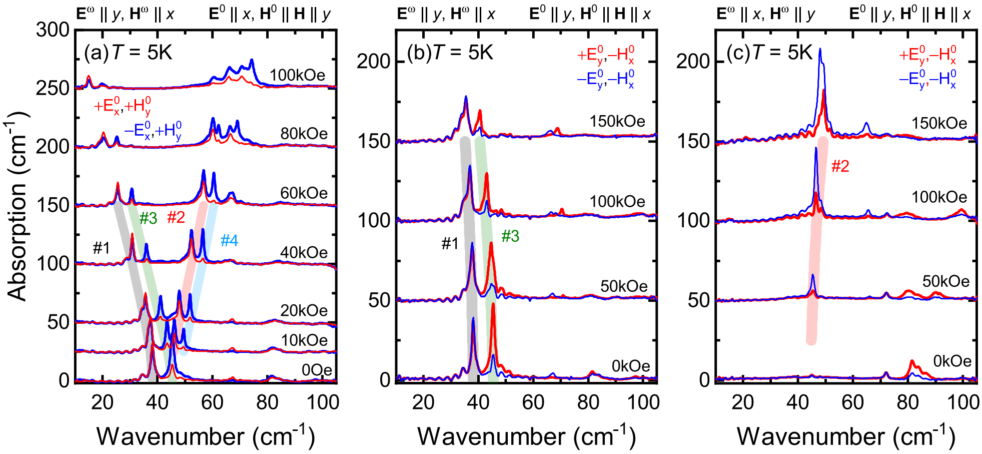

FIG. 4. Magnetic field dependence of the optical absorption spectra measured at $T = 5$ K for different combinations of the poling fields. The reference spectra, taken in the paramagnetic phase ($T = 30$ K), were subtracted from the spectra measured at $T = 5$ K. The poling fields were applied in the (a) ($\mathbf{E}^0 \parallel x$, $\mathbf{H}^0 \parallel y$) and (b) and (c) ($\mathbf{E}^0 \parallel y$, $\mathbf{H}^0 \parallel x$) configurations; the static magnetic field applied after poling was $\mathbf{H} \parallel \mathbf{H}^0$. The $\mathbf{E}^\omega$ polarization of the electromagnetic radiation was set along the (a) and (b) y and (c) x axes. For the purpose of clarity, each spectrum is shifted in proportion to the applied field by (a) 25 cm^{-1}/10 kOe and (b) and (c) 10 cm^{-1}/10 kOe.

and antisymmetric components of the static ME susceptibility are estimated to be $\chi^{\text{symm}}/c = 23.5$ ps/m and $\chi^{\text{antisymm}}/c = 8.5$ ps/m, respectively, based on the static measurements. The symmetric part is about 2.8 times larger than the antisymmetric one.

The selection rules were further studied by recoding the absorption spectra with light polarized along all the principal axes. The results of this systematic study are summarized in Fig. 3(a) and in Table I. In total, 13 resonances are observed, one more than expected from the multiboson spin-wave theory of a four-sublattice AFM with $S = 3/2$ spins [13]. Since the structural symmetry is preserved, no new phonon modes are expected in the magnetically ordered phase; thus, the origin of the extra mode is unclear. Figure 3(b) schematically illustrates the character of the different excitations. In the case of the usual zone-center magnon modes of antiferromagnets, there is a finite $\mathbf{H}^\omega$-induced magnetization in each unit cell, as the different magnetic sublattices oscillate in phase. There may be a dynamic electric polarization associated with the presence of individual spins, but these local polarizations oscillate out of phase and average to zero over the unit cell. Thus, these modes couple to only uniform $\mathbf{H}^\omega$ and not $\mathbf{E}^\omega$. In contrast for an electromagnon (E-magnon), responding only to $\mathbf{E}^\omega$, there is a finite electric polarization of the unit cell induced by the spin dynamics, but the dynamic magnetization is canceled due to the out-of-phase oscillation of the different sublattices. In the case of ME resonances, both the dynamic magnetization and polarization of the unit cell are finite; thus, these modes can be excited by $\mathbf{H}^\omega$ as well as $\mathbf{E}^\omega$. Modes 2 and 4 are usual magnon modes which are excited only by the oscillating magnetic field of light [13]. Modes 1, 3, 6, and 9 are ME resonances, as they exhibit ODA and are excited by both the H_x^ω and E_y^ω components of light. Mode 8 is an E-magnon, as it is excited only by E_x^ω. Modes 11–13 do not show simple selection rules but appear simultaneously for any polarization of the light, and they exhibit ODA for H_y^ω; thus, they are ME resonances. In summary, four magnon modes are excited by H_z^ω (2, 4, 5, and 10), four ME resonances are excited by H_x^ω as well as E_y^ω (1, 3, 6, and 9), and two E-magnons are excited by E_z^ω and E_x^ω (7 and 8, respectively).

VI. FIELD DEPENDENCE OF THE SPIN-WAVE EXCITATIONS

The characters and the frequencies of the spin-wave excitations together with their dynamic ME effect are further investigated using the magnetic-field-dependent absorption measurements shown in Fig. 4. The magnetic field dependence of the absorption spectra, measured at $T = 5$ K, is presented in Figs. 4(a) and 4(b) for $\mathbf{E}^\omega \parallel y$ and in Fig. 4(c) for $\mathbf{E}^\omega \parallel x$. The reference signal was again recorded in the paramagnetic phases at $T = 30$ K and subtracted from the $T = 5$ K spectra. The external magnetic field was applied in the same direction as the magnetic field used for poling, $H \parallel H^0$. Since the external magnetic field does not change the magnetic phase of the sample at low temperature [32], the domain state selected by the poling is preserved during the field-dependent measurements. The poling fields $E_x^0 = 1$ kV/cm and $H_y^0 = 100$ kOe are applied in Fig. 4(a). In this case, the two modes observed in zero field split into four distinct excitations. Modes 1 and 3 shift to lower energies in proportion to the magnetic field, while modes 2 and 4 shift to higher energies. In experiments corresponding to Figs. 4(b) and 4(c), poling fields of the same magnitude were applied in the perpendicular configuration, i.e., $\mathbf{E}^0 \parallel y$ and $\mathbf{H}^0 \parallel x$. In Fig. 4(b), only modes 1 and 3 are observed. With increasing magnetic field, they soften weakly and lose oscillator strength, while in Fig. 4(c) only mode 2 appears and slightly shifts to higher energies. In zero magnetic field, mode 2 is a usual magnon with no ODA; however, due to hybridization to

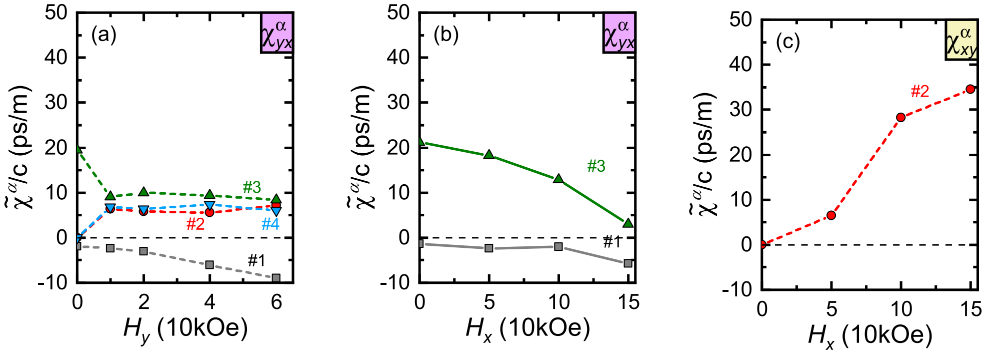

FIG. 5. Individual contributions of the different ME spin resonances to the static ME effect, calculated using the ME sum rule. (a) and (b) Field dependence of χ_{yx} for domain α, with $\mathbf{H} \parallel y$ and $\mathbf{H} \parallel x$, respectively. (c) Field dependence of χ_{xy} for domain α, with $\mathbf{H} \parallel x$. The color coding and the numbering of the curves correspond to the labeling of the modes in Fig. 4. For χ_{yx}^{α} and χ_{xy}^{α} the sum of the different contributions and their field and temperature dependences are shown in Fig. 6 in comparison with the data from the static measurements.

modes 1 and 3 it also shows considerable directional effect in finite magnetic fields.

According to the sum rule established in Ref. [21], excitations with ME character contribute to the static ME effect:

$$\chi_{ij}(0) = \frac{c}{2\pi} \int_0^{\infty} \frac{\Delta\alpha(\omega)}{\omega^2} d\omega, \tag{5}$$

where $\Delta\alpha(\omega)$ is the absorption difference caused by the ODA for light polarization $\mathbf{E}_i^{\omega}$ and $\mathbf{H}_j^{\omega}$. If the optical transitions are well separated in energy, it is possible to estimate the weight of each excitation to the static ME effect by limiting the integration around the excitation. We estimate the error of the individual contributions, originating from the weak overlap of neighboring modes, to be smaller than ±4 ps/m. The contributions of the respective resonances for domain α are denoted as $\tilde{\chi}^{\alpha}$.

The individual contributions of modes 1–4 to the static ME susceptibility estimated from the data presented in Fig. 4(a) for $\mathbf{H}^0 \parallel y$ are shown in Fig. 5(a). In this case the polarization of light $\mathbf{E}^{\omega}$ is perpendicular to the corresponding $\mathbf{E}^0$ poling field, and likewise, $\mathbf{H}^{\omega} \perp \mathbf{H}^0$, which corresponds to the transverse ME susceptibility in the static limit. The usual magnons, modes 2 and 4, which are forbidden in zero magnetic field for the polarization E_x^{ω} and H_y^{ω}, gain optical weight as well as a finite contribution to the χ_{yx}^{α} ME susceptibility in finite fields (for further details see Fig. S4 in the Supplemental Material). For fields larger than $H = 10$ kOe, modes 2, 3, and 4 have a roughly equal and field-independent contribution to the static ME effect. In contrast to the other excitations, mode 1 has a negative and increasing contribution in larger H field.

Figures 5(b) and 5(c) show the field dependence of the $\tilde{\chi}_{yx}^{\alpha}$ and $\tilde{\chi}_{xy}^{\alpha}$ ME susceptibilities for the $\mathbf{H} \parallel x$ field in the form of individual contributions from the different modes calculated using the ME sum rule on the data in Figs. 4(b) and 4(c), respectively. Modes 1 and 3 contribute only to χ_{yx}^{α}, while χ_{xy}^{α} is dominated by mode 2. Note that the contributions to χ_{yx}^{α}

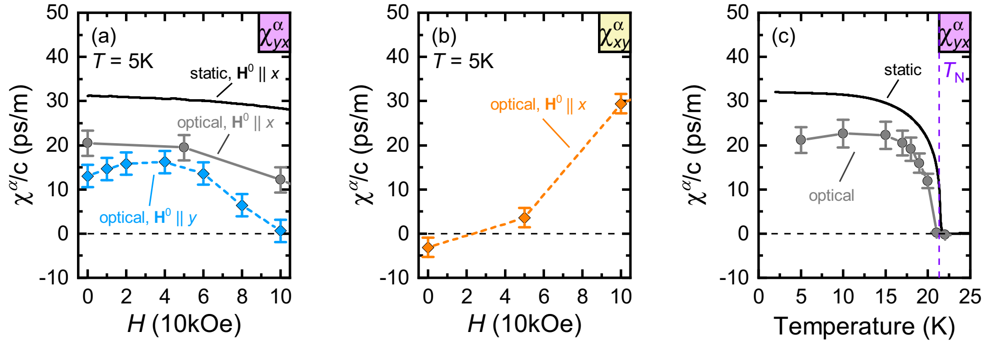

FIG. 6. (a) and (b) Magnetic field and (c) temperature dependences of the static and optical ME susceptibilities. The optical data were calculated using the ME sum rule over the complete spectral window. In (a), the gray and blue curves, corresponding to the field dependence of χ_{yx}^{α} for $\mathbf{H} \parallel x$ and $\mathbf{H} \parallel y$, respectively, should coincide at $H = 0$. Their slight deviation may come, e.g., from the imperfectness of the ME single-domain state in one of the measurements. (b) the magnetic field dependence of χ_{xy}^{α} in applied field $\mathbf{H} \parallel \mathbf{H}^0 \parallel x$. In (c), the optical spectroscopy measurements were carried out in the absence of H field, while static ME susceptibility was taken in warming runs with $H = 10$ kOe field. The corresponding, temperature-dependent optical absorption spectra can be found in Fig. S3 [24]. The error bars were estimated using the average of the ME susceptibilities between $\pm H$ fields.

from modes 1 and 3 have opposite signs for any direction of the magnetic field.

In Fig. 6 the zero-field static ME susceptibility obtained from magnetocurrent measurements and the sum of the contributions of the studied optical modes are compared. The value obtained via the ME spectroscopy, $\chi_{yx}/c = +20.5 \pm 2.9$ ps/m, is in rather good agreement with the static value $|\chi_{yx}|/c = 32$ ps/m. In this case the observed ME resonances explain well the bulk of the static ME response; that is, the polarization is mainly induced by the spin dynamics associated with the spin-wave modes observed in our experiment. On the other hand, $\chi_{xy}/c = -3.1 \pm 2.2$ ps/m, deduced from the optical experiments, is much smaller than the ME susceptibility $|\chi_{xy}|/c = 15$ ps/m measured in the static limit. The most likely explanation for this discrepancy is the presence of additional ME mode(s) or ME electronic excitations, lying out of the limited frequency range of our THz absorption measurement.

VII. CONCLUSIONS

The antiferromagnetic $LiCoPO_4$ has two possible antiferromagnetic domain states with opposite signs of the ME coupling, which can be selected by the simultaneous application of $\mathbf{E}^0$ and $\mathbf{H}^0$ poling fields orthogonal to each other. When selecting one of the domains by ME poling, the material shows optical directional anisotropy without any external fields, where the more transparent and absorbing directions are interchanged for the two domains. Using straightforward measurements of THz optical absorption after applying different ME poling configurations, we have found that the relative sign of the two allowed static ME susceptibility terms, χ_{yx} and χ_{xy}, is the same. According to our findings, the magnetic order promotes a cross coupling between electric and magnetic degrees of freedoms, which is described by a tensor with a symmetric (quadrupolar) component larger than the antisymmetric (torroidal) component. In summary, this optical method can be utilized to determine all off-diagonal elements of the ME susceptibility in a wide range of ME materials.

ACKNOWLEDGMENTS

The authors are grateful to J. Romhányi and K. Penc for discussions and for the technical assistance provided by A. Kikkawa and M. Kriener. V.K. was supported by RIKEN Incentive Research Project FY2016. This project was supported by institutional research funding IUT23-3 of the Estonian Ministry of Education and Research, by European Regional Development Fund Project No. TK134, by the bilateral program of the Estonian and Hungarian Academies of Sciences under Contract No. NKM-47/2018, by the BME-Nanonotechnology and Materials Science FIKP grant of EMMI (BME FIKP-NAT), by Hungarian NKFIH Grant No. ANN 122879, and by the Deutsche Forschungsgemeinschaft (DFG) via the Transregional Research Collaboration TRR-80: From Electronic Correlations to Functionality (Augsburg-Munich-Stuttgart).

---

[1] V. M. Dubovik and V. V. Tugushev, Phys. Rep. **187**, 145 (1990).
[2] N. A. Spaldin, M. Fiebig, and M. Mostovoy, J. Phys.: Condens. Matter **20**, 434203 (2008).
[3] B. B. van Aken, J.-P. Rivera, H. Schmid, and M. Fiebig, Nature (London) **449**, 702 (2007).
[4] J.-P. Rivera, Ferroelectrics **161**, 147 (1994).
[5] M. Baum, K. Schmalzl, P. Steffens, A. Hiess, L. P. Regnault, M. Meven, P. Becker, L. Bohatý, and M. Braden, Phys. Rev. B **88**, 024414 (2013).
[6] P. Tolédano, D. D. Khalyavin, and L. C. Chapon, Phys. Rev. B **84**, 094421 (2011).
[7] P. Tolédano, M. Ackermann, L. Bohatý, P. Becker, T. Lorenz, N. Leo, and M. Fiebig, Phys. Rev. B **92**, 094431 (2015).
[8] I. Kézsmárki, N. Kida, H. Murakawa, S. Bordács, Y. Onose, and Y. Tokura, Phys. Rev. Lett. **106**, 057403 (2011).
[9] Y. Kato, K. Kimura, A. Miyake, M. Tokunaga, A. Matsuo, K. Kindo, M. Akaki, M. Hagiwara, M. Sera, T. Kimura, and Y. Motome, Phys. Rev. Lett. **118**, 107601 (2017).
[10] S. Bordács, I. Kézsmárki, D. Szaller, L. Demkó, N. Kida, H. Murakawa, Y. Onose, R. Shimano, T. Rõõm, U. Nagel, S. Miyahara, N. Furukawa, and Y. Tokura, Nat. Phys. **8**, 734 (2012).
[11] P. Borisov, A. Hochstrat, X. Chen, W. Kleemann, and C. Binek, Phys. Rev. Lett. **94**, 117203 (2005).
[12] Y. Shiratsuchi, S. Watanabe, H. Yoshida, N. Kishida, R. Nakatani, Y. Kotani, K. Toyoki, and T. Nakamura, Appl. Phys. Lett. **113**, 242404 (2018).
[13] V. Kocsis, K. Penc, T. Rõõm, U. Nagel, J. Vít, J. Romhányi, Y. Tokunaga, Y. Taguchi, Y. Tokura, I. Kézsmárki, and S. Bordács, Phys. Rev. Lett. **121**, 057601 (2018).
[14] P. Babkevich, L. Testa, K. Kimura, T. Kimura, G. S. Tucker, B. Roessli, and H. M. Rønnow, Phys. Rev. B **96**, 214436 (2017).
[15] S. Di Matteo, Y. Joly, and C. R. Natoli, Phys. Rev. B **72**, 144406 (2005).
[16] C. Ederer, Eur. Phys. J. B **71**, 349 (2009).
[17] M. Fiebig, T. Lottermoser, D. Frohlich, A. V. Goltsev, and R. V. Pisarev, Nature (London) **419**, 818 (2002).
[18] A. S. Zimmermann, B. B. Van Aken, H. Schmid, J.-P. Rivera, J. Li, D. Vaknin, and M. Fiebig, Eur. Phys. J. B **71**, 355 (2009).
[19] T. Arima, J. Phys.: Condens. Matter **20**, 434211 (2008).
[20] M. Saito, K. Taniguchi, and T. Arima, J. Phys. Soc. Jpn. **77**, 013705 (2008).
[21] D. Szaller, S. Bordács, V. Kocsis, T. Rõõm, U. Nagel, and I. Kézsmárki, Phys. Rev. B **89**, 184419 (2014).
[22] R. Santoro, D. Segal, and R. Newnham, J. Phys. Chem. Solids **27**, 1192 (1966).
[23] D. Vaknin, J. L. Zarestky, L. L. Miller, J.-P. Rivera, and H. Schmid, Phys. Rev. B **65**, 224414 (2002).
[24] See Supplemental Material at http://link.aps.org/supplemental/10.1103/PhysRevB.100.155124 for further magnetization, polarization, and optical absorption measurements, as well as for the illustration of the experimental configurations.

[25] A. Szewczyk, M. U. Gutowska, J. Wieckowski, A. Wisniewski, R. Puzniak, R. Diduszko, Y. Kharchenko, M. F. Kharchenko, and H. Schmid, Phys. Rev. B **84**, 104419 (2011).

[26] V. M. Khrustalyov, V. M. Savytsky, and M. F. Kharchenko, Low Temp. Phys. **42**, 280 (2016).

[27] A. S. Zimmermann, D. Meier, and M. Fiebig, Nat. Commun. **5**, 4796 (2014).

[28] R. Saint-Martin and S. Franger, J. Cryst. Growth **310**, 861 (2008).

[29] Y. Takahashi, R. Shimano, Y. Kaneko, H. Murakawa, and Y. Tokura, Nat. Phys. **8**, 121 (2012).

[30] F. Wooten, *Optical Properties of Solids* (Academic, New York, 1972).

[31] V. Kocsis, Ph.D. thesis, Budapest University of Technology and Economics, 2016.

[32] N. F. Kharchenko, V. M. Khrustalev, and V. N. Savitskii, Low Temp. Phys. **36**, 558 (2010).

Curriculum Vitae

1. Personal data

Name	Johan Viirok
Date and place of birth	10 July 1989, Tallinn, Estonia
Nationality	Estonian

2. Contact information

Address	National Institute of Chemical Physics and Biophysics Akadeemia tee 23, 12618, Tallinn, Estonia
Phone	+372 5813 3968
E-mail	johanviirok@gmail.com

3. Education

2015–...	Tallinn University of Technology, School of Science, Engineering physics, PhD
2013–2015	Tallinn University of Technology, Faculty of Science, Engineering physics, MSc *cum laude*
2008–2013	Tallinn University of Technology, Faculty of Science, Engineering physics, BSc

4. Language competence

Estonian	native
English	fluent

5. Professional employment

2015– ...	National Institute of Chemical Physics and Biophysics, Junior Researcher
2012–2015	National Institute of Chemical Physics and Biophysics, Engineer

6. Voluntary work

2009–...	TTÜ Photoclub, Member of the Board, Chairman

7. Computer skills

- Operating systems: MacOS, Windows, Linux
- Document preparation: PowerPoint, Keynote, Beamer
- Programming languages: Python, Java, Javascript
- Scientific packages: matplotlib, NumPy, SciPy, Pandas, Origin

8. Honours and awards

- 2016, Johan Viirok, Talveakadeemia short articles contest 1st place

9. Defended theses

- 2015, Magnetic field induced directional dichroism of THz light in $Sr_2CoSi_2O_7$, MSc, supervisors PhD Toomas Rõõm and PhD Urmas Nagel, Tallinn University of Technology, Institute of Physics
- 2013, THz spectroscopy of Azurite at temperatures below 1 K, BSc, supervisors PhD Toomas Rõõm and PhD Urmas Nagel, Tallinn University of Technology, Institute of Physics

10. Field of research

- FIELD OF RESEARCH: 4. Natural Sciences and Engineering; 4.10. Physics and Technical Physics; CERCS SPECIALITY: P260 Condensed matter: electronic structure, electrical, magnetic and optical properties, supraconductors, magnetic resonance, relaxation, spectroscopy; SPECIALITY: (infrared and THz spectrometry of low dimensional and strongly correlated electron and spin systems, directional dichroism, high magnetic fields, low temperatures)

11. Scientific work

Papers

1. J. Viirok. Magnetväljaga tekitatud THz kiirguse suunadikroism multiferroidis $Sr_2CoSi_2O_7$. *Talveakadeemia*, 32-44, 2016.
2. R. S. Fishman, S. Bordács, V. Kocsis, I. Kézsmárki, J. Viirok, U. Nagel, T. Rõõm, A. Puri, U. Zeitler, Y. Tokunaga, Y. Taguchi, and Y. Tokura. Competing exchange interactions in multiferroic and ferrimagnetic $CaBaCo_4O_7$. *Phys. Rev. B*, 95:024423, Jan 2017.
3. J. Viirok, U. Nagel, T. Rõõm, D. G. Farkas, P. Balla, D. Szaller, V. Kocsis, Y. Tokunaga, Y. Taguchi, Y. Tokura, B. Bernáth, D. L. Kamenskyi, I. Kézsmárki, S. Bordács, and K. Penc. Directional dichroism in the paramagnetic state of multiferroics: A case study of infrared light absorption in $Sr_2CoSi_2O_7$ at high temperatures. *Phys. Rev. B*, 99:014410, Jan 2019.
4. L. Peedu, V. Kocsis, D. Szaller, J. Viirok, U. Nagel, T. Rõõm, D. G. Farkas, S. Bordács, D. L. Kamenskyi, U. Zeitler, Y. Tokunaga, Y. Taguchi, Y. Tokura, and I. Kézsmárki. Spin excitations of magnetoelectric $LiNiPO_4$ in multiple magnetic phases. *Phys. Rev. B*, 100:024406, Jul 2019.
5. V. Kocsis, S. Bordács, Y. Tokunaga, J. Viirok, L. Peedu, T. Rõõm, U. Nagel, Y. Taguchi, Y. Tokura, and I. Kézsmárki. Magnetoelectric spectroscopy of spin excitations in $LiCoPO_4$. *Phys. Rev. B*, 100:155124, Oct 2019.
6. K. Amelin, J. Engelmayerb, J. Viirok, U. Nagel, T. Rõõm, T. Lorenz, and Z. Wang, Experimental observation of high-energy E8 particles in the Ising chain ferromagnet $CoNb_2O_6$. *PNAS*, (SUBMITTED)

Conference presentations

1. J. Viirok. *Directional Dichroism of THz Radiation in Multiferroic* $Sr_2CoSi_2O_7$, IV international Symposium on Strong Nonlinear Vibronic and Electronic Interactions in Solids, 30 April – 03 May 2015, Tartu
2. J. Viirok. *Directional Dichroism of THz Radiation in Multiferroic* $Sr_2CoSi_2O_7$, 2nd Grandmaster PhD Workshop in Physics, 6–11 September 2015, Budapest, Hungary
3. J. Viirok. *THz spectroscopy of one-dimensional Ising chain compound* $CoNb_2O_6$ *near the quantum critical point*, American Physics Society March Meeting, 13–17 March 2017, New Orleans, USA
4. J. Viirok. *THz spectroscopy of one-dimensional Ising chain compound* $CoNb_2O_6$ *near the quantum critical point*, American Physics Society March Meeting, 5–9 March 2018, Los Angeles, USA
5. J. Viirok. *THz Spectroscopy of the Quantum Criticality in a Transverse Field Ising Chain Compound* $CoNb_2O_2$, EMFL Summer School: Science in High Magnetic Fields, 26–30 September 2018, Arles, France
6. J. Viirok. *THz Spectroscopy of the Quantum Criticality in a Transverse Field Ising Chain Compound* $CoNb_2O_2$, Graduate School of Functional Materials and Technologies Conference, 4–5 February 2019, Tartu
7. J. Viirok. *Non-Reciprocal Directional Dichroism of THz Radiation in Multiferroic* $Sr_2CoSi_2O_7$, American Physics Society March Meeting, 4–8 March 2019, Boston, USA
8. J. Viirok. *THz Spectroscopy of One-Dimensional Ising Chain Compound* $CoNb_2O_6$ *Near the Quantum Critical Point*, 4th Grandmaster Early-Career Workshop in Physics, 1–7 September 2019, Split, Croatia
9. J. Viirok. *THz spectroscopy of* $BiFeO_3$ *in the magnetic-field-induced canted AFM state*, American Physics Society March Meeting (CANCELLED), 2–6 March 2020, Denver, USA

Elulookirjeldus

1. Isikuandmed

Nimi	Johan Viirok
Sünniaeg ja -koht	10.07.1989, Tallinn, Eesti
Kodakondsus	Eesti

2. Kontaktandmed

Aadress	Keemilise ja Bioloogilise Füüsika Instituut, Akadeemia tee 23, 12618, Tallinn, Estonia
Telefon	+372 5813 3968
E-post	johanviirok@gmail.com

3. Haridus

2015–…	Tallinna Tehnikaülikool, Loodusteaduskond, Tehniline füüsika, doktoriõpe
2013–2015	Tallinna Tehnikaülikool, Matemaatika-loodusteaduskond, Tehniline füüsika, MSc *cum laude*
2008–2013	Tallinna Tehnikaülikool, Matemaatika-loodusteaduskond, Tehniline füüsika, BSc

4. Keelteoskus

eesti keel	emakeel
inglise keel	kõrgtase

5. Teenistuskäik

2015– …	Keemilise ja Bioloogilise Füüsika Instituut, nooremteadur
2012–2015	Keemilise ja Bioloogilise Füüsika Instituut, insener

6. Vabatahtlik töö

2009–…	TTÜ Fotoklubi MTÜ, juhatuse liige, esimees

7. Computer skills

- Operatsioonisüsteemid: MacOS, Windows, Linux
- Kontoritarkvara: PowerPoint, Keynote, Beamer
- Programmeerimiskeeled: Python, Java, Javascript
- Teadustarkvara paketid: matplotlib, NumPy, SciPy, Pandas, Origin

8. Autasud

- 2016, Johan Viirok, Talveakadeemia lühiartiklite konkursi II astme I koht

9. **Kaitstud lõputööd**

- 2015, Magnetväljaga tekitatud THz kiirguse suunadikroism multiferroidses $Sr_2CoSi_2O_7$-s, MSc, juhendajad PhD Toomas Rõõm ja PhD Urmas Nagel, Tallinna Tehnikaülikool, Füüsikainstituut

- 2013, Loodusliku asuriidi terahertsspektroskoopia temperatuuril alla 1 K, BSc, juhendajad PhD Toomas Rõõm ja PhD Urmas Nagel, Tallinna Tehnikaülikool, Füüsikainstituut

10. **Teadustöö põhisuunad**

- VALDKOND: 4. Loodusteadused ja tehnika; 4.10. Füüsika; CERCS ERIALA: P260 Tahke aine: elektrooniline struktuur, elektrilised, magneetilised ja optilised omadused, ülijuhtivus, magnetresonants, spektroskoopia; PÕHISUUND: (madalamõõduliste ja tugevalt korreleeritud elektron- ja spinnsüsteemide infrapuna ja THz-spektromeetria, suunadikroism, tugevad magnetväljad, madalad temperatuurid)

11. **Teadustegevus**
Teadusartiklite, konverentsiteeside ja konverentsiettekannete loetelu on toodud ingliskeelse elulookirjelduse juures.